CZECH TECHNICAL UNIVERSITY IN PRAGUE

FACULTY OF NUCLEAR SCIENCES AND PHYSICAL ENGINEERING

DEPARTMENT OF MATERIALS

DISSERTATION THESIS

Effect of Microstructure on Fatigue of Superelastic NiTi Wires

Prague 2021 Ondřej TYC

BIBLIOGRAPHIC ENTRY

Author	Ing. Ondřej Tyc Czech Technical University in Prague Faculty of Nuclear Sciences and Physical Engineering Department of Materials
Title of Dissertation	Effect of Microstructure on Fatigue of Superelastic NiTi Wires
Degree Programme	Application of Natural Sciences
Field of Study	Physical Engineering
Supervisor	Prof. Dr. RNDr. Miroslav Karlík Czech Technical University in Prague Faculty of Nuclear Sciences and Physical Engineering Department of Materials
Supervisor specialist	RNDr. Petr Šittner, CSc. Institute of Physics of the Czech Academy of Sciences Department of Functional Materials
Academic Year	2020/2021
Number of Pages	118
Keywords	Martensitic Transformation, NiTi, Heat Treatment, Superelasticity, Fatigue

B I B L I O G R A F I C K Ý Z Á Z N A M

Autor	Ing. Ondřej Tyc České vysoké učení technické v Praze Fakulta jaderná a fyzikálně inženýrská Katedra materiálů
Název práce	Vliv mikrostruktury na únavu superelastické slitiny NiTi
Studijní program	Aplikace přírodních věd
Studijní obor	Fyzikální inženýrství
Školitel	Prof. Dr. RNDr. Miroslav Karlík České vysoké učení technické v Praze Fakulta jaderná a fyzikálně inženýrská Katedra materiálů
Školitel specialista	RNDr. Petr Šittner, CSc. Fyzikální ústav AV ČR, v. v. i. Oddělení funkčních materiálů
Akademický rok	2020/2021
Počet stran	118
Klíčová slova	slitina NiTi, tepelné zpracování, martenzitická transformace, superelasticita, únava

ABSTRACT

NiTi wires having different nanocrystalline microstructures were subjected to thermomechanical tensile tests and fatigue tests in a wide temperature range. Accumulated unrecovered strains and microstructures evolving upon cycling were analyzed. Cyclic instability of stress-strain–temperature functional responses of NiTi is presumably due to the plastic deformation accompanying martensitic transformation proceeding under external stress. The unrecovered strains and density of lattice defects increased with increasing temperature and stress, at which the forward and/or reverse transformation proceeded. If the martensitic transformation proceeded at low stress (< 100 MPa), the cyclic responses of the wire were found to be stable (only marginal accumulated unrecovered strain and a few isolated dislocation loops and segments). If the forward and/or reverse martensitic transformation proceeded under large external stress (> 200 MPa), the responses of samples with 250 nm grain became unstable (large accumulated unrecovered strains and high density of dislocations and deformation bands). A scheme allowing for estimating the cyclic instability of functional behaviors of various NiTi wires in a wide range of thermomechanical loading tests was introduced. NiTi wires with the smallest grains (~ 20 nm) displayed a stable stress-strain response but the lowest fatigue life (N_f < 2500 cycles), while the wires with the largest grains (~ 250 nm) displayed an unstable response and highest fatigue life (N_f ~ 12000 cycles), though the N_f decreased rapidly with increasing test temperature. A suitable strategy to improve the fatigue performance of superelastic NiTi is to create microstructure that allows for some plastic deformation while suppressing the formation of deformation bands/twins leading to microstructure refinement. Among the tested microstructures, these requirements are best matched by the aged wire containing 75 nm grains and Ni_4Ti_3 nano-precipitates.

ACKNOWLEDGEMENT

I would like to first thank my supervisor specialist, Petr Šittner, and my supervisor, prof. Miroslav Karlík. Also, I would like to acknowledge Orsolya Molnárová, Jan Duchoň, Petr Svora, and Jaroslav Kupčík, for transmitting me their knowledge in the field of scanning and transmission electron microscopy. I am grateful to Miroslav Lamač and Luděk Heller, for the technical support and numerous consultations.

ABSTRAKT

NiTi dráty s odlišnými nanozrnnými mikrostrukturami byly podrobeny tahovým tepelně-mechanickým a únavovým testům v širokém rozmezí teplot. Při těchto testech byla analyzována akumulace nevratné deformace a vývoj mikrostruktury drátů. Cyklická nestabilita funkčního chování v prostoru napětí-teplota-deformace je pravděpodobně vyvolána lokalizovanou plastickou deformací doprovázející martenzitickou transformaci při cyklickém zatěžování pod vnějším napětím. Nevratná deformace a hustota mřížových poruch narůstá s rostoucí teplotou a napětím při nichž probíhá dopředná i zpětná transformace. Probíhá-li transformace při nízkých napětích (< 100 MPa), mechanické chování NiTi drátů je stabilní – vzniká pouze minoritní nevratná deformace a izolované množství dislokačních smyček. Pokud dopředná nebo zpětná transformace probíhá při vyšších napětích (> 200 MPa), mechanická odezva vzorků s velikostí zrn 250 nm se stává nestabilní – výrazně přibývá nevratná deformace, zvyšuje se hustota mřížových defektů a vznikají deformační pásy. Bylo sestaveno schéma umožňující odhad stability funkčního chování NiTi drátů v závislosti na tepelně-mechanickém zatěžování. Nejvyšší stabilitu superelastického chování vykazují dráty s nejmenší velikostí zrn (~ 20 nm), avšak životnost těchto vzorků je nejnižší (N_f < 2 500 cyklů). Naopak dráty s velikostí zrn okolo 250 nm vykazují nejvyšší životnost (N_f ~ 12 000 cyklů), ale jejich životnost výrazně klesá s rostoucí teplotou prostředí. Vhodnou strategií na zvýšení únavové životnosti NiTi slitiny je vytvoření mikrostruktury, která do určité míry umožňuje plastickou deformaci při superelastickém cyklování, avšak tvorba deformačních pásů a deformačních dvojčat je přitom potlačena. V rámci únavových testů tomuto požadavku nejlépe vyhovuje mikrostruktura s velikostí zrn 75 nm obsahující precipitáty fáze Ni_4Ti_3.

PODĚKOVÁNÍ

Rád bych poděkoval především konzultantovi RNDr. Petru Šittnerovi, CSc. a vedoucímu práce prof. Dr. RNDr. Miroslavu Karlíkovi. Také bych rád poděkoval za předání znalostí v oblasti SEM a TEM mikroskopie Orsolyi Molnárové, Janu Duchoňovi, Petru Svorovi a Jaroslavu Kupčíkovi. Dále bych rád poděkoval i Miroslavu Lamačovi a Luďku Hellerovi za technickou podporu a konzultace.

Contents

Abbreviations

ε_p^{up} – Upper plateau strain
ε_{tr} – Transformation strain
ε_{us} – Unrecovered strain
σ – stress
$\sigma^{F,R}$ – stress of a forward or reverse martensitic transformation
σ_p^{up} – Upper plateau stress of a superelastic cycle
σ_y – Yield stress
A – Ductility
A_f – Austenite finish temperature
A_s – Austenite start temperature
B2 – Cubic space group Pm-3m of austenite
B19’ – Monoclinic space group $P2_1/m$ of martensite
BF – Bright field
CW – Cold Work
DF – Dark field
DIC – Digital Image Correlation
DSC – Differential Scanning Calorimetry
FFS – Fatigue fracture surface
FTMT-EC – Final Thermomechanical Treatment by Electric Current
GB – Grain boundary
GI – Grain interior
M_f – Martensite finish temperature
M_d – Martensite desist temperature
M_s – Martensite start temperature
MITTER – Miniature testing rig
N_f – Number of fatigue cycles
R_m – Tensile strength
SAD – Selected area diffraction
SANS – Small-Angle Neutron Scattering
SMA – Shape Memory Alloys
SEM – Scanning electron microscopy
TEM – Transmission electron microscopy
TTT – Time Temperature Transformation
XRD – X-ray diffraction

1 State of the art

1.1 Introduction

Shape memory alloys (SMA) have already been used in a wide range of engineering applications in medicine, aerospace, robotics, and the automotive industry, owing to their unique superelastic and shape memory properties [1][2][3][4][5][6]. NiTi SMA alloys have the potential to be utilized in novel applications such as refrigeration/elastocaloric cooling or waste heat recycling [7][8]. However, some of these applications are severely limited by the fatigue life of NiTi. Superelastic and actuator fatigue of NiTi is hence currently being investigated from a wide variety of perspectives. The fatigue life of NiTi is limited to thousands of cycles in the superelastic regime in tension [9][10][11]. On the other hand, NiTi loaded in compression [12][13] or thermally cycled under constant load (actuation) [14][15][16] reaches a significantly longer fatigue life.

Superelastic properties can be modified by microstructure manipulation (cold working, annealing, and aging) [9][17][18][19][20]. Appropriate cold working/annealing can significantly improve functional degradation but not necessarily fatigue life. The aging treatment of Ni-rich NiTi seems to have a positive effect not only on functional fatigue but also on structural fatigue [9][21]. The aging of Ni-rich NiTi at temperatures around 400 °C for 0.5 - 2 h introduces 10 – 30 nm Ni_4Ti_3 precipitates into the material microstructure [21][22], as a result of which the microstructure is strengthened against plastic deformation and transformation temperatures increase.

Strain amplitude applied in a fatigue test affects fatigue performance, as in rotary-bending and torsional fatigue experiments [21][23][24] or even in tension [25], if transformation stress plateau is lost due to functional degradation. Contrarily, fatigue life is less sensitive to the strain amplitude within the plateau range in tensile tests [10] in which the superelastic deformation is localized [26]. Similar insensitivity to strain amplitude was observed even in rotary-bending tests in [9][27][28]. Besides the strain amplitude, the most important parameter of fatigue tests is the upper plateau stress [21][23][28][29] that can be adjusted by chemical composition, microstructure manipulation, and test temperature. Important factors are also surface finishing treatments [28][30] and TiC and Ti_2NiO_x inclusion content as fatigue cracks preferentially nucleate at the surface inclusions [31][32][33]. However, these factors are of less importance in this research as all samples were prepared from the same spool of 100 µm NiTi wire in a cold work state.

It is well known that the superelastic deformation of NiTi tends to be accompanied by plastic deformation giving rise to an accumulation of unrecovered strains upon cycling and the instability of cyclic stress-strain response (functional fatigue) [34][35][36]. However, it is much less understood how it affects structural fatigue (number of cycles until failure). Although higher functional degradation is commonly associated with inferior fatigue performance of NiTi at higher temperatures (stresses, strain amplitudes) [3][37], the coupling between microstructure changes and the functional and structural fatigue of superelastic NiTi still needs to be established.

In this research, superelastic NiTi wires were subjected to tensile fatigue tests with the aim to find out how functional and structural fatigue are affected by the virgin austenitic

microstructure (grain size, lattice defects, and Ni_4Ti_3 precipitates). The experimental approach to the characterization of functional and mechanical properties of NiTi wires in wide temperature and microstructure ranges introduced in [19] was adopted in the fatigue research presented here. The ultimate goal is to distinguish the effects of microstructure and temperature on the functional degradation and fatigue life in the superelastic regime.

Results of our earlier experiments on superelastic NiTi wires [34][38][39][40][41][42][43] suggest that the austenitic microstructure of NiTi may change significantly upon superelastic cycling due to plastic deformation accompanying the stress-induced martensitic transformation, particularly deformation twinning in oriented martensite. The deformation twinning in B19' martensite has been treated as a new deformation mechanism called kwinking by Seiner et al. [44] or earlier as a non-transformation pathway by Gao et al. [45][46] and proposed to be an origin of functional fatigue of NiTi. The same processes referred to as grain refinement in [47][48] have the potential to affect fatigue life. Whether these processes become activated or not during the superelastic cycling of nanocrystalline NiTi wires depends on the temperature and microstructure [19].

1.2 Superelasticity

Superelasticity is the stress-induced martensitic transformation. Fig. 1 shows a tensile superelastic cycle of a NiTi wire at various temperatures (above austenite finish temperature A_f). At first, the unloaded wire is in the B2 austenite (cubic). Then, the transformation from austenite to B19' martensite (monoclinic) is triggered upon reaching transformation stress (or transformation peak as shown in Fig. 1) and elastic loading is followed by exothermic transformation at almost constant stress. This part of the stress-strain curve is called transformation plateau and elongation of the wire is achieved by a change of the crystal structure. Then, reverse endothermic transformation (B19' $\rightarrow$ B2) takes place during unloading at a lower stress level than forward transformation, and the superelastic cycle is completed without permanent strain in the ideal case [49]. This is the simplest case of the superelastic cycle and some of the other phenomena accompanying superelastic cycling will be discussed later.

The position of transformation stresses is considerably influenced by ambient temperature since the higher the temperature is, the more stable austenite is. This relation is also expressed by the Clausius-Clapeyron relation

$$\frac{d\sigma}{dT} = \frac{-\Delta H}{T\varepsilon_{tr}}, \qquad (1)$$

where $d\sigma$ is the change of transformation stress, dT is the change of transformation temperature, ΔH is the enthalpy of transformation per unit volume, T is testing temperature, and ε_{tr} is transformation strain [50][51]. Only one martensite variant (ideally) is created in the superelastic cycle, unlike in the stress-free thermally-induced martensitic transformation. Transformation strain values depend on a loading axis orientation to the NiTi crystal lattice. Transformation strains for equiatomic single crystal NiTi are as follows: 10.7 % in [233] direction, 9.8 % in [111] direction, 8.4 % in [011] direction, and 2.7 % in [001] direction [49]. Commercially produced polycrystalline NiTi wires show transformation strain around 5-7 % [3][4][18].

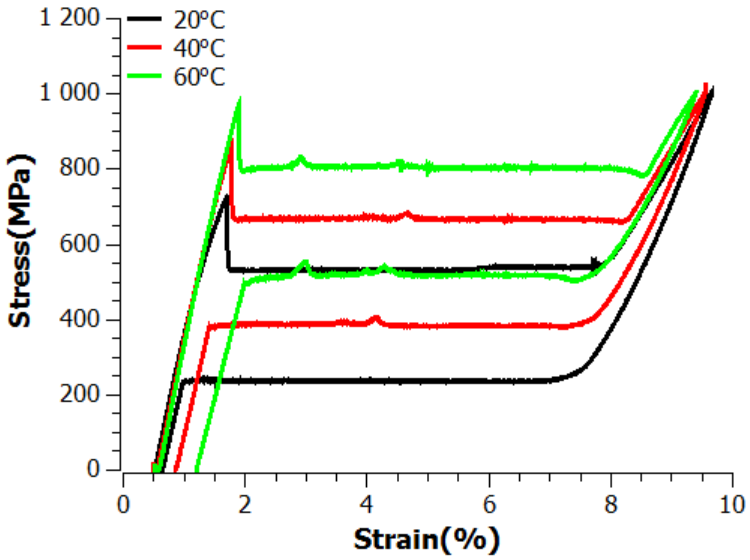

Fig. 1. Stress-strain curves of a superelastic NiTi wire at various temperatures.

The $\frac{d\sigma}{dT}$ ratio in equation (1) can be determined experimentally by superelastic loading at different temperatures, seen in Fig. 1. The slope of transformation stresses dependence on temperature, which is almost linear in a certain temperature range, expresses the $\frac{d\sigma}{dT}$ ratio (around 6 MPa/°C) [50]. However, plastic deformation (primarily <001> slip) and $\{114\}_{B2}$ compound austenite twinning of austenite is preferred above M_d (martensite desist) temperature and transformation does not occur [52]. On the other hand, when NiTi is cooled below temperature A_f, transformation is not fully reversible. In summary, reversible stress-induced transformation occurs in between the A_f and M_d temperature interval that is ~ 150°C wide (the so-called superelastic temperature window). Since superelastic behavior is accompanied by plastic strain at high temperatures (near to M_d), the temperature range for practical applications is even more limited [3], which will be later discussed in detail in section 1.5.

1.3 Heat treatment

Although cold-worked NiTi alloys exhibit high tensile strength (up to approx. 2 GPa), superelastic properties are suppressed by high dislocation density and even an amorphous phase is introduced by cold working [18][53]. A stress-strain curve of NiTi alloys under these conditions is similar to a conventional alloy. Furthermore, fracture toughness and ductility are significantly decreased, as will be discussed later [54]. Finally, conventional NiTi wires produced for superelastic applications contain over 50 at.% Ni. Excess Ni is dissolved in the NiTi matrix after a fabrication process of the wires and Ni-rich precipitates are not present in the NiTi matrix [18]. Thus, heat treatment is required to restore the microstructure with desired functional properties. Processes such as dislocation recovery, recrystallization, and precipitation are utilized to set transformation stresses and strain, stability of superelastic loop (accumulation of permanent strain), and tensile strength. The process of heat treatment and the final material properties depend on previous history (cold work, grain size, impurities, etc.) as well [18][55]. The effect of heat treatment on stress-strain response is illustrated in Fig. 2. Although the change of transformation stresses is inevitable during superelastic cycling, other parameters such as permanent strain or tensile strength can be modified by heat treatment.

Individual processes taking place in heat treatment and their influence on functional properties will be discussed in the following sections.

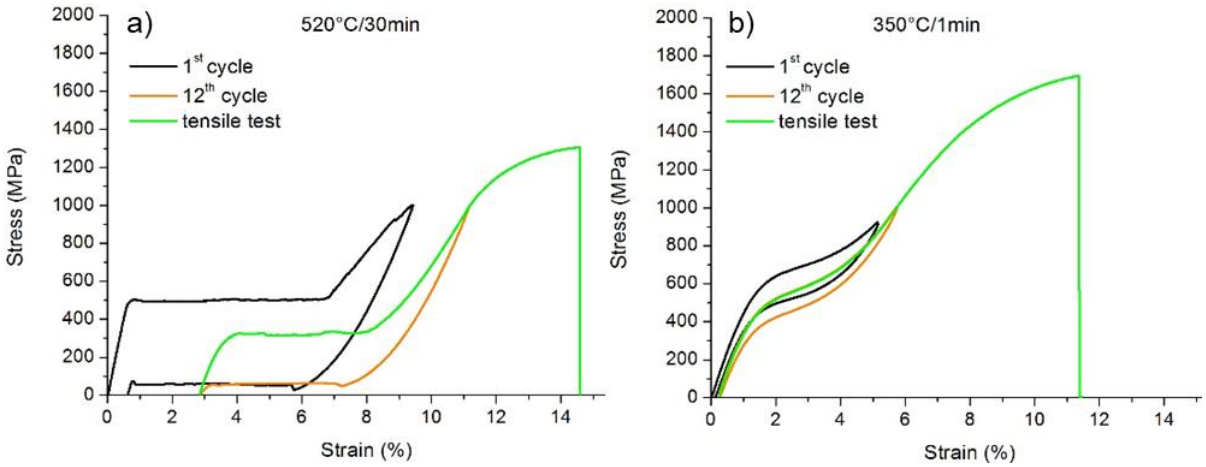

Fig. 2. Comparison of the 1st and 12th superelastic cycle followed by tensile test until rupture at 20 °C of the same type of NiTi wire subjected to different heat treatment a) 520°C/30min and b) 350°C/1min.

1.3.1 Precipitation

Precipitates are particles with a different crystal structure and composition than the matrix and are created by the decomposition of supersaturated solid solution (precipitation). Quenching below solvus temperature (creation of supersaturated solid solution) and precipitation at the appropriate temperature is commonly used to create fine precipitates suppressing dislocation movement and increasing tensile strength. Solvus temperature of the stable NiTi phase region is illustrated in Fig. 3 [49]. Types of precipitates and their influence on the superelastic response will be discussed in the following section.

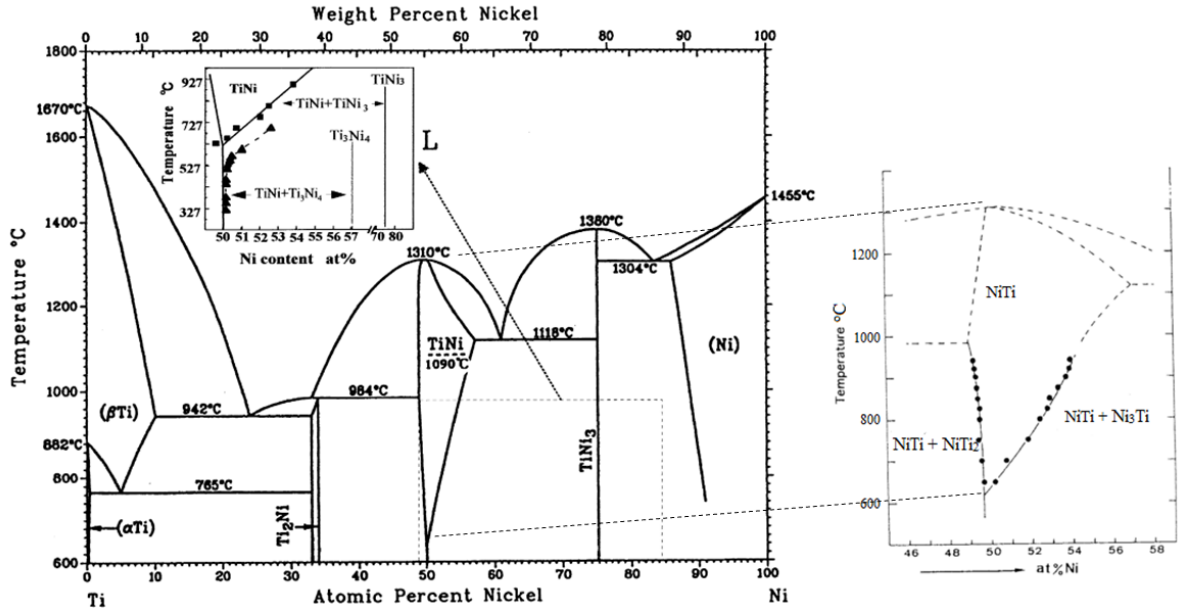

Fig. 3. Ni-Ti phase diagram and detail of the superelastic composition region. [49][51]

1.3.1.1 Ni-rich precipitates

Precipitation often takes place in several superelastic stages, in which metastable phases are created before reaching the final stable phase. Three types of Ni-rich precipitates (Ni_4Ti_3, Ni_3Ti_2, and Ni_3Ti) are known in NiTi alloy. Ni_4Ti_3 and Ni_3Ti_2 are metastable phases and Ni_3Ti is the final stable phase with the highest Ni concentration. Although the phase diagram in Fig. 3 shows that precipitation should proceed above 50 at.% Ni, supersaturation around 50.5 at.% Ni is needed to trigger precipitation processes in the NiTi matrix in a reasonable time period [51][57]. Maximal attainable supersaturation in the Ni-rich NiTi is around 57 at.% Ni. On the other hand, only about 51 at.% Ti supersaturation is attainable in the Ti-rich NiTi matrix. The alloy exhibits weak dependence of transformation temperatures on composition in this region and M_s (martensite start) temperature is around 60-70 °C. This differs from the Ni-rich region, where transformation temperatures and stresses are sensitive to composition (see Fig. 4). Therefore, precipitation decreasing Ni content in the matrix can be used to decrease transformation stresses in a superelastic loading or increase transformation temperatures of a thermal actuator.

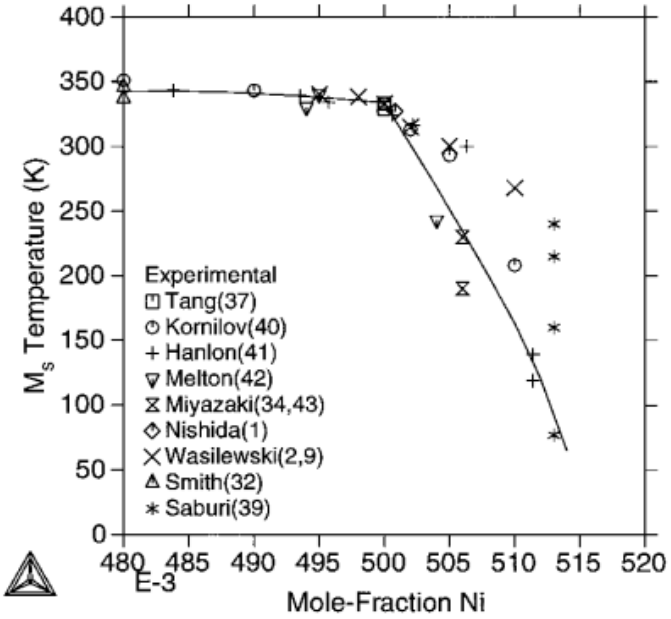

Fig. 4. a) Influence of Ni content on transformation temperature martensite start (M_s), the solid curve shows predicted values according to [50] (M_s = 60 °C at 50 at.% Ni and increase of 0.1 at.% results in about 16 K decrease in M_s temperature) in comparison with experimental data of various researchers.

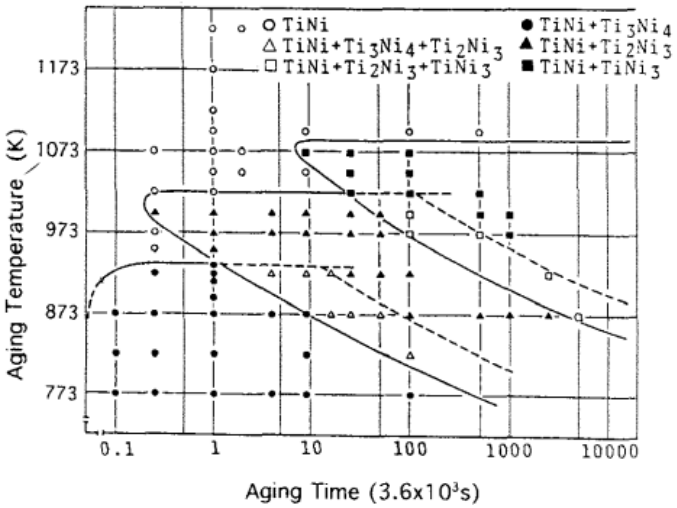

Fig. 5. TTT diagram of $Ni_{52}Ti_{48}$ alloy precipitation after homogenization at 1000 °C and quenching. [51]

The TTT (Time Temperature Transformation) diagram of $Ni_{52}Ti_{48}$ alloy is shown in Fig. 5. The aging of the Ni-rich alloy can be separated into 3 temperature ranges:

a) At first, Ni_4Ti_3 precipitates are created below 680 °C. Then, the Ni_3Ti_2 phase is created and the final product of annealing is the Ni_3Ti phase after an extremely long time (< 1000 h).

b) The Ni_4Ti_3 phase is not created at a temperature above 680 °C and Ni_3Ti_2 precipitates are created instead in the temperature range of 680 °C-750 °C followed by Ni_3Ti precipitates after a longer time of annealing.

c) The Ni_3Ti phase is created directly without metastable phases in the temperature range of 750 °C-800 °C. The NiTi matrix is stable above 800 °C at the given composition, and precipitation is not taking place or Ni-rich phases dissolve. [51]

Ni_4Ti_3 precipitates have a rhombohedral crystal structure (a = 0.6704 nm, α = 113.85°), lenticular shape (Fig. 6), and nucleate at relatively low temperatures [51][58][59]. Ni_4Ti_3 shrinks 2.3 % in the direction of the habit plane normal, and 0.5 % in the habit plane [49], which is given by the difference of lattice parameters and molar volume. Thus, strain fields are created around coherent precipitates. Small precipitates are coherent with a matrix up to approx. 150-300 nm [60][61] (or up to 500 nm according to [59]). These strain fields increase tensile strength [3] and promote R-phase transformation [49][57][62]. The higher size of precipitates leads to semi-coherent interface, and lattice strain is relaxed by dislocations [59]. However, the Ni_4Ti_3 phase does not exhibit martensitic transformation. Therefore, Ni_4Ti_3 does not contribute to superelastic behavior, and a shortening of transformation strain can be expected after aging [17]. Orientation relation between coherent Ni_4Ti_3 and B2 matrix is: $(001)_{Ni4Ti3}||(111)_{B2}$, $[010]_{Ni4Ti3}||[213]_{B2}$ and the habit plane $\{111\}_{B2}$ [51].

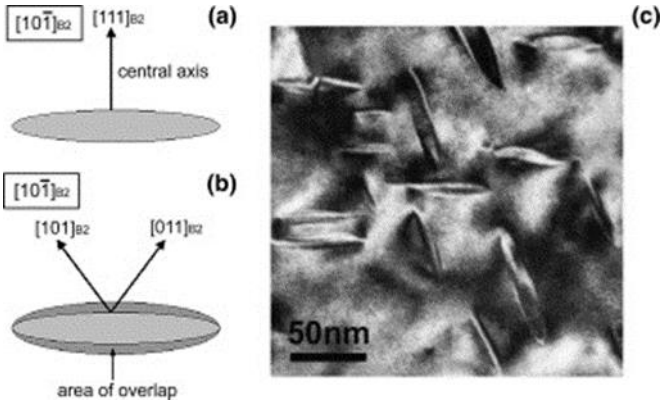

Fig. 6. Orientation in the NiTi matrix and TEM micrograph of Ni_4Ti_3 precipitates. [60]

The second type of precipitate is the Ni_3Ti_2 phase. These precipitates also exhibit phase transformation. Crystal structure is tetragonal (a = 0.3095 nm and c = 1.3585 nm) at around 100 °C and orthorhombic (a = 0.4398 nm, b = 0.4370 nm and c = 1.3544 nm) at room temperature [49]. No considerable strengthening effect has been reported yet. The last stable phase is Ni_3Ti with a hexagonal crystal structure (a = 0.510 nm and c = 0.831 nm) [63].

1.3.1.2 Factors affecting precipitation

Heterogeneities and defects in the crystal structure

Precipitation is diffusion-driven phase transformation. The creation of stable nuclei followed by growth is needed to create precipitates in general and a phase interface is established between precipitate and matrix, which is a barrier for further growth. The energy of the interface is proportional to a discrepancy of lattice parameters of matrix and precipitate. Thus, precipitation takes place through metastable stages (Ni_4Ti_3, Ni_3Ti_2) before stable precipitates (Ni_3Ti) are created. Nucleation of precipitates is also energetically favorable in areas of crystal defects, where deformation energy is released by the growth of precipitates. These areas are dislocation networks, grain boundaries, stacking faults, or inclusions such as carbides (Fig. 7) [49][64]. The effect of grain boundaries can be seen especially in large grains, where the grain interior is almost without precipitates unlike the grain exterior (Fig. 7c). Even Ni_4Ti_3 precipitates affect the nucleation of other precipitates in their surroundings by strain fields and lead to the arrangement captured in Fig. 7d [64]. The above-mentioned circumstances affect the driving force (ΔG) of the diffusional phase transformation, which can be expressed by individual components

$$\Delta G = \Delta G_V + \Delta G_S + \Delta G_E + \Delta G_D, \quad (2)$$

where $\Delta G_V < 0$ is transformation energy (proportional to the volume of precipitate), the sign of inequality shows higher stability of precipitate than supersaturated matrix at given conditions, $\Delta G_S > 0$ is the energy of phase interface between matrix and precipitate (proportional to the surface of precipitate), $\Delta G_E > 0$ is the change of strain energy in the crystal lattice and $\Delta G_D < 0$ is the energy of crystal defects. A level of supersaturation also affects the kinetic of precipitation processes, as will be discussed in the section 1.4 R-phase.

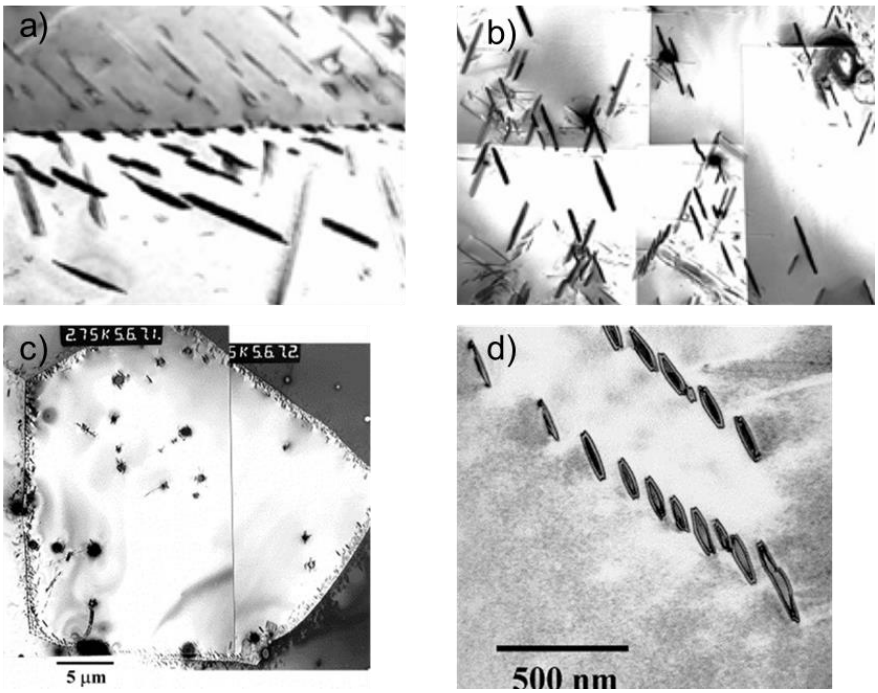

Fig. 7. The presence of Ni_4Ti_3 precipitates on a) grain boundaries and b) inclusions. c) Absence of precipitates in grain interior of large grains and d) chain of Ni_4Ti_3 precipitates - growth in the stress field of neighboring particles [64]

Temperature

As Ni-rich precipitates with higher Ni content require higher temperatures or longer aging time, the Ni_4Ti_3 phase is created at relatively low temperatures and aging may take only minutes. Commonly used NiTi wires manufactured for superelastic applications contain approx. 50.5-51 at. % Ni. Therefore, precipitation of Ni-rich phases is shifted to lower temperatures than in 52 at.% Ni alloy shown in the TTT-diagram (Fig. 5) and the creation of Ni_4Ti_3 has been reported even at a temperature around 250 °C in 50.8 at.% Ni alloy. However, growth is significantly hindered and the size of precipitates does not exceed 20 nm even after hundreds of hours [58]. Solvus temperature for Ni_4Ti_3 phase is around 500-550 °C for this composition [3], which is in the recrystallization temperature range as well [18]. The ideal reported temperature for the fast nucleation and growth of the Ni_4Ti_3 phase is around 425-450 °C [3][65]. Diffusional processes are faster at higher temperatures, but nucleation rate decreases, yielding a smaller number of large semi-coherent precipitates, and tensile strength decreases [3].

Stress-assisted aging

Eight crystallographic variants of Ni_4Ti_3 can are formed on {111}-planes [51]. As mentioned above, precipitates create strain fields. Therefore, external or internal stresses can favor or suppress the occurrence of certain Ni_4Ti_3 variants [66]. External stresses can remedy the heterogeneous distribution of precipitates in the large grains (see Fig.7c) and precipitation occurs also in the grain interior. Less than 10 MPa is needed to achieve this effect [67]. Habit planes of precipitates subjected to external tension during aging tend to be parallel to the direction of the applied stress. On the other hand, habit planes orient perpendicular to applied compression stress during aging [68][69]. For example, two variants of precipitates

perpendicular to each other can be formed in a bent wire during aging due to tension/compression stresses. Stress-assisted aging also affects the size of precipitates. Unlike stress-free aging, where the size of precipitates increases with increasing distance from the grain boundary, the size of precipitates is more homogeneous after stress-assisted aging [64].

1.3.2 Recovery and Recrystallization

Recovery processes also take place approximately within the temperature range of Ni_4Ti_3 phase precipitation. Dislocation density decreases in general, which consists of polygonization, annihilation, or gliding of dislocations, and internal stresses relax [55]. Recrystallization is referring to nucleation and growth of new grains with low defect density. Nucleation sites are preferentially regions with high stored deformation energy like nucleation sites for precipitation (grain and subgrain boundaries, inclusions, or shear bands). Primary recrystallization is finished when the former cold-worked microstructure is replaced by recrystallized grains. Then, further grain growth (secondary recrystallization) may follow. This phenomenon is undesired as grains above approx. 200 nm without precipitates are prone to dislocation activity in superelastic cycling leading to high permanent strain (instability of superelastic loop, see Fig. 8, 9) [18].

Recrystallization occurs in commercial NiTi wires at temperatures above 450 °C [70]. As recrystallization belongs to diffusional-driven processes, an increase in temperature is naturally accelerating grain growth. However, recrystallization temperature and kinetic of grain growth may significantly vary. On one hand, the presence of alloying elements, inclusions, or precipitates decreases recrystallization kinetic (Zener pinning). On the other hand, a higher degree of cold work (higher deformation energy) has the opposite effect. Higher cold work also increases nucleation rate (number of recrystallized grains) and yields microstructures with finer grains [55]. For example, 1 µm grains are present in superelastic wires before cold working in contrast to 20-50 nm grains after cold working followed by heat treatment [18]. If the heating rate and final temperature are high enough, recrystallization takes place at the expense of the other processes (recovery and precipitation) [55].

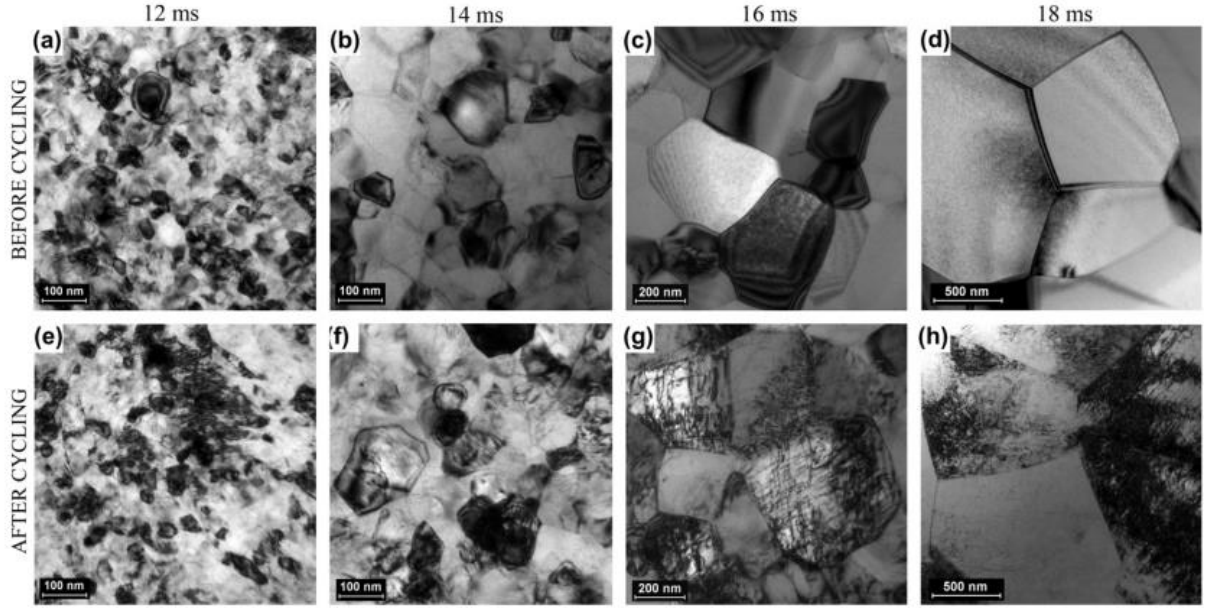

Fig. 8. TEM of NiTi wires with various grain sizes after pulse heat treatment. (a)-(d) micrographs show grain structure before superelastic cycling and (e)-(h) after superelastic cycling. [18]

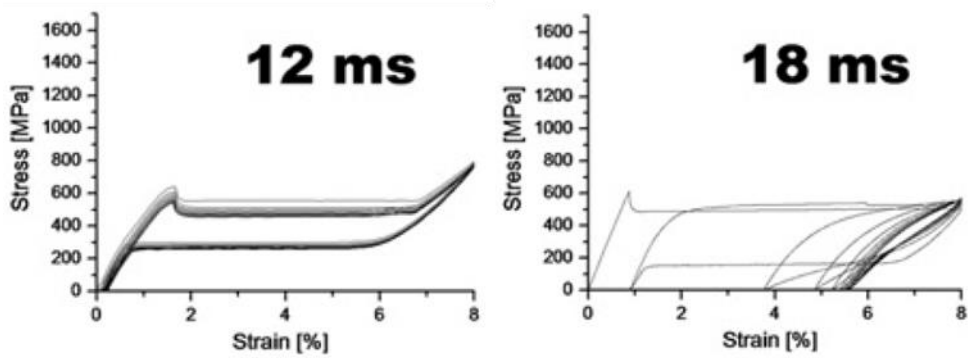

Fig. 9. Ten superelastic cycles of NiTi wire at room temperature after pulse heat treatment by 160W/mm^3 power density for 12 ms and 18 ms. [18]

These processes are necessary for the recovery of superelastic and shape memory properties of NiTi alloy after cold working since dislocation networks and grain boundaries of nanosize grains inhibit propagation of martensitic transformation, which increases transformation stress and decreases transformation strain [18][71]. It is necessary to realize that heat treatment triggers several processes in general and each of them affects the final microstructure and functional properties of NiTi alloy.

1.3.3 Pulse heat treatment by electric current

A unique method of pulse annealing by electric current (Final Thermomechanical Treatment by Electric Current (FTMT-EC)) was developed for fast annealing of thin NiTi wires intended for medical or textile applications [72][73][74]. Functional properties and final microstructure are set in milliseconds (see Figs. 8,9, and 11) by passing electric current and temperature is not constant in this type of annealing, unlike conventional annealing. Duration and power of the electric pulse can be precisely adjusted to set the desired superelastic response or track the evolution of the microstructure. Moreover, the activity of precipitation processes is suppressed in the short electric pulse [18][53]. Since precipitation is mostly accompanied by other diffusional processes (recovery and recrystallization) during conventional annealing, the FTMT-EC method can be used to some extent to separate the influence of recovery processes and precipitation on mechanical properties.

Properties of a NiTi wire can be monitored during the electric pulse annealing. An illustration of the annealing process is shown in Fig. 10, where a 50 mm wire with a 0.1 mm diameter and 45% initial cold work is prestressed to 400 MPa. The increase of stress at the beginning of the electric pulse (3W/1s) is attributed to the reverse transformation of residual martensite induced by severe plastic deformation during cold working. Then, thermal expansion and even plastic deformation prevail, and stress decreases at constant constrain. Finally, stress increases during the cooling of the wire, when the electric pulse is terminated. The decrease in resistivity is given by recovery processes. The total decrease is about 40 %. The end of a steep decrease in resistivity at 1.5 s indicates that the wire is already superelastic with plateau strain. Further annealing is increasing temperature in the wire, and grain size is increasing as well. Thus, tracking of resistivity during electric pulse provides worthwhile information.

The evolution of NiTi wire properties (grain size, transformation strain in the first superelastic cycle, and permanent strain after 10 cycles) are shown in Fig. 11 after electric pulse at constant power (160W/mm^3). Accelerated grain growth begins in the initial nanograin microstructure

after 12 ms and grain size increases up to approx. 1 μm at 18 ms. Increased permanent strain is attributed to grain growth and related decrease in yield stress. However, the longer the time of annealing, the higher the transformation strain. Therefore, compromise annealing parameters are needed to obtain balanced functional properties and the FTMT-EC method is suitable for this objective. As annealing temperature is not constant during the short electric pulse and increases with time, the effect of annealing time is more considerable than is usual in conventional heat treatment.

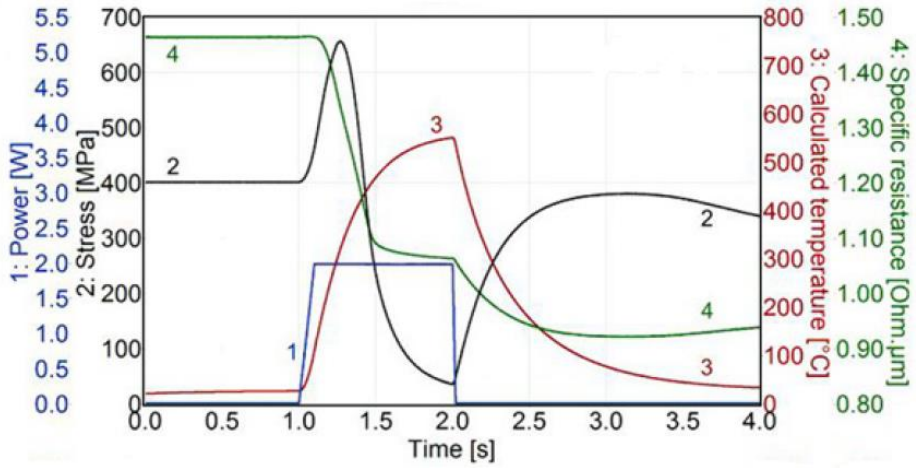

Fig. 10. Process of heat treatment by electric current as a function of time- 1) applied power, 2) evolution of stress, 3) calculated temperature profile, and 4) evolution of resistance. [53]

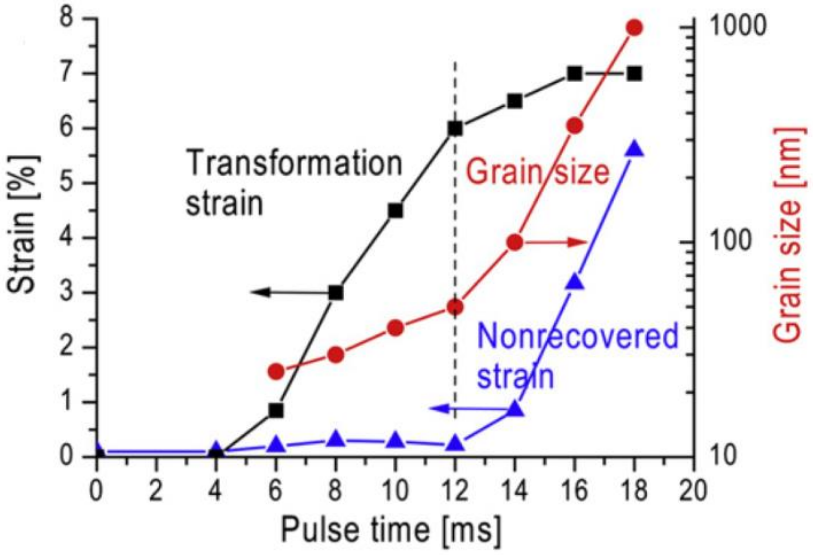

Fig. 11. Evolution of transformation strain (black), grain size (red), and permanent strain (blue) as a function of annealing time at power 160 W/mm^3. [18]

1.4 R-phase

The so-called R-phase can be formed in stress- or temperature-induced martensitic transformation under specific conditions. R-phase has a rhombohedral crystal structure: a = 0.301 nm and $\alpha < 90°$ decreases with decreasing temperature (α = 89.57° at 292 K and α = 89.32° at 272 K [75]). The formation of the R-phase can be described as the stretching of B2 austenite along [111] direction [49].

The three main reasons promoting the formation of the R-phase are 1) strain fields of precipitates, 2) dislocations, or 3) alloying elements [49]. Free energy of martensite is increased in each of the cases and R-phase transformation is more favorable to occur as the free energy of the R-phase is not affected so significantly by change of microstructure or chemical composition [62].

In superelastic loading, B2→R-phase→B19‘ two-step transformation sequence takes place (Fig. 12a). Either reverse transformation B19‘→R→B2 or only B19‘→B2 transformation proceeds in a NiTi alloy after a previous forward two-step transformation, depending on the microstructure of the alloy and the testing temperature [76]. The same sequence of transformations takes place during the cooling and heating thermal cycle (see Fig. 13a) [49][75][77].

As R-phase transformation occurs in strain fields of Ni_4Ti_3 precipitates, the R-phase can be utilized as an indicator of precipitation processes as shown in Fig. 12, where a) shows stress-strain and resistance-strain response of the NiTi wire annealed by a short pulse followed by 15 min aging and b) shows the response of the wire annealed by an electric pulse (without precipitates). [17][56]

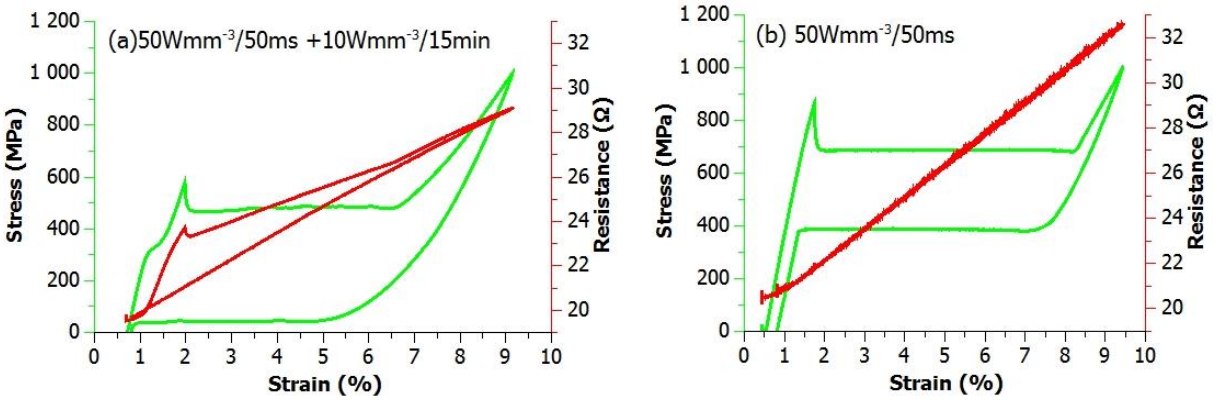

Fig. 12. Identification of R-phase transformation in stress-strain and resistance-strain curves of a NiTi wire (a) with R-phase transformation at approx. 350 MPa, (b) without R-phase transformation.[56]

The transformation strain of B2-R-phase transformation is around 0.5-1 % in a single crystal, which is ten times lower than B2-B19‘ transformation [51]. However, B2-R-phase transformation exhibits very low hysteresis both in temperature (1-2 °C) and stress (20-50 MPa) cycle in comparison with B2-B19‘ transformation [49]. Transformation stress of B2-R-phase transformation is more dependent on temperature ($d\sigma/dT$ ~17MPa/K [75]) than the B2-B19‘ one. Since the R-phase has the highest resistivity of NiTi phases, an increase of resistivity is another sign revealing R-phase transformation. Values of resistivity are 82 μΩ/cm for austenite, 65 μΩ/cm for martensite, and 98 μΩ/cm for R-phase according to [77]. However, resistivity may vary depending on a thermomechanical treatment or twinning of martensite (self-accommodation or preferential orientation under stress).

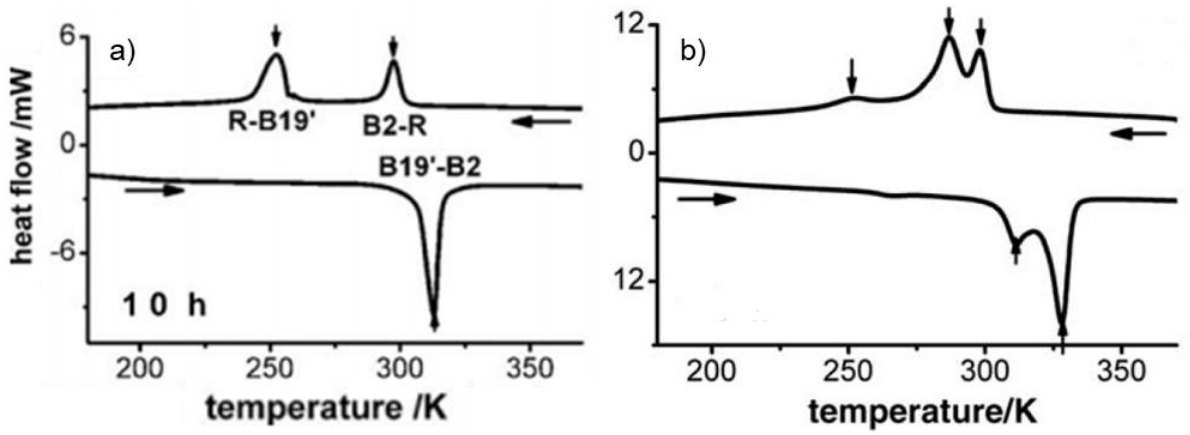

Fig. 13. DSC curves for a) Ti–51.5Ni single-crystal solution-treated at 1000°C for 1 h followed by water quenching and aging 450°C/10h and b) polycrystalline Ti–50.6Ni after solution-treated 1000°C/1h followed by water quenching and aging 450°C/24h [57].

However, three or even more peaks can be found in a DSC record of NiTi cooling (Fig. 13) suggesting a multi-stage transformation. Since no new phase was identified, a mechanism explaining this behavior was needed to find out. Explanation of the multi-stage transformation can be found in the heterogeneity of precipitation processes. As precipitation of Ni_4Ti_3 phase is favorable on grain boundaries (GB), Ni concentration in NiTi matrix is lower on grain boundaries than in the grain interior (GI). Consequently, B2-R-B19‘ transformation takes place on GB and only B2-B19‘ transformation takes place in the GI. The result is a three-stage transformation at three different temperatures. The effect is more pronounced in alloys with lower Ni excess (Fig. 14). For example, the nucleation rate in the GI is nine times lower than on GB in 50.6 at.% Ni alloy, yet the ratio of GB/GI nucleation rate is only 1.2 in 51.5 at.% Ni, where higher supersaturation increases the driving force for precipitation and the influence of GB is suppressed [57]. Three-step transformation can occur even in a NiTi single crystal with no grain boundaries. The reason is local heterogeneity of chemical composition given by precipitates with larger spacing (> 200 nm) as Ni is depleted around precipitates. At first, B2-R-phase transformation proceeds on the precipitate/matrix interface and then transformation to B19‘ martensite. Finally, martensite nucleates in areas farther from precipitates [57].

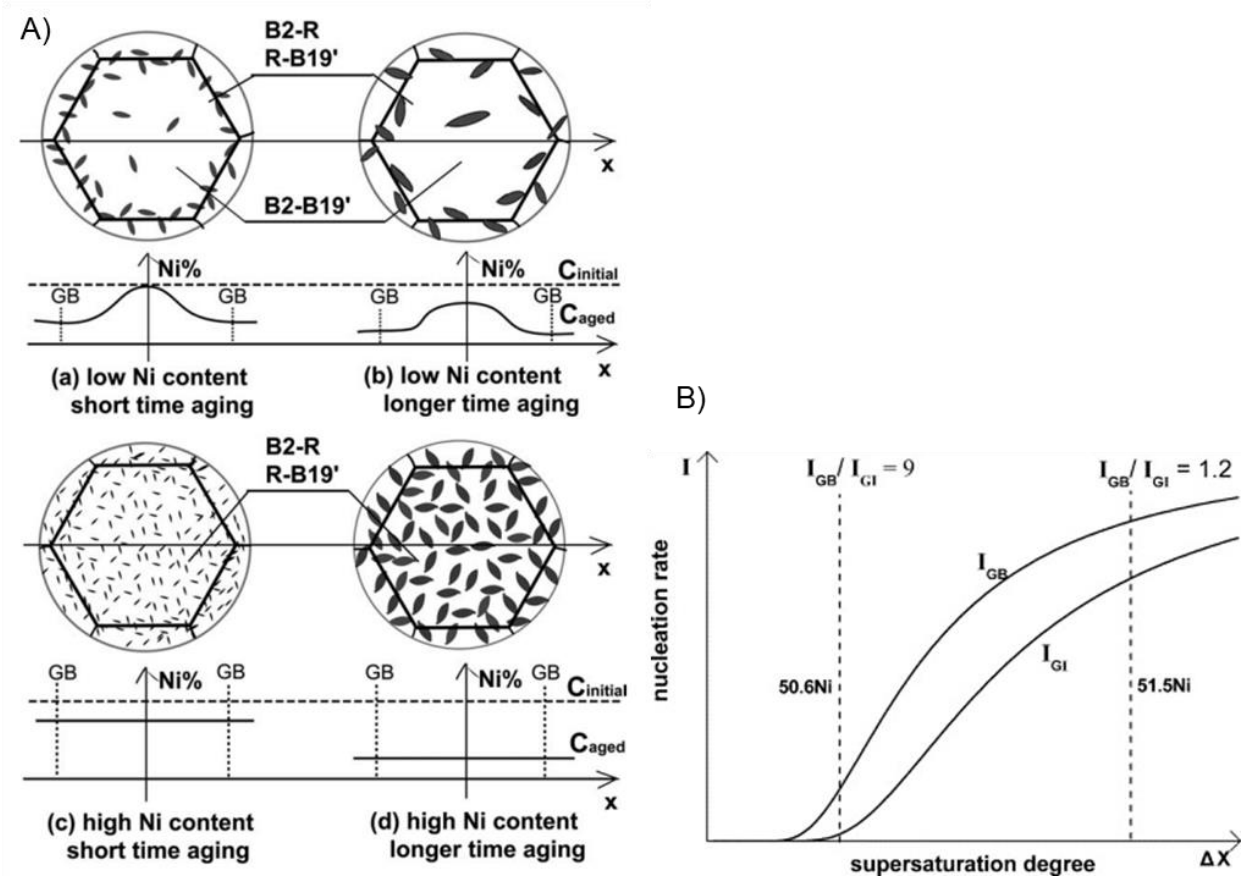

Fig. 14. A) Unified model for explaining the microstructure evolution at low Ni supersaturation (a) and (b) and high Ni supersaturation (c) and (d). It also explains both the three-stage and two-stage transformation behavior of supersaturated Ti-Ni solid solution. In the figure, $C_{initial}$ and C_{aged} curves represent the Ni profile of the initial (as-quenched) state and that after aging, respectively. GB denotes grain boundary. B) Schematic illustration for the relation between nucleation rate and supersaturation degree in grain interior region and grain boundary region. Supersaturation degree ΔX is defined by the solute (Ni) concentration beyond its solubility limit in the B2 Ti–Ni phase at a given aging temperature. The nucleation rate at the grain boundary and the grain interior is indicated by I_{GB} and I_{GI}, respectively. [57]

1.5 Fatigue of NiTi alloys

The fatigue of NiTi alloys can be classified into two categories: functional and structural fatigue. Functional fatigue is related to the degradation of thermomechanical response, e.g. the evolution of transformation temperatures, stresses, and strains. Structural fatigue is meant in its standard sense- an accumulation of dislocations and internal stresses, crack nucleation, and growth until the failure [78]. The cyclic evolution of mechanical properties investigated since the nitinol discovery in the 1960s. However, superelastic fatigue life is not sufficient for many applications yet. It is known that the superelastic response of NiTi alloy evolves during superelastic cycling and how this is related to the evolution of microstructure and internal stresses to some extent [36]. It is well known that the stress-induced martensitic transformation in superelastic NiTi tends to be accompanied by unrecovered strain as lattice defects are introduced upon thermomechanical cycling, microstructure evolves irreversibly, and functional properties gradually change upon cycling [11][34][36][39]. Although higher functional degradation is commonly associated with inferior fatigue performance as higher temperatures,

transformation stresses, and strains lead to the deterioration of both functional properties and fatigue life [1][25][28], the rate of deterioration and coupling between functional and structural fatigue and microstructure changes during fatigue life need to be further examined for various microstructures.

1.5.1 Functional degradation

Evolution of the stress-strain response

Decrease in transformation stresses is a well-known phenomenon occurring during superelastic cycling of the NiTi alloy [25][79][80]. These changes are caused especially by redistribution of inner stresses in differently oriented grains, an increase of dislocation density, and an increase of a residual martensite volume fraction [36][79]. It is also important to consider that superelastic deformation is realized by martensite band front propagation in the uniaxial tension (Fig. 15a) [10][26]! Austenite and martensite have different crystal structures and deformation is not homogenous, especially in the martensite band front (the strain of the martensitic part is almost ten times higher in tension loading). This kind of discrepancy is minimized by a sharp and thin interface, which is inclined approx. 55° to the loading axis in NiTi ribbons or films [82]. On the contrary, the interface has a shape of a rounded cone in NiTi wires loaded in uniaxial tension shown in Fig. 15b, where the distribution of stresses is evaluated by three-dimensional X-ray diffraction (3D XRD) microscopy. Although nominal stress is 420 MPa, 600 MPa stress was measured in surface grains and only 250 MPa in the middle of the cone, which is the key feature of the martensite bend front in NiTi wires, revealed in [26]. The next feature of functional degradation is a decrease in transformation strain and accumulation of unrecovered strain ε_{us} as well (Fig. 16). Change in transformation stress cannot be fully avoided during superelastic cycling, however, the accumulation of ε_{us} and dislocation activity can be greatly reduced in a nanograin microstructure (Fig. 8,9,16). Since fatigue failure occurs after stabilization (100-200 cycles) of functional properties, it seems that functional fatigue is not directly connected with fatigue failure. However, small increments of permanent strain and other features of functional degradation can be detected in a whole fatigue life [11][34].

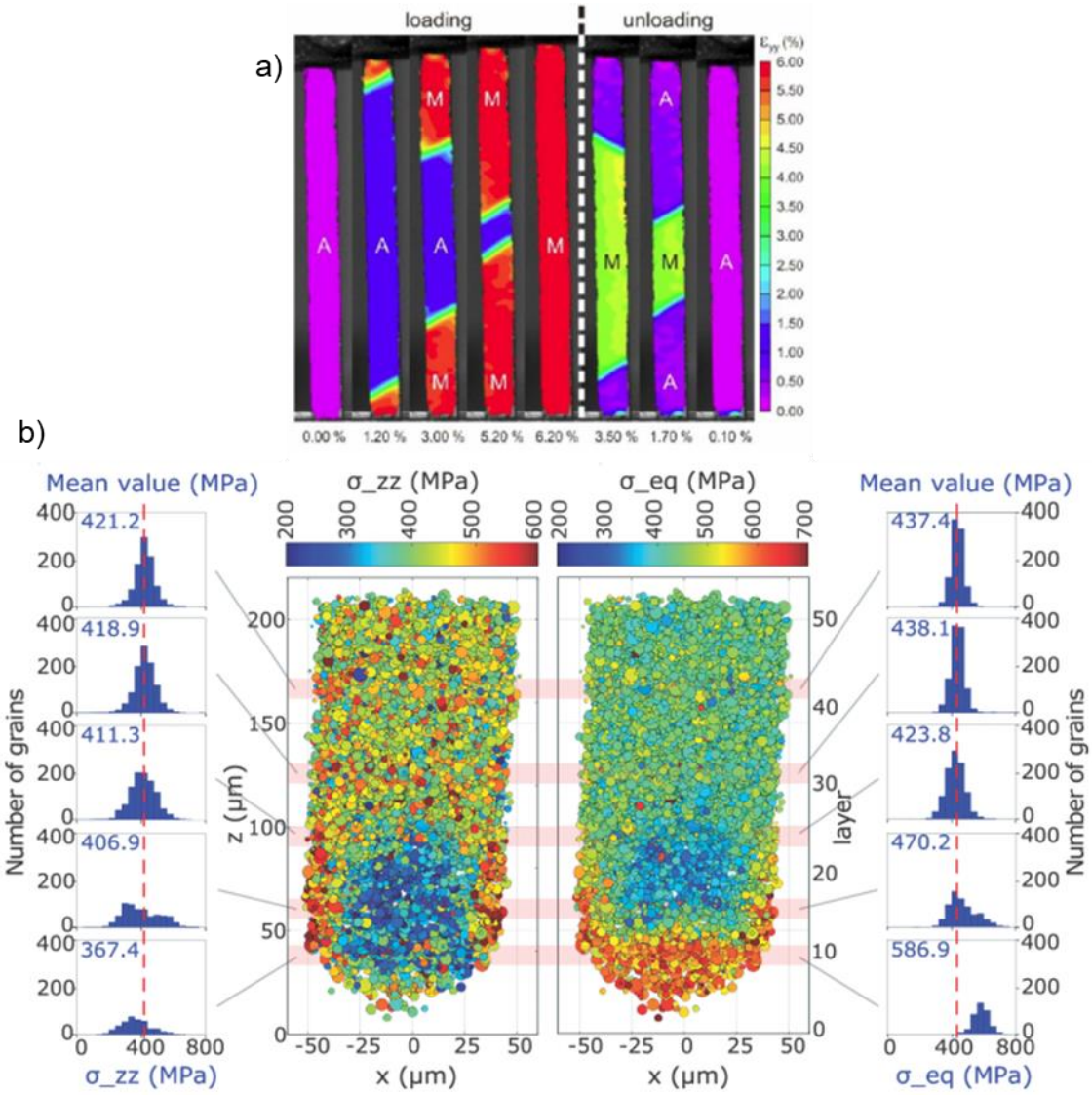

Fig. 15. a) Localization of martensitic transformation in the uniaxial superelastic loading of a NiTi ribbon evaluated by DIC [81]. b) Distribution of internal stresses in austenite and shape of austenite/martensite interface evaluated by 3D-XRD (longitudinal cut of 100 μm NiTi wire) [26].

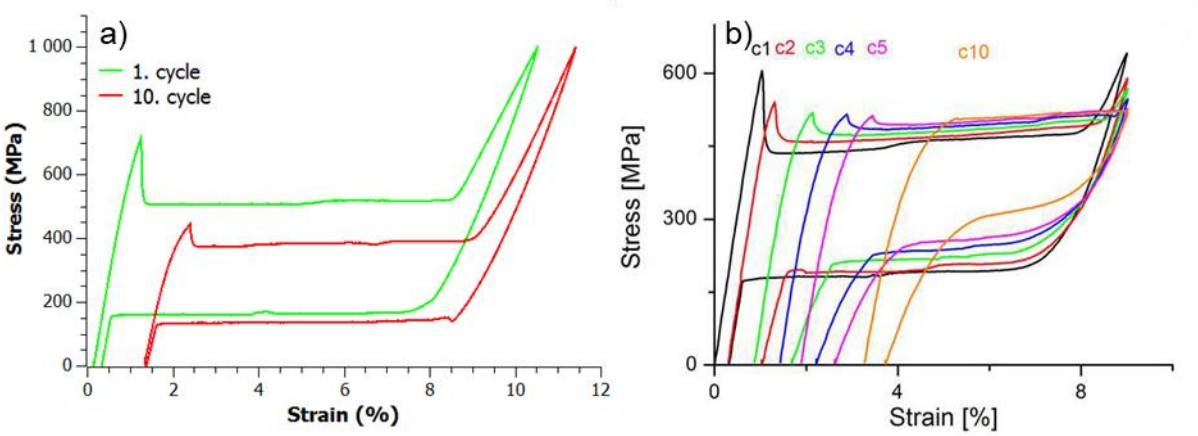

Fig. 16. Functional degradation in superelastic cycling. a) The first and tenth superelastic cycle of NiTi wire at 20 °C after electric pulse heat treatment (160Wmm^{-3}/13ms). b) Ten superelastic cycles plus heating above 100 °C in between cycles to release residual martensite (pulse heat treatment 160Wmm^{-3}/20ms) [73].

Results of thermomechanical loading tests reaching into high temperature/high stress regime reveal further evidence of NiTi deformation behaviors due to the martensitic transformation coupled with plastic deformation. First of all, the unrecovered strains generated separately by the forward martensitic transformation ε_{us}^{F} upon cooling under large stress and by the reverse martensitic transformation ε_{us}^{R} upon heating under large stress (Figs. 17,18) were investigated using the "Bypass Approach", introduced recently in [34]. They reported that: i) plastic deformation accompanies martensitic transformation only when it proceeds under external stress; ii) the amount of unrecovered strain increases exponentially with increasing temperature and stress; iii) surprisingly, larger unrecovered strains are generated by the reverse transformation than by the forward one (Fig. 17d,18d). This means that a NiTi wire is irreversibly damaged/elongated even in the unloading part of a superelastic cycle.

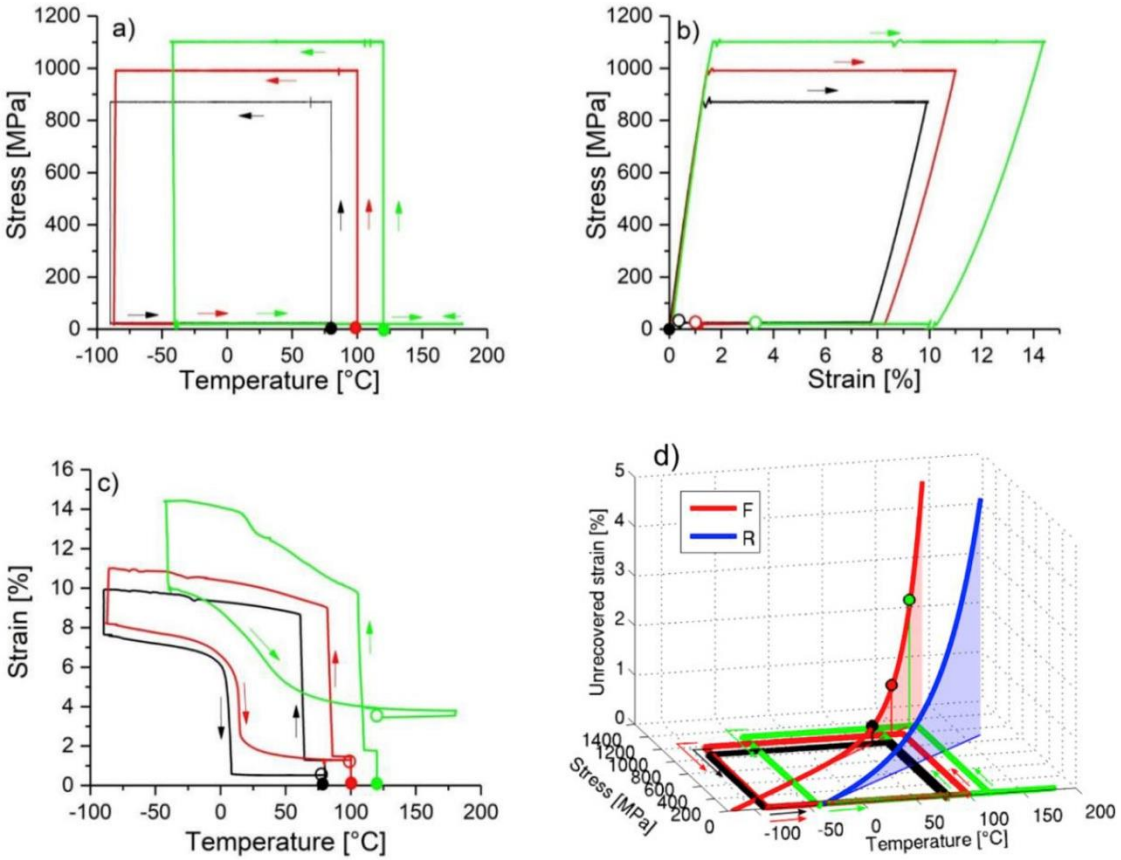

Fig. 17. Unrecovered strains generated by the forward martensitic transformation upon cooling under stress (red exponential in d) as evaluated from the stress-strain-temperature response of NiTi wire in 3 thermomechanical loading tests composed of loading until 870, 990, and 1100 MPa at ~100 °C, cooling under constant stress 870, 990 and 1100 MPa to induce A→M transformation, unloading to 20 MPa and stress-free heating back to the starting test temperature. The test course can be tracked by following arrows in (a,b,c) from the solid circle to the open circle.[39]

The results of the series of bypass tests for martensitic transformations proceeding upon cooling (Fig. 17) or heating (Fig. 18) under constant tensile stresses below 1 GPa are essentially the same as those reported in [34], only the unrecovered strains are larger. When reaching the high temperature – high-stress regime above 1 GPa applied stress, however, the observed stress-strain-temperature responses become quite different. The green curve in Fig. 17 and magenta in Fig. 18 represent extreme loading conditions at 1100MPa stress of NiTi wire with the tensile strength of 1300 MPa. Besides the strain evolving during the martensitic transformation upon

cooling under 1100 MPa, significant tensile strain develops further upon cooling in the martensite state further below 100 °C (green curve in Fig. 17c). Furthermore, tensile strain increases upon heating at 1100 MPa stress instead of decreasing (magenta curve in Fig. 18c), as commonly observed in NiTi actuator tests.

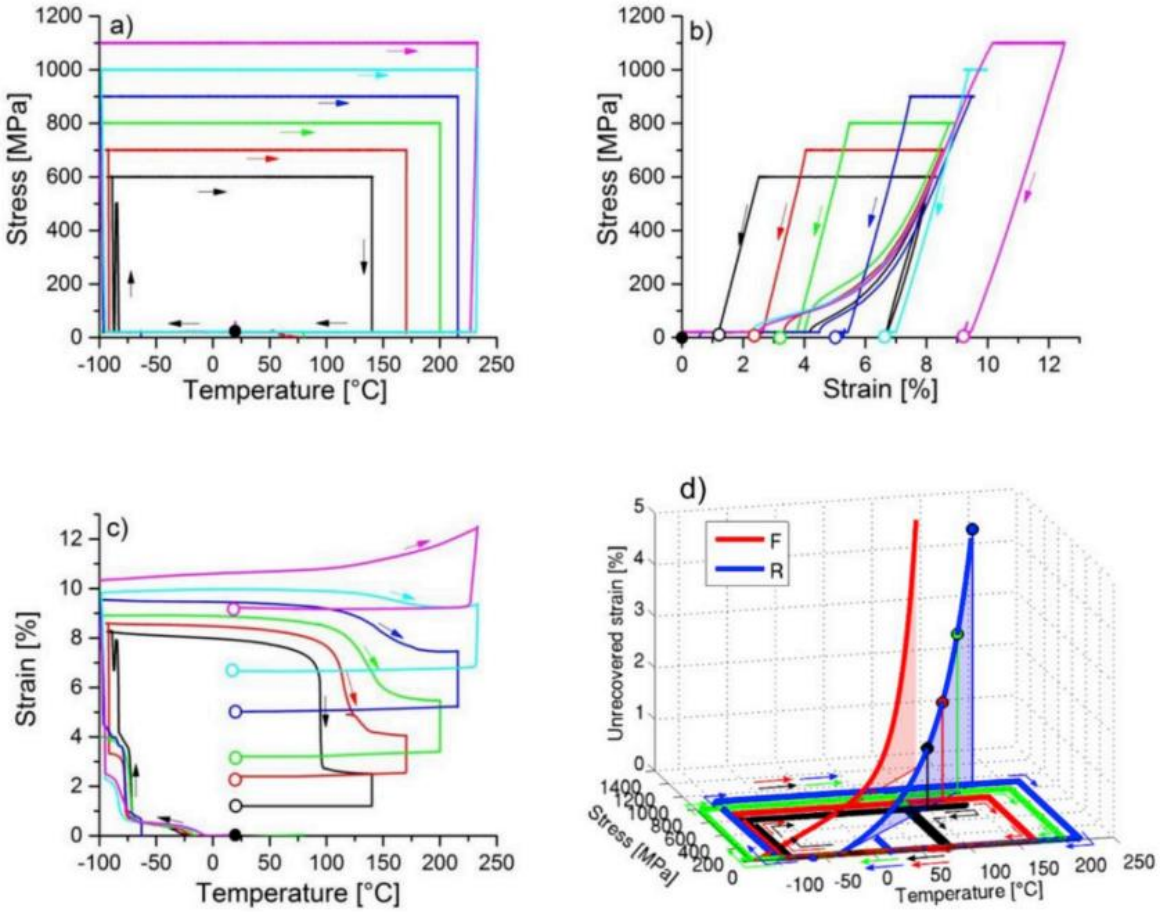

Fig. 18. Stress-temperature dependence of unrecovered strains generated by the reverse martensitic transformation upon heating under stress (blue exponential in d) as evaluated from the stress-strain-temperature response of NiTi wire in thermomechanical loading tests consisting in stress-free cooling to -100 °C, loading till 600, 700, 800, 900, 1000 and 1100 MPa, heating under constant applied stress till fully austenitic phase (or 250 °C), unloading to 20 MPa and cooling to the starting test temperature. The test starts (solid circle) by loading the wire to the required stress and cooling under stress. I ts course can be tracked by following arrows in (a,b,c). [39]

Deformation twinning

The deformation twinning in oriented B19' martensite [83][84][85] occurs upon tensile loading of NiTi wires when the applied strain exceeds the martensite yield limit [40][83] or as an intermediate step of the stress-induced B2→B19'→$B2^T$ ($B2^T$ – twinned austenite) sequential martensitic transformation proceeding at elevated temperatures and stress [86]. The B2→B19'→$B2^T$ transformation is activated, e.g. upon thermal cycling under large stress [87], upon constrained heating of the deformed NiTi [38], or upon severe plastic deformation of NiTi [88][89][90]. As revealed in [40], the deformation twinning in oriented martensite results in

permanent deformation and suppresses the recoverability of transformation strains in tensile tests at elevated temperatures. In a contrast, dislocation slip, while it also causes plastic deformation, does not restrict the recoverability of transformation strains.

At the single crystal level, the B2→B19'→$B2^T$ transition path can be seen as a sequence of kinematically compatible structures evolving in the crystal lattice under increasing stress. This sequence is outlined in Fig. 19b. The crystal lattice is initially in the austenite state, which represents a reference configuration with zero strain in the loading direction. Under the action of the external loading, the transformation proceeds discontinuously towards the martensitic structure. The austenite lattice transforms into a laminate of martensitic variants fulfilling the requirement for strain compatibility at the habit plane. If we assume a single stress state everywhere and proper orientation of the martensite lattice with respect to the loading, a single variant of martensite forms from the martensite laminate under the action of this stress. The elongation of the crystal lattice in the direction of the loading provided by the single martensite variant is denoted as $\varepsilon^{B2\rightarrow B19'}$. This is the maximal strain the lattice can attain via cubic to monoclinic martensitic transformation. The continuous elastic distortion of austenite and martensite is not considered in Fig. 19. The maximal strain, together with the polycrystal texture, controls the length of the transformation plateau in fully recoverable tensile tests on polycrystalline NiTi wires at relatively low temperatures.

Upon further loading above the stress plateau, the martensite single crystal in Fig. 19b(b) undergoes continuous elastic distortion and further plastic deformation can theoretically proceed via dislocation slip in stress-induced martensite. Alternatively, a further inelastic strain may appear in a form of "dislocation slip assisted deformation twinning (plastic twinning)". The {20–1} deformation twinning reported in the literature is a good example [83][84]. The {20–1} plastic twins appearing in the martensitic lattice cannot be described by a continuous mapping of the reference configuration in the Cauchy-Born sense [91] - i.e. these twins are not predictable by the mathematical theory of martensitic microstructures. Instead, the formation mechanism of these twins comprises of both shearing and shuffling [83] and the resulting twinned martensite thus loses its tight lattice correspondence to the initial parent austenite lattice. Breaking the lattice correspondence to the parent austenite lattice (its particular orientation) gives the martensitic lattice an additional degree of freedom and potential for additional elongation in the sense of Fig. 19b(c). The deformation twinning enables tilting and rotation of the crystal lattice, such that the maximal transformation strain can get better aligned with the applied loading and the lattice is reaching the total strain of $\varepsilon^{B2\rightarrow B19'+B19'^T}$ (B19'^{T}- {20–1} martensitic deformation twin) as shown in Fig. 19b(c). The experiments seem to suggest that small inelastic strains caused by the {20–1} twinning at low temperatures are partially recoverable at low temperature (Fig. 20), but get gradually irrecoverable with increasing temperature above A_f.

A direct consequence of this new degree of freedom is the possibility of reverse transition of the {20–1} twinned martensite into twinned B2 austenite upon forward loading, as outlined in Fig. 19b(d). Additionally, upon subsequent unloading and/or heating, the remaining neighboring martensite lattice will transform to the parent austenite lattice, as given in Fig. 19b(e). As the two twin-related variants of martensite in Fig. 19b(c,d) correspond to two different reference configurations, the reverse transition proceeds into a mixture of two differently rotated austenitic lattices. In this way, the {20–1} twins are inherited into austenite

as {114} austenite twins [92][93] - i.e. the tilting of the martensite lattice due to the {20–1} twinning is adopted by the cubic lattice of austenite (Fig. 20).

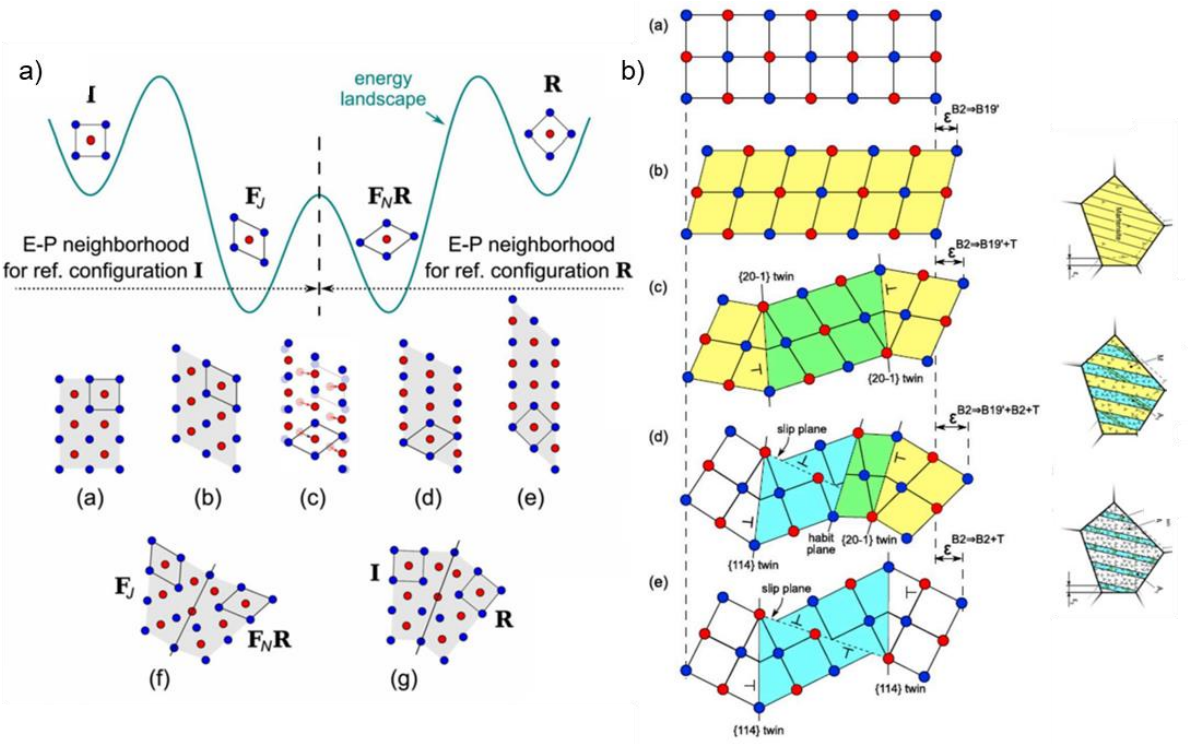

Fig. 19 Potential energy landscape for martensitic transformation and deformation twinning in NiTi (A) [94]. The high symmetry austenite phase appears in the original reference configuration I and a rotated configuration R at the same energy level in mirror symmetry with respect to the center. The low symmetry martensite phase F_J (F_NR) forms from the austenite phase I (R) via martensitic transformation upon cooling by overcoming the energy barrier between I and F_J (R and F_NR). The martensite variant F_J belonging to the Ericksen–Pitteri neighborhood of I (b) may form the martensite variant F_NR, belonging to the E–P neighborhood of R (d) by deformation twinning involving a combination of plastic shearing and shuffling (c). Parent phase with reference configuration R (e) may be obtained from the F_NR by reverse martensitic transformation on heating, unloading, and/or further tensile loading. The {20–1} twin interfaces in the martensite phase (f) are converted into {114} twin interfaces in the austenite phase (g) after the reverse martensitic transformation. The atomic configurations appearing successively upon tensile loading at various temperatures B the initial austenite lattice (a); the oriented B19' martensite phase (b); the deformation twinned B19' martensite phase (d); twinned austenite (e) yield increasing respectively effective strain (right). Sketches of polycrystal grains outline the microstructure in the wire at the peak stress at three different temperatures. [95]

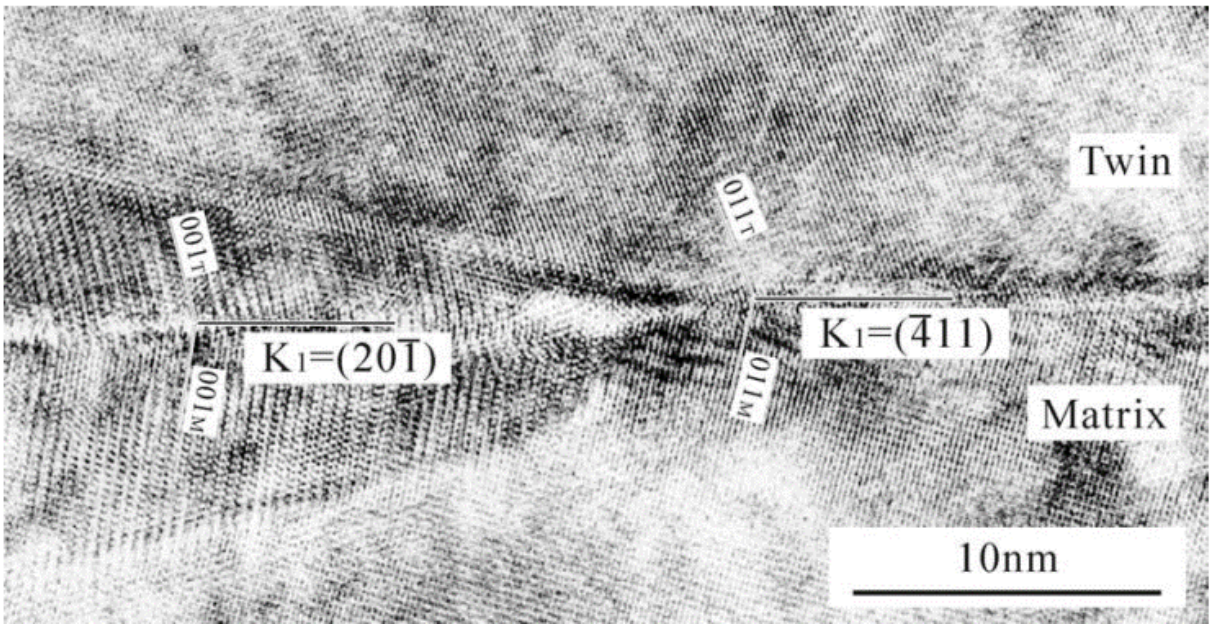

Fig. 20. Two-dimensional lattice image of the partially reverse transformed Ti–50.6at%Ni alloy deformed in the fully martensitic state, showing continuity of K1 planes between $(20\text{-}1)_{B19'}$ twin in retained martensitic phase and $(\text{-}411)_{B2}$ twins in reverse transformed parent phase. The electron beam is parallel to $[010]_{B19'}$ and $[01\text{-}1]_{B2}$. [92]

An in-situ high-resolution digital image correlation investigation during uniaxial tensile deformation reveals the recoverable and the non-recoverable strain mechanisms in a $Ni_{51}Ti_{49}$ alloy with a mean grain size of 35 µm (Fig. 21). Besides the recoverable strain by martensitic transformation, non-recoverable strain is accommodated by dislocation slip in the austenite and austenite twinning following the sequence: B2-B19′-$B2^{T}$. Finally, small amounts of retained martensite are detected, contributing to the non-recoverable strain. The coexistence of stress-induced martensite, slip, and twinning in martensite/austenite results in deformation bands with high axial strain [96]. These processes referred to as grain refinement in [47][48]w have the potential to affect fatigue life (the effect of grain size and internal stresses will be discussed later in section 1.5.3).

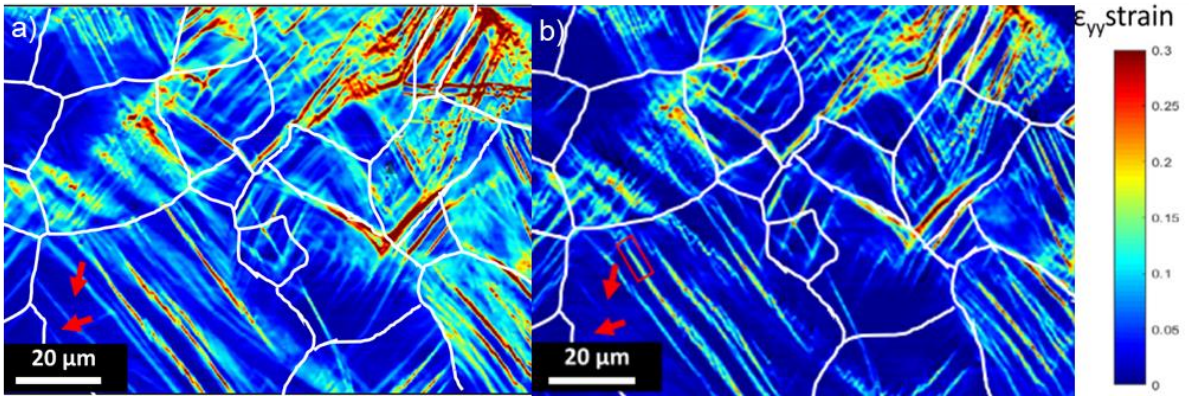

Fig. 21. a) HR-DIC map at maximum load (i.e. average strain of 10%) and b) Map of residual strains after complete unloading. [96]

1.5.2 Aspects of NiTi fatigue life

Transformation stresses and temperature

A boundary between elastic and superelastic loading of NiTi alloy is also the boundary between high-cycle and low-cycle fatigue. In terms of the number of cycles to failure (N_f), it is approx. 10^3-10^4 cycles [27][31][78]. However, values of stress or strain, where the boundary is, depend on factors such as NiTi composition, heat treatment, and testing temperature. Strain amplitude applied in a fatigue test affects fatigue performance, like for example in rotary-bending and torsional fatigue experiments [21][23][24] or even in tension [25], if transformation stress plateau is lost due to functional degradation. On the other hand, fatigue life is less sensitive to the strain amplitude and mean strain within the plateau range in tensile tests [10][97]. An explanation can be found in the localization of martensitic transformation shown in Fig. 15 [26][81]. Although macroscopic strain is below the end of plateau strain, local strain beyond martensite bend front is at the level of transformation strain regardless of macroscopic strain. In fact, this kind of loading regime is similar to a full superelastic loading of a shorter sample. Similar insensitivity to strain amplitude was observed in rotary-bending tests in [9][27][28].

Different fatigue curves of NiTi wires subjected to the rotating-bending test can be seen in Fig. 22 as the result of various Ni content. The red curve shows the fatigue life of austenitic wire, where martensitic transformation does not occur, which causes serious shortening of fatigue life at high strain amplitude (ε_a). On the contrary, shape memory (martensitic) wire shows two orders of magnitude higher fatigue life at the same testing temperature. The reason is the capability of martensite to accommodate large strain by twin reorientation, which requires low stresses (~ 100 MPa [27][49]). The fatigue life of superelastic wire (pink curve) is located in between the previous curves. Superelastic wire behaves as pure austenite at low strain amplitude. Then, the region insensitive to strain amplitude occurs in the range around 3-8 % strain amplitude (region of transformation strain). Finally, the fatigue life of the superelastic wire resembles the performance of the martensitic one at a 10 % strain amplitude region [27]. From that point of view, testing temperature (together with NiTi composition) plays a crucial role in NiTi fatigue life [23][28][29]. Moreover, an increase in fatigue life is observed with decreasing testing temperature [23], which is expected considering Clausius-Clapeyron relation and decrease in transformation stresses. In other words, the strain amplitude insensitive region in Fig. 22 shifts to the right with decreasing temperature. Another unusual fatigue feature related to martensitic transformation is the low sensitivity of fatigue life on mean strain at low strain amplitude in superelastic plateau [97].

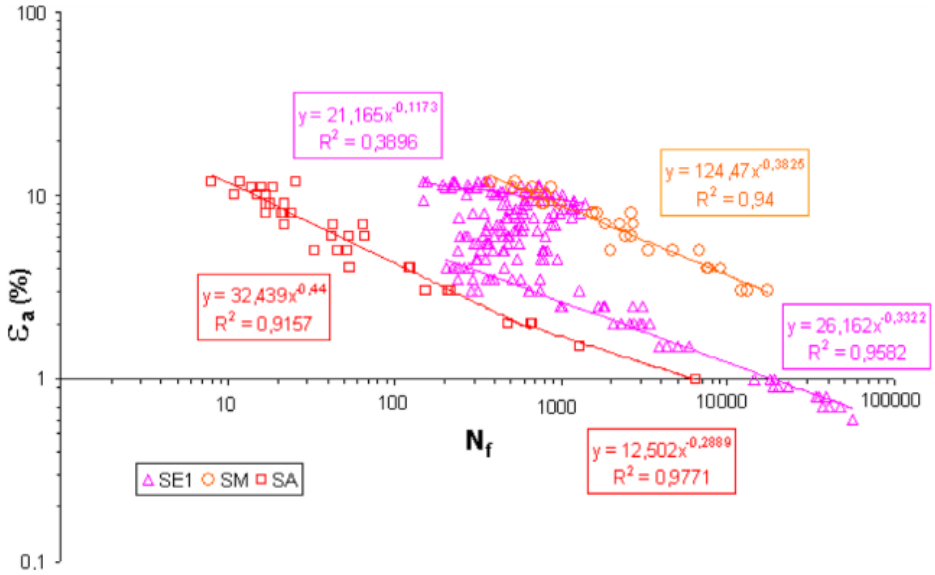

Fig. 22. Effect of phase transformation temperatures: ε_a-N_f curves for superelastic (pink), austenitic (red), and martensitic (orange) wire in the rotating-bending test. [27]

Precipitates

Ni_4Ti_3 precipitates significantly affect the mechanical properties of NiTi alloy as mentioned in section 1.4. Thus, the effect of aging on fatigue life has been studied to find out the benefits of Ni-rich precipitates. It was found out that coherent 10 nm Ni_4Ti_3 precipitates inhibit dislocation activity during superelastic cycling and decrease the accumulation of permanent strain (functional degradation) compared to samples without precipitates. Thus, it can be concluded that strain fields of coherent precipitates protect the NiTi matrix against damage accumulation to some extent. On the other hand, no effect has been observed in samples with 500 nm precipitates that are not coherent with the NiTi matrix [22]. Fatigue life of aged samples was reported three times higher in [21] at higher strain amplitude, where martensitic transformation occurs. Except for decreasing dislocation activity, Ni-rich precipitates also decrease Ni content in the matrix. Therefore, superelastic cycles can be performed at lower stresses, which is beneficial for fatigue performance in the same way as the decrease in testing temperature.

Impurities in NiTi alloys

The fatigue life of the NiTi alloy is negatively affected by the presence of contaminating elements (oxygen and carbon). Well-known inclusions are carbide particles TiC and Ti_2Ni intermetallic phase with a high concentration of oxygen in solid solution (often denoted as O-rich or oxide particles) [31][98]. The crystal lattice of O-rich particles is FCC and no orientation relation with NiTi matrix has been found [63]. Carbides have BCC lattice [99]. Moreover, Ti is preferentially depleted from the matrix to create O-rich and C-rich particles, which decreases the transformation temperatures of NiTi alloy [31].

These inclusions exhibit significantly distinct material properties from the NiTi matrix. First of all, C-rich and O-rich particles are not as superelastic as the NiTi matrix. Another problem is the high elastic modulus of these phases compared to the NiTi alloy, which causes incompatibility even in the elastic loading region of austenite. Elastic modulus is around 150

GPa in the O-rich phase and 380-450 GPa in the TiC phase [31][99]. The high hardness of the ceramic particles also gives rise to micro-cracks nucleation (particle/void assessment) during cold working, which is seen in Fig 23. Furthermore, O-rich particles seem to have a more negative impact on NiTi fatigue life due to larger dimensions and weaker cohesion with the matrix, which causes a 5 times higher number of the particle/void defects than TiC particles, according to [31]. Moreover, the length of micro-cracks created on O-rich particles during cold working was one order of magnitude higher. In general, inclusions weaken the structural integrity of the NiTi alloy and give rise to fatigue crack nucleation.

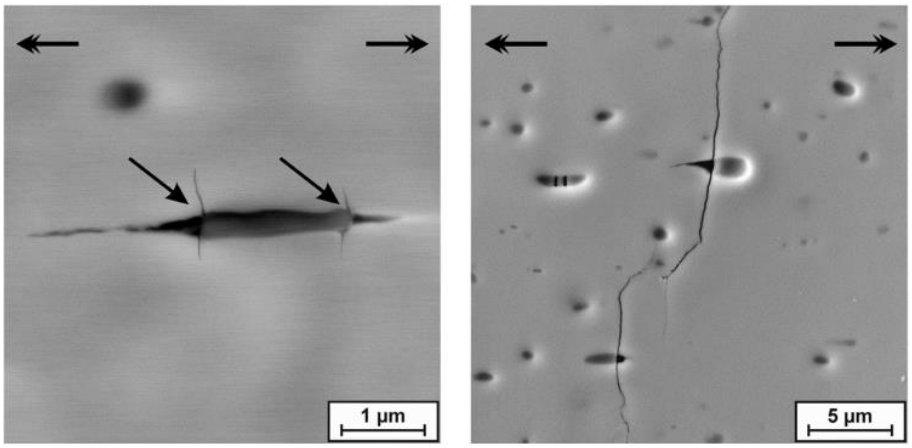

Fig. 23. SEM of crack initiation sites (carbides- left and oxides- right). The double-tip arrows indicate the longitudinal wire direction. [31]

1.5.3 Fracture mechanics of NiTi

Fractography

Fractography provides information about material damage through the identification of fractographic features on fracture surfaces. Determination of the reason for fatigue failure is frequently required as suggested in the previous sections. Examples of analysis of fatigue fracture surfaces will be discussed in this section.

The fatigue fracture surface of a NiTi wire after the rotating-bending test is shown in Fig. 24a. The nucleation site of fatigue crack, area of fatigue crack propagation, and the final fracture can be identified together with the macroscopic and microscopic direction of crack propagation. Pronounced striation fields are visible in the cyclically-loaded area of fatigue crack propagation. Value of striation spacing indirectly expresses a local rate of fatigue crack growth according to formula

$$v=D.s, \qquad (3)$$

where v is crack growth rate, s is striation spacing and D is the coefficient depending on material properties, crack length, loading conditions, etc. [100]. The effect of strain amplitude (ε_s=0.8 % and 1.5 %) on striation spacing is illustrated in Fig. 24b). Higher strain amplitude causes higher striation spacing and crack growth. However, striations are not created necessarily in each cycle, especially in the early stages of fatigue crack growth, and more sophisticated methods are needed for the identification of idle cycles [100]. Lastly, the area of final fracture (Fig. 24a(3)) is characterized by ductile dimples caused by microvoid coalescence nucleating on the matrix/inclusion interface.

The fracture surface of CT specimens with large grains (~ 1 µm) mainly shows dimples indicating a dominant ductile fracture. For smaller grains (~ 100 nm), the fracture surface is characterized by a mixture of dimples and cleavage planes. With further grain size reduction, the tendency of the cleavage increases in the fracture process.[54]

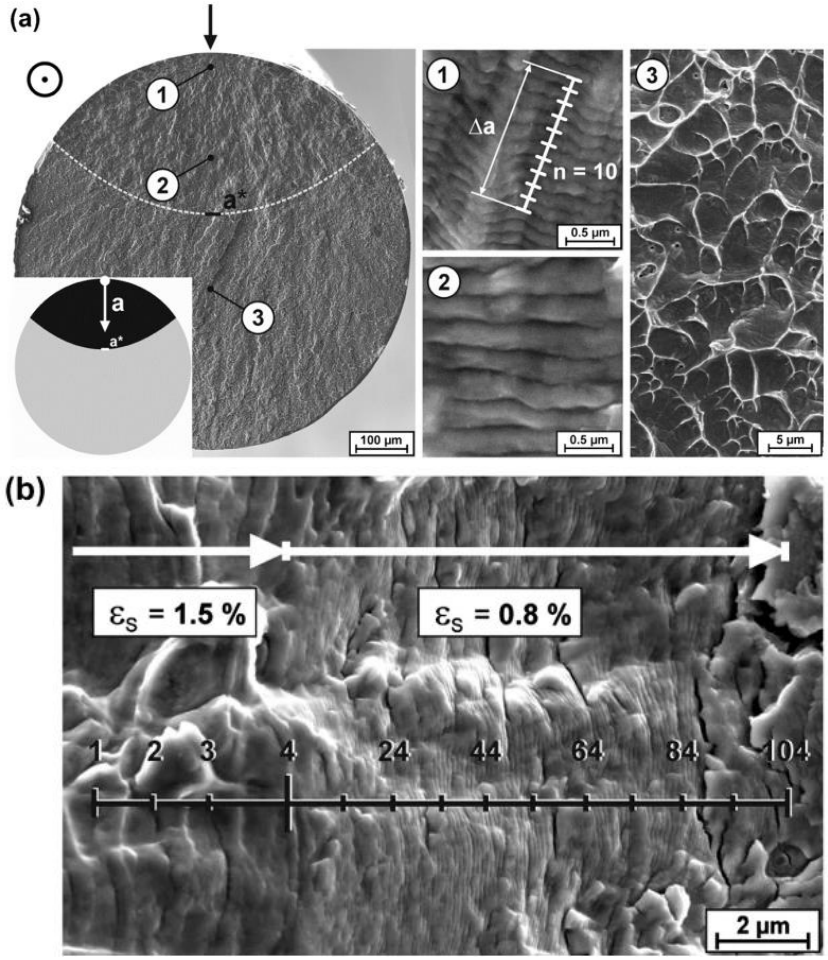

Fig. 24. (SEM) (a) Fatigue fracture surface of wire after the rotating-bending test. White arrows denote crack propagation direction and the black arrow denotes crack nucleation site. The dotted line separates the area of fatigue crack propagation and the final fracture surface. (b) Striation fields with different spacing as a function of strain amplitude. [31]

The nucleation site of a fatigue crack is appreciated information, providing a clue to the increase in fatigue life. The most frequent fatigue crack nucleation sites in the NiTi alloy are TiC carbides and O-rich particles (Figs. 23 and 25) and the decrease in size and concentration of the impurities increases the fatigue life of the superelastic NiTi wires [31][32]. As the inclusions are not superelastic, separation of the inclusions from the NiTi matrix during superelastic cycling is reported [32][101]. As shown in Fig. 25, only the dimple remains in the crack nucleation site. Even a high number of fatigue cracks can independently nucleate in the NiTi during superelastic loading throughout the whole length of the tested sample, as shown in Fig. 26.

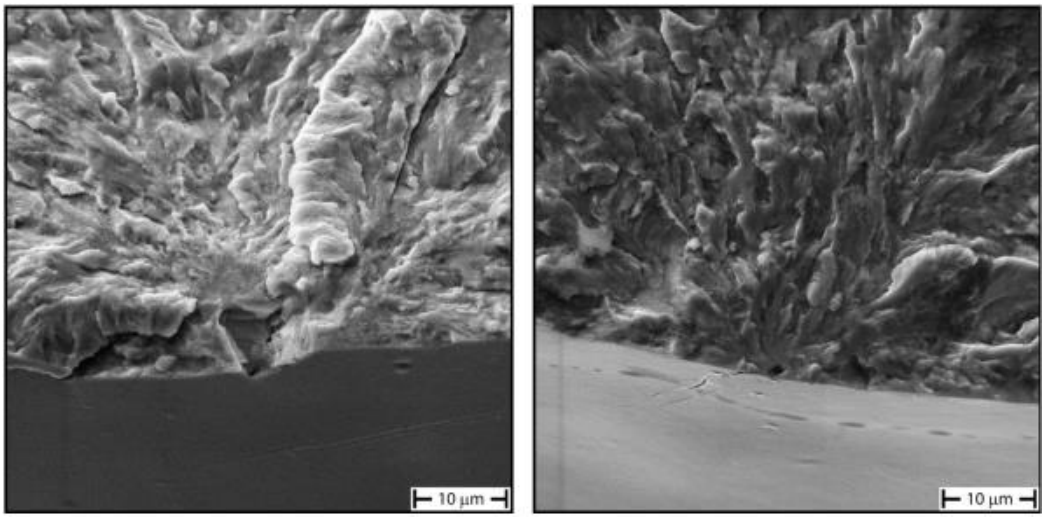

Fig. 25. (SEM) Initiation of crack on a near-surface inclusion: left micrograph- lower purity sample, right micrograph- high purity sample. [32]

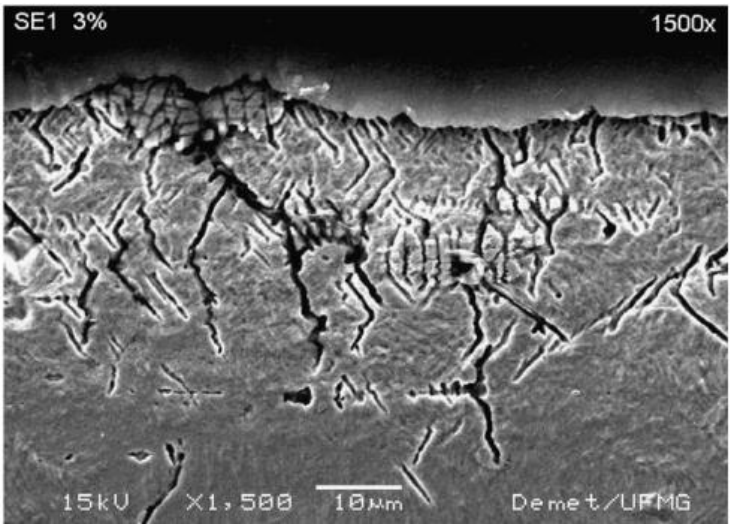

Fig. 26. (SEM) Longitudinal section of superelastic wire after fatigue test with 3% strain amplitude. [27]

Crack tip stress field

Surface defects such as cracks or notches act as stress concentrators and give rise to multi-axial stress, even in uniaxial loading. The level of stress concentration is characterized by the so-called stress concentration coefficient

$$\alpha = \frac{\sigma_{max}}{\sigma}, \tag{4}$$

where σ_{max} is maximal stress and σ is mean stress (in a fractured or in an intact cross-section of material) [102]. Stresses at a notch or crack tip can highly exceed nominal stress, but the upper limit is given by yield stress and tensile strength of a material.

A stress intensity factor *K* characterizing the stress and displacement fields near to a crack tip is very often used in fracture mechanics. A general formula for the K factor is:

$$K = \sigma * \sqrt{\pi a} * f\left(\frac{a}{W}\right), \tag{5}$$

where σ is an applied load, a is a crack length, W is the width of a tested specimen, and $f\left(\frac{a}{W}\right)$ is a geometric factor of the order of unity [103].

In addition to yield stress and tensile strength, transformation stresses are important for NiTi behavior at a crack tip. As shown in Fig. 27a), superelastic NiTi alloy resembles ideal elastoplastic material in a certain deformation range, and values of transformation stresses are a function of various variables (temperature, Ni concentration, or annealing), which consecutively affects the shape and size of a crack tip zone. The size and shape of an actual crack tip zone, represented by the black color on synchrotron X-ray microdiffraction strain maps, are shown in Fig. 27b. The actual shape of the transformation zone is significantly affected by grain misorientation complicating martensite propagation and even by austenite/martensite compatibility on the interphase [26].

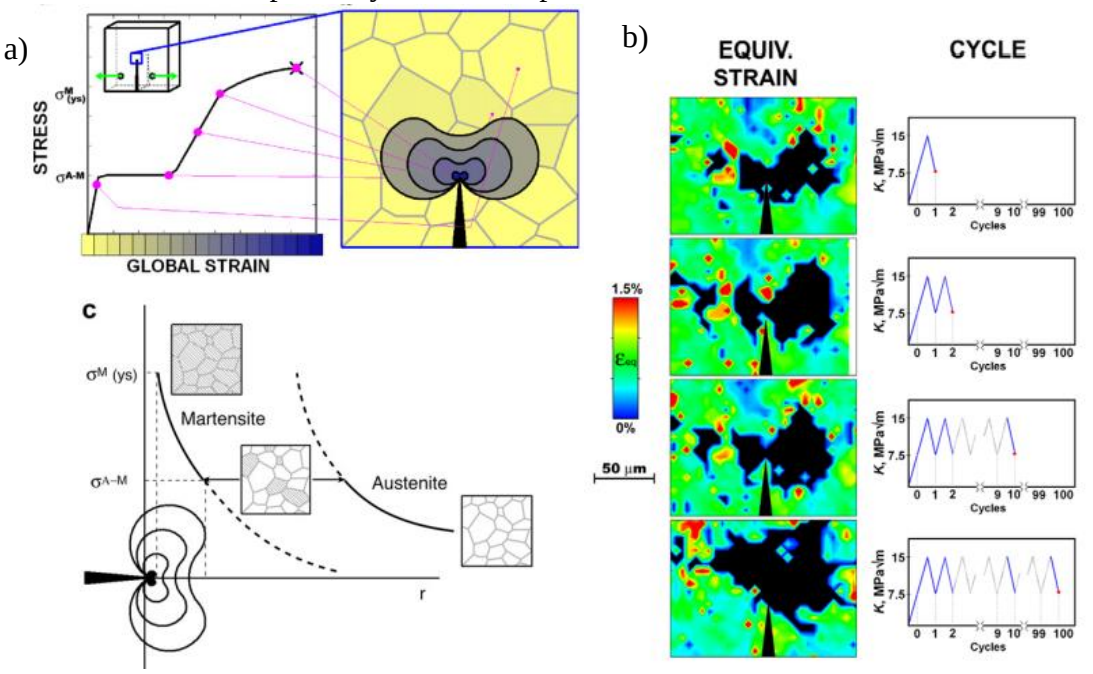

Fig. 27. a) Model of stress and phase distribution at the crack tip of superelastically loaded NiTi alloy, b) Local equivalent strain map evaluated by micro XRD showing the actual transformation zone at the crack tip (transformed martensitic grains are not imaged by this method and so they are in black). [103]

Another possibility to observe a plastic and transformation zone at a crack tip is digital image correlation (DIC). The utility of this method is increased in combination with scanning electron microscopy (SEM DIC) [104][105]. Imaging of the strain field at the NiTi crack tip is shown in Fig. 28, where the effect of grain size is clearly proven and samples with small grains exhibit much smaller transformation and plastic zone at the crack tip as transformation stresses are higher and transformation strain lower. This also proves the importance of a final microstructure and heat treatment. Another utilization is in-situ tracking of propagation of martensite bend front especially in complicated shapes loaded by multiaxial stresses.

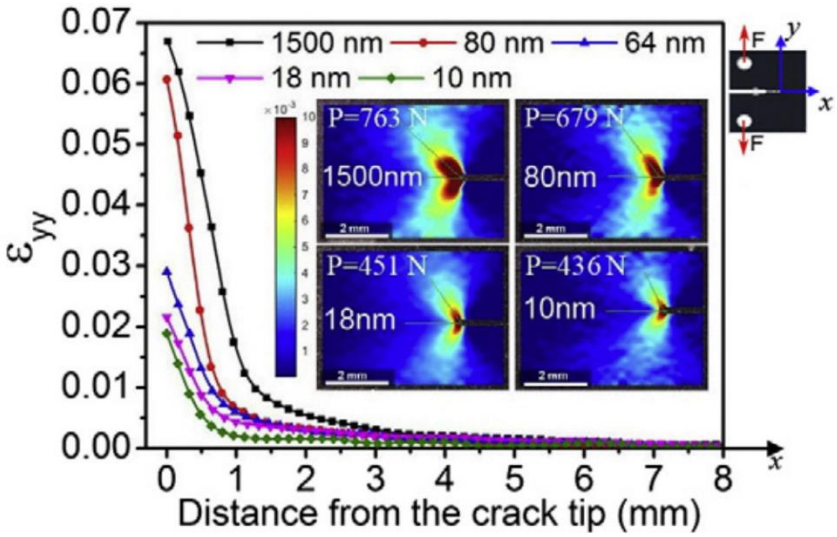

Fig. 28. Grain size effect on the strain distribution at the crack tip of CT samples. [54]

Factor affecting crack tip zone and crack propagation

Except for the notch effect, martensite bend front is affecting stress distribution in NiTi as well. Although nominal stress is 420 MPa, 600 MPa stress was measured in surface grains and only 250 MPa in the middle of the cone, which is the key feature of the martensite band front in NiTi wires revealed in [26]. This kind of stress concentration on the wire's surface could be a crucial factor in undesired fatigue failure of superelastic components. Moreover, NiTi alloy exhibits a very low amplitude of threshold stress intensity factor ΔK_{th} needed for crack propagation, and especially the cold-worked NiTi is comparable with ceramic materials. Although heat treatment improves ΔK_{th}, even hot-rolled NiTi alloy tested in [106] shows lower ΔK_{th} than other tested materials used in medical implants (Fig. 29). Influence of temperature and asymmetry of the loading cycle (stress ratio) on ΔK_{th} were tested in [107], where $Ni_{49.9}Ti_{50.1}$ CT samples were tested after annealing at 750°C/1h. The beginning of fatigue crack growth curves is shown in Fig. 30.

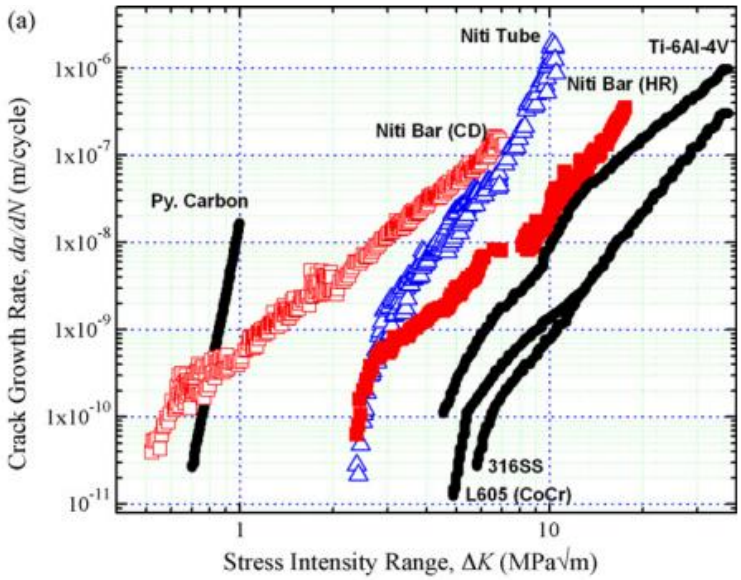

Fig. 29. Comparison of fatigue crack growth rate as a function of stress intensity factor ΔK of NiTi alloy subjected to different thermomechanical treatment (CD: cold-drawn, HR: hot-rolled) and other materials used for biomedical implants. [106]

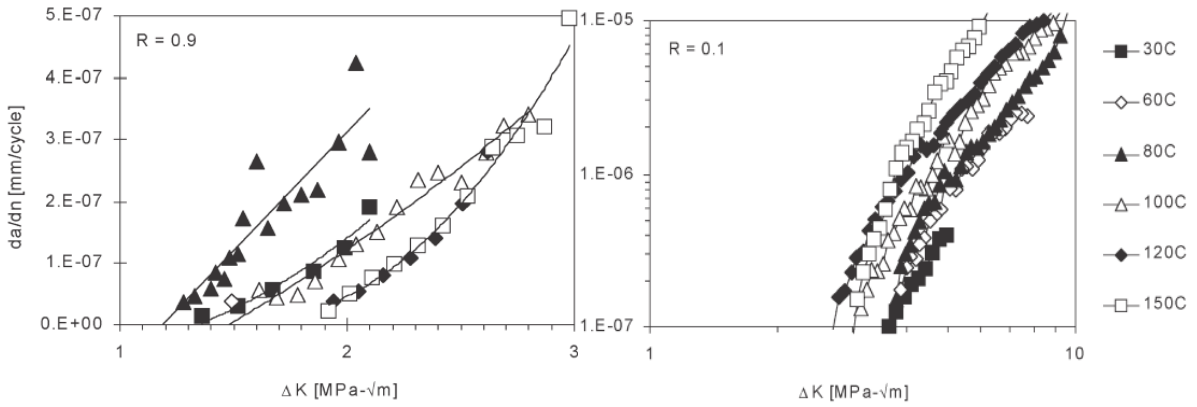

Fig. 30. The near-threshold crack growth rate in $Ni_{49.9}Ti_{50.1}$ heat-treated 750°C/1h at various temperatures for stress ratio R=0.9 and 0.1. [107]

The formation of the plastic zone at the crack tip of NiTi alloy also creates stress fields (compressive at the crack tip), which increases stress resp. K factor needed for crack tip opening (σ_{op} resp. K_{op}). If a small number of overloading cycles are added to a monotonous loading, the plastic zone at the crack tip and K_{op} is increased, which decreases crack growth rate. The effect of overloading cycles on NiTi alloy has been studied in [108][109]. As can be seen in Fig. 31, overloading cycles have a significantly positive impact on fatigue life in thermal cycling under constant uniaxial tension (wire actuation). Fatigue crack growth rate is decreased, even though transformation strain is at around the same level of 4 %. Contrastingly, the higher the overloading stresses are, the higher the permanent strain is accumulated during fatigue cycling (Fig. 32 a).

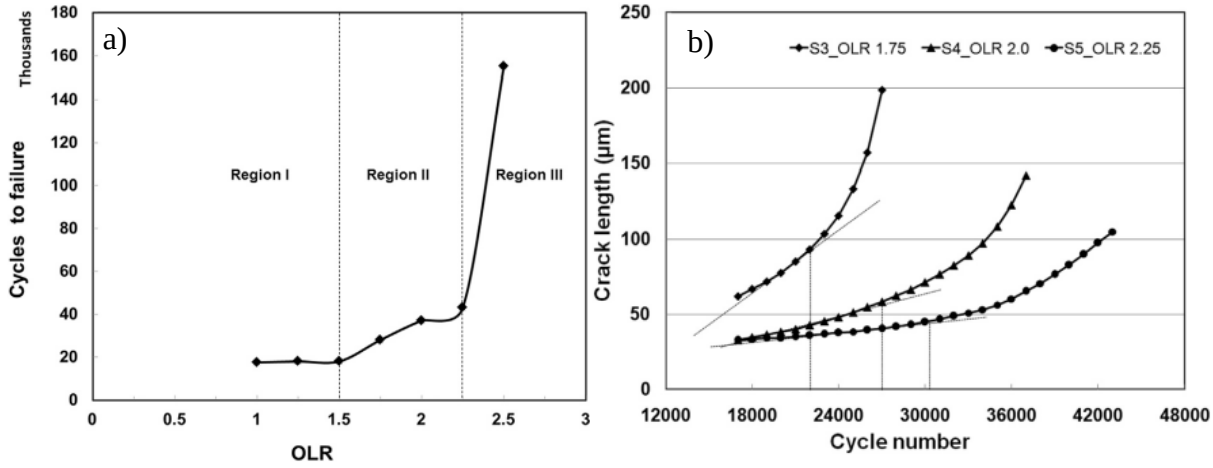

Fig. 31. a) Illustration of overloading cycle effect on fatigue life of actuator at constant stress 200 MPa (Overload ratio $OLR = \frac{\text{overload stress}}{\text{nominal stress}}$), b) Fatigue crack length vs. the number of actuation cycles for wires with varying OLRs. [108]

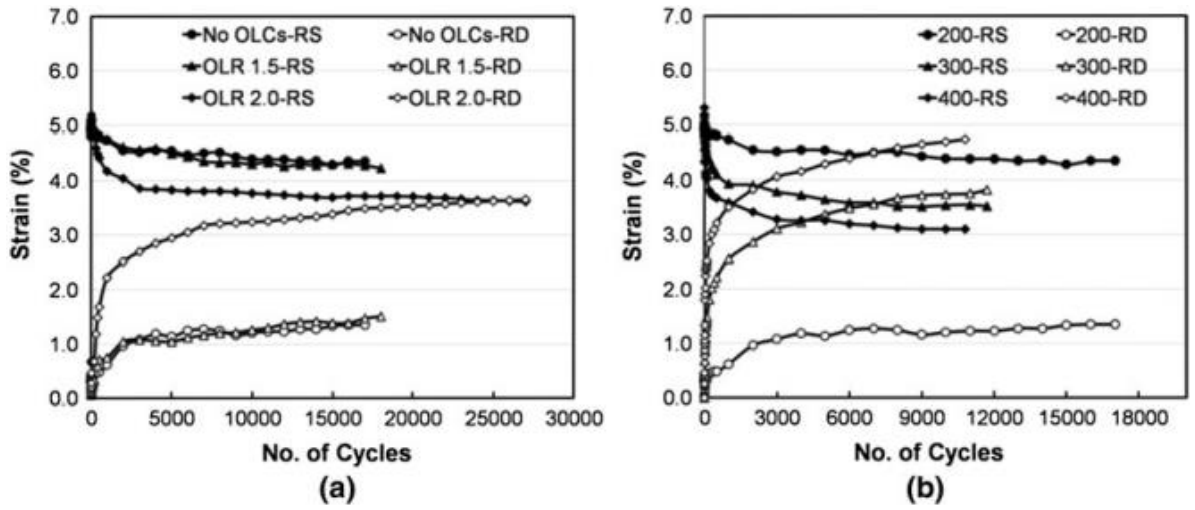

Fig. 32. a) Illustration of overloading cycle influence on fatigue life, transformation strain (RS) and permanent strain (RD), b) influence of actuation stress level. [109]

The heat treatment method called ''healing'' is also described in the NiTi literature. The sample is intentionally overheated highly above A_f temperature during thermomechanical cycling to remove residual martensite or even recover dislocations introduced by martensitic transformation. Consequences of previous cycling (functional degradation) can be to some extent removed by this treatment. However, this method is beneficial only in the case of low-cycle fatigue, where martensitic transformation occurs, before nucleation of a macroscopic crack [110]. On the contrary, if a macroscopic crack nucleates, stress relaxation at the crack tip increases fatigue crack growth rate. Repeated overheating in each actuation cycle also decreases fatigue life. For example, overstepping of A_f temperature by 40 °C instead of 10 °C results in three times lower fatigue life [109].

The grain size of the polycrystalline matrix significantly affects the material properties of NiTi alloy. The benefits of nanograin microstructure are increased tensile strength, yield stress, and suppressed dislocation activity, which decreases accumulated permanent strain in superelastic cycling [18][19][53]. However, the ductility of that microstructure is limited. Note that ductility of NiTi alloy varies significantly from approx. 4 % up to 60 % depending on heat treatment/grain size [19][74]. The result of a nanograin microstructure is substantially decreased plastic zone at the crack tip and an increase of stress concentration leading to a decrease in fracture toughness and an increase of crack growth rate [106][111]. Fracture toughness K_{IC} of $Ni_{50.9}Ti_{49.1}$ alloy was measured in [54], where cold working and heat treatment of CT samples yielded a grain size 10-1500 nm. The reported fracture toughness of samples was approx. 46 MPa*$m^{1/2}$ resp. 25 MPa*$m^{1/2}$ for grain size 1500 nm resp. 10 nm (Fig. 33).

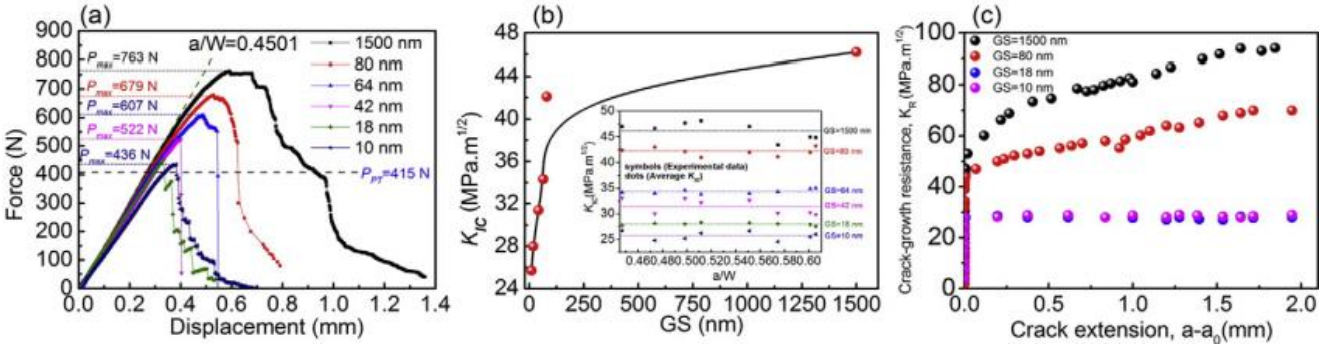

Fig. 33. Grain size effect on force-displacement curves and fracture toughness of CT specimens. [54]

Another important factor affecting fracture toughness of superelastic NiTi alloy is transformation stress. Mobility of the martensite band front is suppressed by grain boundaries of nanograin microstructure, high dislocation density, and even amorphous phase after severe cold-working. Therefore, transformation stresses are increased and the martensitic zone at the crack tip is reduced (see Fig. 34) leading to lower fracture toughness [71][112]. Mechanical properties of grain boundaries become more relevant in nanograin microstructure and act as a rigid shell with a superelastic core [71]. Thus, martensitic transformation is not localized into the martensite band front described in [26] for NiTi with grain size above 50 nm. Transformation occurs in individual grains independently at different macroscopic stresses (without transformation plateau). Another view of this issue is presented in [54]. Crooked propagation of fatigue crack (in mixed mode I and II) was observed in a coarse-grain NiTi. In contrast, direct propagation in mode I is observed in a nanograin microstructure (Fig. 34). Thus, fracture toughness and K_{th} are lower again in nanograin microstructures. On the other hand, it is explicit that the crack mainly propagates transgranularly and intragranularly by occasion (Fig. 35) in [113] and the effect of larger grains on the direction of crack propagation is not as pronounced as illustrated in [54].

In summary, the extent of the martensitic and plastic zone at the crack tip is significantly reduced in nanograin microstructure due to the combination of higher transformation stresses, suppressed transformation strain, and ductility of the material. On the contrary, annealing above 500 °C creates a microstructure with higher fracture toughness. However, stability of superelastic cycles is compromised in material with higher grain size and compromise must be found for an individual application of NiTi alloy.

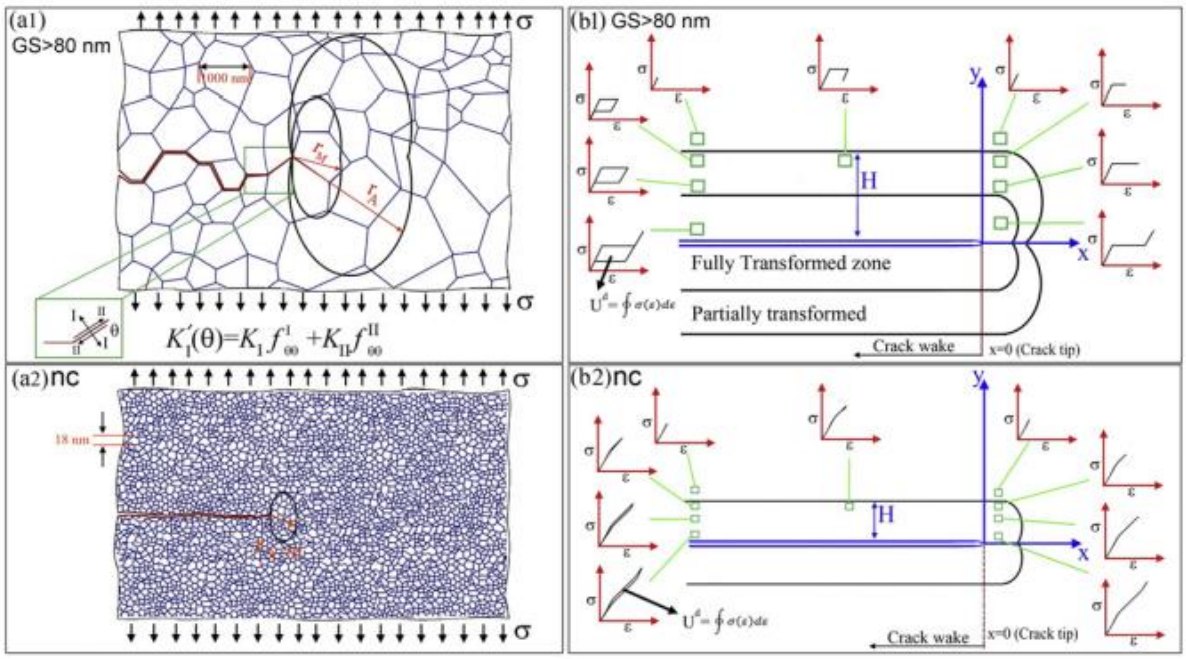

Fig. 34. Illustration of grain size effect on the crack propagation and deformation zones at the crack tip. [54]

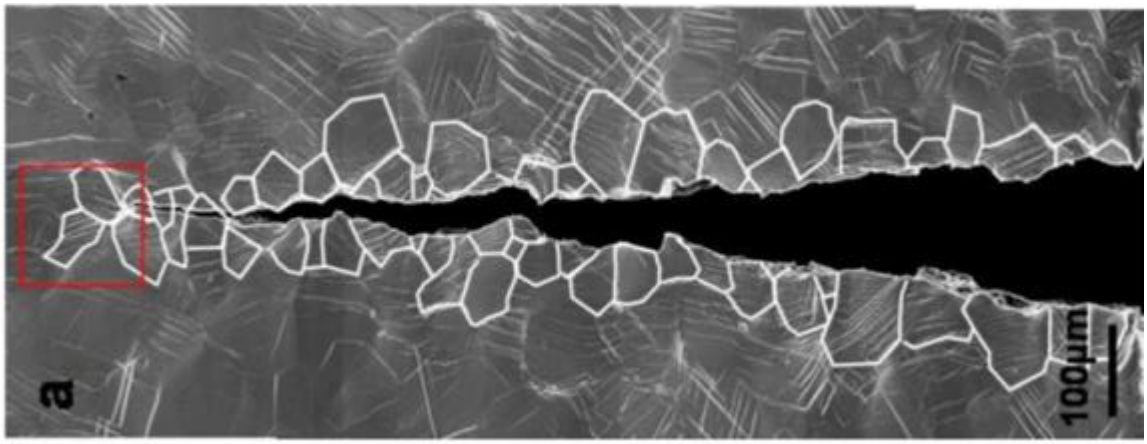

Fig. 35. SEM image of the crack morphology; the white lines highlight the grain boundaries. [113]

2 Experimental part/objectives of the dissertation

Functional properties of NiTi alloys can significantly differ depending on chemical composition and thermomechanical treatment (cold working, annealing, etc.) that affects the virgin austenitic microstructure (grain size, lattice defects, and Ni_4Ti_3 precipitates). In this dissertation, stress-strain-temperature curves of NiTi wires in tension are recorded in various thermomechanical loading regimes (superelasticity, actuation, shape memory effect) as a source of data for characterization of functional properties of NiTi wires. The main objective is to find a connection between functional fatigue, structural fatigue, virgin microstructure, and microstructure evolution during thermomechanical (especially superelastic) loading at various conditions (temperature and stress). The tested wires were pulse heat-treated by electric current as well as conventionally annealed in an environmental furnace to identify effects of microstructure recovery/recrystallization, as well as the effect of Ni-rich precipitates created by suitable annealing. Low cycle fatigue tests in the superelastic regime are used to characterize functional properties and structural fatigue of the NiTi wires. These tests were complemented by extensive TEM and SEM analysis of the virgin and thermomechanically loaded samples to evaluate changes in microstructure. An important assumption of this work is that the majority of the unrecovered strain and generation of lattice defects occur when martensitic transformation proceeds under applied stress and depends on the stress levels of forward and reverse transformations. In other words, levels of transformation stresses are more relevant for fatigue damage and permanent strain accumulation than stress or strain amplitudes. These claims are evidenced by a series of thermomechanical loading tests and TEM microscopy of the tested samples.

3 Experimental details

Cold-worked Ni-rich NiTi wire (50.8 at. % Ni, 45 ± 5 % CW, 0.1 mm in diameter, produced by Fort Wayne Metals in 2011) was used in the experiments. The NiTi wire was annealed by electric current pulse with the aim to obtain superelastic samples with desired nanograin microstructure. Constant power 160 W/mm^3 (62.5 W for 50 mm samples) of the electric pulse was applied for 10 ms, 13 ms, 15 ms, 16 ms, and 20 ms to produce samples with different virgin austenitic microstructures. The pulse time is used to denote the produced NiTi wires further on. Moreover, selected 13 ms, 15 ms, and 20 ms samples were further aged for 1 h at 400 °C to introduce precipitates of Ni_4Ti_3 phase. Such heat-treated wire is called 13 ms+400 °C/1h.

Thermomechanical testing and fatigue cycling were performed on the MITTER rig (Fig. 1) developed and constructed at the Department of Functional Materials at the Institute of Physics of the Czech Academy of Sciences for testing NiTi wires. The testing rig MITTER allows both mechanical testing and pulse heat treatment by electric current, which eliminates transmission of samples. Peltier elements are controlling the testing temperature in the range from -40 to 200 °C. More detailed information on the testing rig and pulse heat treatment by the electric current can be found in [18][72][73][74]. Tests below the lower temperature limit were carried out by means of an aluminum heat sink filled with liquid nitrogen placed on the top of the copper body of the Peltier chamber to reach nearly -100 °C. The ends of the wires were clamped into stainless steel capillaries (1.6 mm in the outer and 0.18 mm in the inner diameter) for easier manipulation and gripping in the MITTER tester. The gauge length of the wire sample between the capillaries was 50 mm. The sample with capillaries fits into the 80 mm long copper chamber

and can be kept at a homogenous temperature with a minimum temperature gradient from the wire center towards the capillaries.

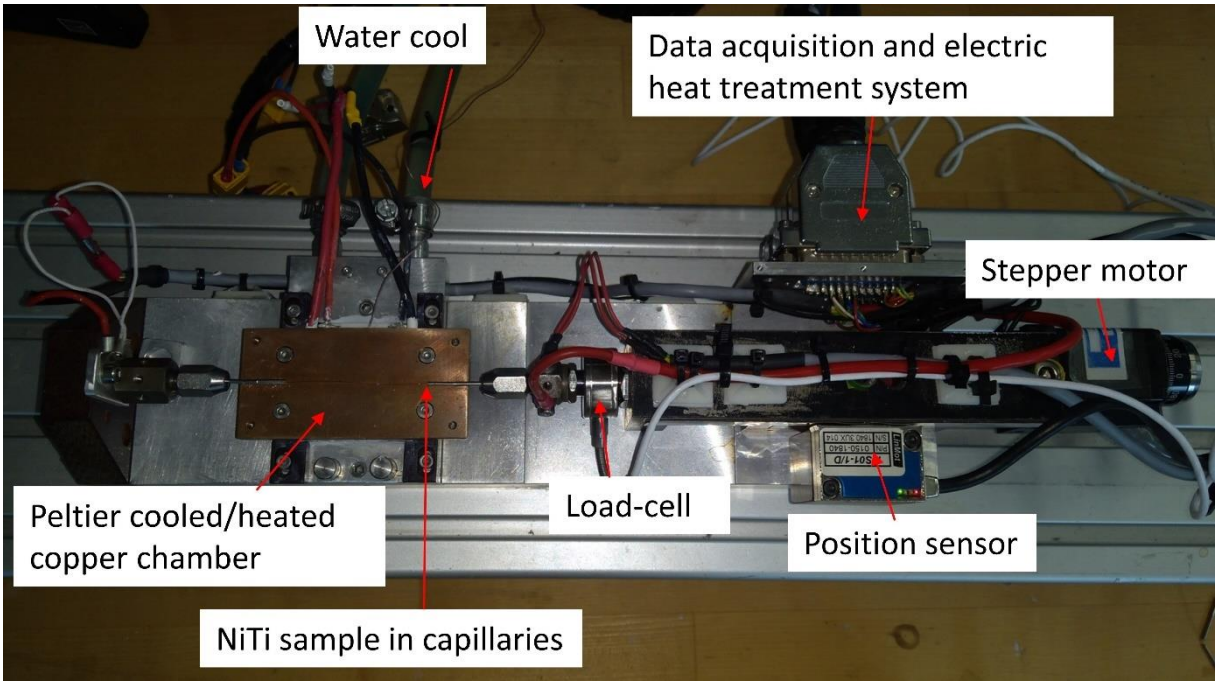

Fig. 1. Miniature tensile tester MITTER (equipped with a load cell, stepper motor, position encoder, Peltier-based environmental chamber, resistance measurement, and closed-loop LabView-based control system) used to perform both the electro-pulse heat treatment and thermomechanical loading tests of the NiTi wires.

The cooling/heating dilatometry experiments (Fig. 3a,b) were performed using thermal/mechanical analyzer LINSEIS TMA PT1600 under a force of 0.1 N (13 MPa tensile stress) using cooling and heating rate 3 °C/min. The DSC measurements were performed using DSC 25 apparatus by TA Instruments.

Tensile tests were performed at various temperatures in the range from -30 °C to 190 °C in a displacement-controlled regime to explore superelastic stress-strain response and deformation until fracture (Fig. 2). The displacement rate of the test was 0.05 mm/s (0.1 %/s strain rate). The following material characteristics were evaluated: upper plateau stress σ_p^{up}, upper plateau strain ε_p^{up}, and unrecovered strain ε_{us} in the first superelastic cycle, yield stress σ_y (the point above the upper plateau of the first loading cycle where the stress-strain curve deviates from the linear path by 0.2 % of strain), tensile strength R_m, and ductility A.

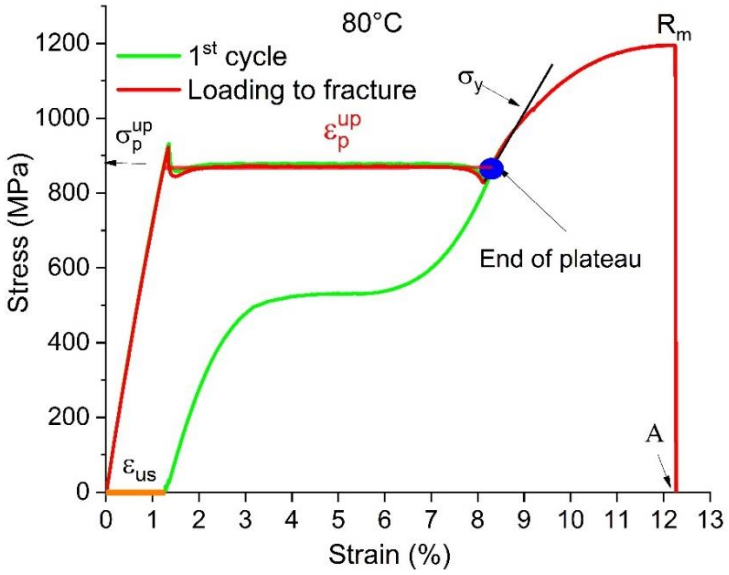

Fig. 2. Material characteristics of superelastic NiTi wire evaluated from the tensile test (upper plateau stress σ_p^{up}, upper plateau strain ε_p^{up}, unrecovered strain ε_{us}, yield stress σ_y, ductility A, and tensile strength R_m). NiTi wire was subjected to: 1) tensile deformation up to the end of stress plateau and unloading (green curve) and 2) tensile test up to fracture (red curve) at a constant temperature. Stress-strain curves recorded at temperature 80 °C and strain rate 0.1 %/s are shown only as an example on which the definition of material characteristics is demonstrated.

Superelastic fatigue tests were performed at a 1 %/s strain rate in the displacement-controlled regime. Since the higher strain rate used affects a stress-strain response [114] owing to the exothermic/endothermic character of the forward/reverse martensitic transformation, tensile cycles at a lower strain rate (0.1 %/s) were included during the fatigue tests to monitor the evolution of stress-strain response upon cycling. The lower loading limit was 10 MPa, which prevents buckling of NiTi wires as unrecovered strain accumulates in the fatigue cycling above A_f temperature. The upper loading limit was set to the end of the stress plateau at a given temperature. A temperature range in which the fatigue experiments were performed (roughly - 5 °C to 110 °C) depended on fatigue and material characteristics of a particular wire (A_f, $\varepsilon_{us} < 4$ % and $N_f > 1000$ cycles). Fatigue tests were repeated 5 times at each temperature to capture a scatter of fatigue life.

Samples for TEM observation of lattice defects in the virgin and deformed wires were prepared by the Focused Ion Beam (FIB) method using the FEI Quanta 3D FIB-SEM electron microscope. TEM lamellae were extracted in such a way that the wire loading axis always lies in the plane of the lamellae. TEM observations were carried out using the FEI Tecnai TF20 X-twin field emission gun microscope operated at 200 kV.

4 Results

4.1 Thermomechanical characterization of NiTi wires

4.1.1 Microstructure and transformation temperatures

As explained in chapter 1.3, the thermomechanical properties of NiTi wire depend on chemical composition (transformation temperatures) and microstructural state (grain size, lattice defects, precipitates). Both can be adjusted by the heat treatment to some extent. Hence, we need to characterize the virgin microstructure and transformation temperature of all NiTi wires used in thermomechanical loading experiments. Virgin microstructures of the tested wires before thermomechanical and fatigue experiments were analyzed by TEM (Fig. 3e, f, g, h). While the partially recrystallized microstructure of the 10 ms wire (d ~ 20 nm) contains a high density of lattice defects, microstructures of the 13 ms and 15 ms wires are completely recrystallized with mean grain size 75 nm and 250 nm, respectively.

Transformation temperatures of the wires were determined by DSC (Fig. 3a, b) and compared with dilatometry measurement under a constant tensile stress of 13 MPa (0.1 N) (Fig. 3c, d). The 10 ms wire does not show any significant response induced by B2-B19' martensitic transformation in the tested temperature range and only marginal R-phase transformation. The 13 ms wire shows R-phase transformation below 0 °C (with a similar broad and flat transformation peak as the 10 ms sample) and R-B19' transformation with transformation temperatures: M_s = -81 °C and A_f = -8 °C. The additional 400°C/1h aging results in the increase of both M_s = -77 °C and A_f = 44 °C temperatures and distinct R-phase transformation. On the other hand, cooling under stress, that produces oriented martensite, shows much higher M_s = -51 °C, which better represents the change in the stress-strain response (Fig. 4b). Since the A_f temperature increases more than the M_s, the aged sample exhibits wider temperature hysteresis. The 15 ms wire shows R-phase transformation as well and the R-B19' transformation displays temperature hysteresis with M_s = -70 °C and A_f = -5 °C. Contrastingly, the sample exhibits direct B19'-B2 transformation with A_f = -20 °C in the heating under stress, and M_s = -54 °C (see the dilatometry in Fig. 3c).

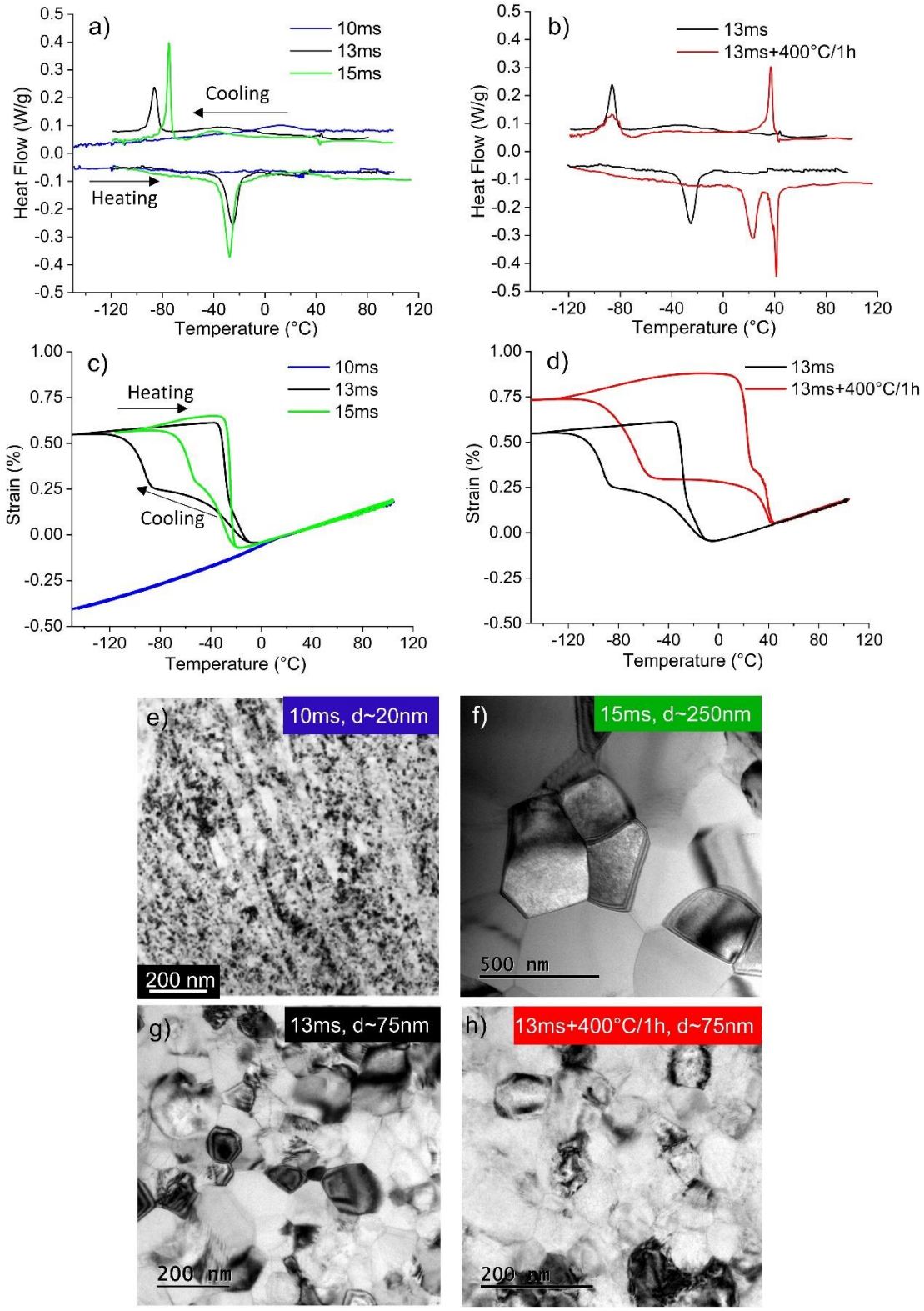

Fig. 3. Thermal responses (a, b, c, d) of NiTi wires having various microstructures (e, f, g, h). Standard DSC record is shown in a) and b). The strain-temperature curves (c, d) were recorded upon cooling/heating under 13MPa constant stress (0.1N force). TEM micrographs (e, f, g, h) show microstructure of the NiTi wires heat-treated for e) 10 ms, f) 15 ms and g) 13 ms (at a constant power density of 160 W/mm^3) and h) 13ms+400°C/1h.

4.1.2 Mechanical properties of NiTi wires determined from tensile tests

Stress-strain responses of the wires at 20 °C with different microstructures are shown in Fig. 4a,b. The cold-worked wire shows no transformation plateau strain, ductility of 6 %, and the highest tensile strength ~ 1900 MPa. The 10 ms wire (d ~ 20 nm), which did not show any transformation in the thermal cycle, exhibits superelasticity at room temperature, with 5.2 % transformation strain ε_p^{up} at nearly constant upper plateau stress σ_p^{up} of 560 MPa, 13 % ductility, and only slightly lower tensile strength ~ 1700 MPa. The 13 ms wire (d ~ 75 nm) exhibits perfect superelasticity with a larger upper plateau ε_p^{up} of 6.7 % and upper plateau stress σ_p^{up} of 475 MPa. Ductility remains around 13 %, however, tensile strength decreases significantly (R_m ~ 1300 MPa). Finally, the 15 ms wire (d ~ 250 nm) displays the largest ε_p^{up} of 7.3 %, upper plateau stress σ_p^{up} of 420 MPa, further reduced R_m ~ 1030 MPa, and a very large ductility of 56 %. The first superelastic stress-strain cycles at 20 °C are perfectly recoverable in the case of all wires (the aged sample has to be heated above 44 °C to induce reverse transformation).

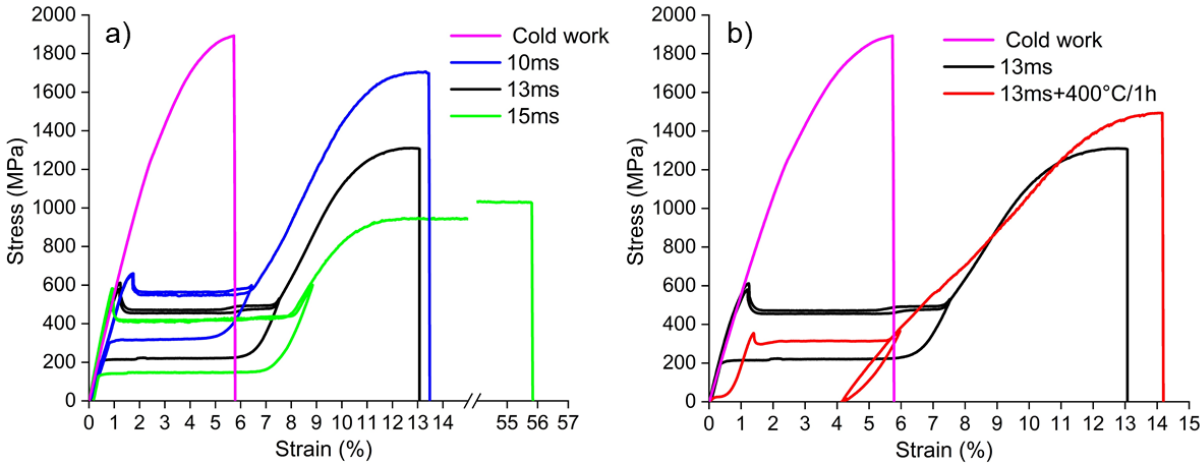

Fig. 4. Mechanical responses of NiTi wires showing the effect of a) recrystallization and b) aging. The stress-strain curves were recorded in uniaxial tensile tests (one superelastic cycle followed by deformation until fracture) at 20 °C.

The additional aging treatment (400°C/1h) applied to the 13 ms wire does not increase the grain size (d ~ 75 nm) (Fig. 3f), but changes the transformation temperatures (Fig. 3b), which causes the decrease of upper plateau stress σ_p^{up} by approx. 170 MPa (Fig. 4d) and increases the R_m to approx. 1500 MPa. Furthermore, the upper plateau strain ε_p^{up} is reduced to 5 %. The ~ 30°C difference in M_s temperature of samples with and without the additional aging (Fig. 3b) corresponds quite well to the decrease in upper plateau stress (Fig. 4b) (considering the stress rate $\frac{d\sigma}{dT}$ = 6 MPa/°C (Fig. 7a)). The detailed STEM analysis of the aged 13 ms wire is shown in Fig. 21.

In order to determine the superelastic functional behavior of NiTi wires subjected to various heat treatments and establish temperature ranges for fatigue experiments, tensile tests were carried out in the temperature range 20 °C to 190 °C. A comparison of the tested microstructures at the same temperature point is shown in Fig. 5 and a comparison of one microstructure at various temperature points is in Fig. 6. After deformation up to the end of stress plateau and unloading, the wires were stress-free heated up by 100 °C above the test

temperature to relieve residual martensite and determine the unrecovered strain introduced during the first superelastic cycle. Temperature dependence of upper plateau stress σ_p^{up} (Fig. 7a) and unrecovered strains ε_{us} (Fig. 7b) were plotted as a function of temperature. The superelastic stress-strain curves shift to higher stresses with increasing test temperature, showing the characteristic temperature dependence of transformation stress of ~ 6 MPa/°C (Fig. 7a), as is common for superelastic NiTi alloys. This does not necessarily mean that the stress-induced B2-(R)-B19' martensitic transformation is the only deformation mechanism activated within the martensite band front propagating at plateau stress, particularly in tensile tests at elevated temperatures [86]. Deformation twinning in the martensite phase and dislocation slip accompanies the stress-induced martensitic transformation in tensile tests at elevated temperatures (see [41][86][95] for detailed discussion).

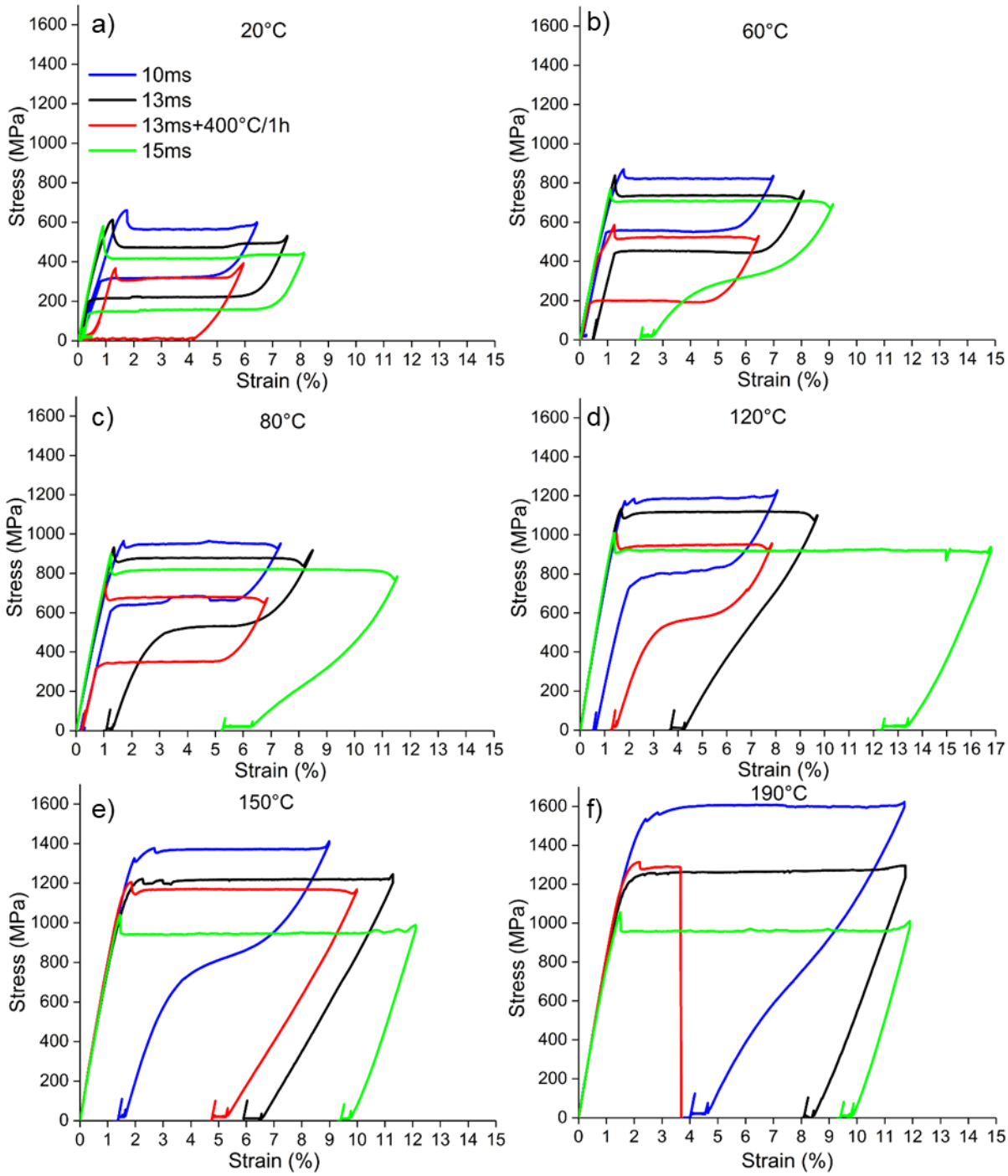

Fig. 5. Stress-strain superelastic response of the NiTi wires at a) 20 °C, b) 60 °C, c) 80 °C, d) 120 °C, e) 150 °C and f) 190 °C. One loading/unloading cycle to the end of the upper plateau followed by heating by 100 °C to recover residual martensite to examine mechanical properties (σ_p^{up}) and stability (ε_{us}) of superelastic loops.

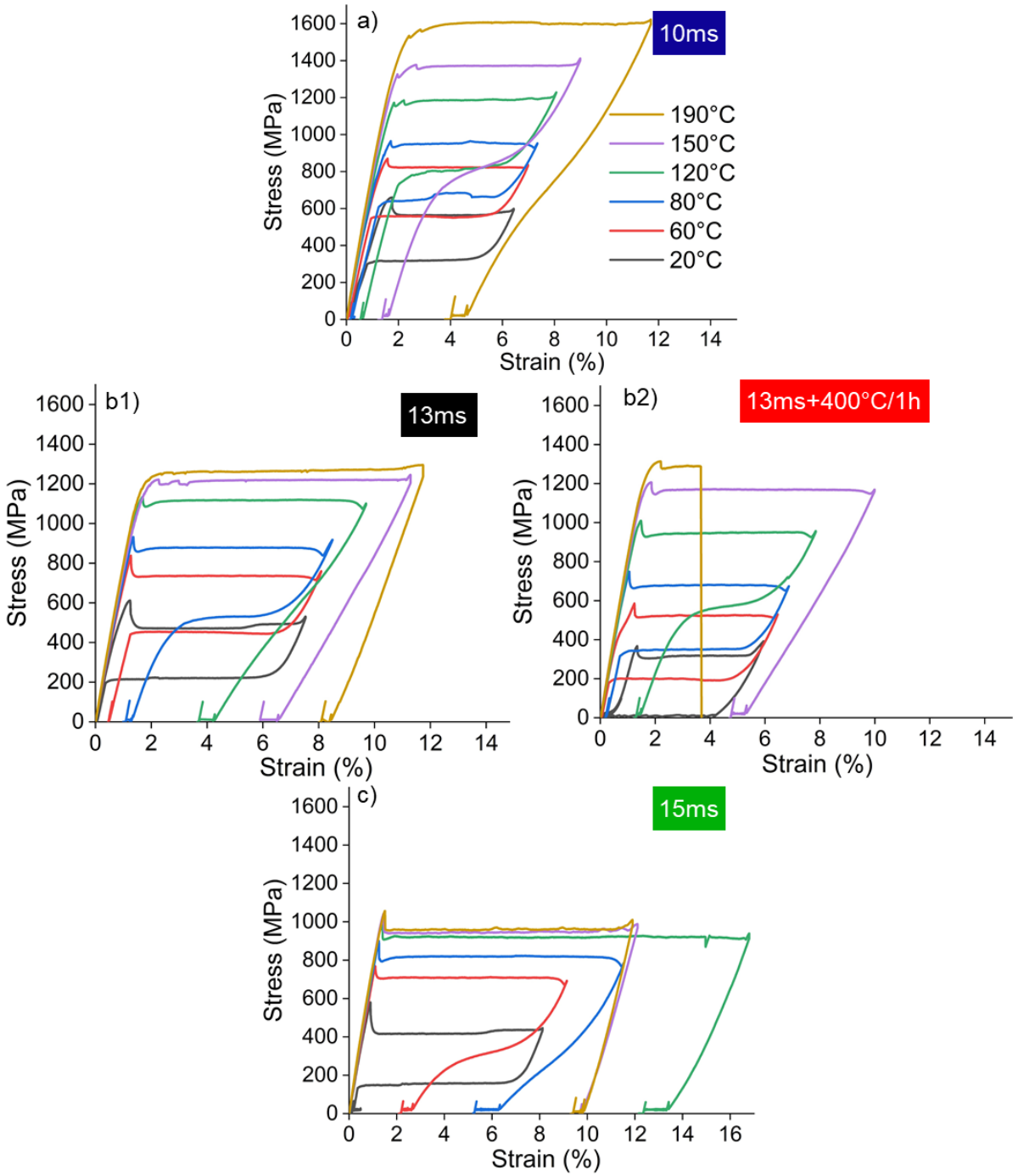

Fig. 6 Stress-strain curves recorded in tensile loading/unloading tests up to the end of stress plateau on four different NiTi wires at various test temperatures in the range of 20 °C to 190 °C. a) 10 ms, b1) 13 ms, b2) 13 ms+400°C/1h and c) 15ms NiTi samples. The wires were heated up by 100 °C to recover residual martensite.

Although all tested microstructures are stable at 20 °C and less than 0.1 % unrecovered strain ε_u is measured in one superelastic cycle (shape memory cycle for the aged sample), there are large differences in upper plateau stress, unrecovered strains, and cyclic instability in tensile tests at elevated temperatures (compare the stress-strain curves of 10 ms and 15 ms wires in Fig. 6a,c). The 10 ms wire shows the lowest unrecovered strain and highest upper plateau stresses in the whole temperature range. Moreover, the linear temperature dependence of upper plateau stress σ_p^{up}-T of the 10 ms wire in the whole temperature range (Fig. 7a) suggests that

the additional plastic deformation processes have a significantly smaller impact on the stress-strain response compared to the other samples (Figs. 6a, 7b). The temperature dependence of upper plateau stress σ_p^{up}-T of the 13 ms and 15 ms wires deviates from linear behavior above 110 °C and 80 °C, respectively, which points out the massive activity of plastic deformation processes in these tests [86]. The lower stress plateau on the stress-strain curve of the 10 ms, 13 ms, and 15 ms wire vanishes at 140 °C, 100 °C, and 60 °C, respectively. The aged sample (13 ms+400°C/1h) exhibits lower σ_p^{up} by approx. 170 MPa, smaller unrecovered strain, and higher yield stress σ_y compared to the 13 ms sample. Thus, the aged microstructure shows better functional stability at higher temperatures (see Fig. 7a,b). However, the 13 ms+400°C/1h wire is not capable to reach the end of its stress plateau at 190 °C and the sample breaks unpredictably within the plateau region, unlike the 13 ms sample. The slope of the temperature dependence of transformation stress $\frac{d\sigma}{dT}$ is not significantly affected by the precipitation or recrystallization processes in the linear part of the σ_p^{up}-T diagram (varies from 5.9 MPa/°C of the 10 ms wire to 6.3 MPa/°C of the 15 ms wire). The σ_p^{up}-T curves are only shifted in the stress/temperature space (Fig. 7a).

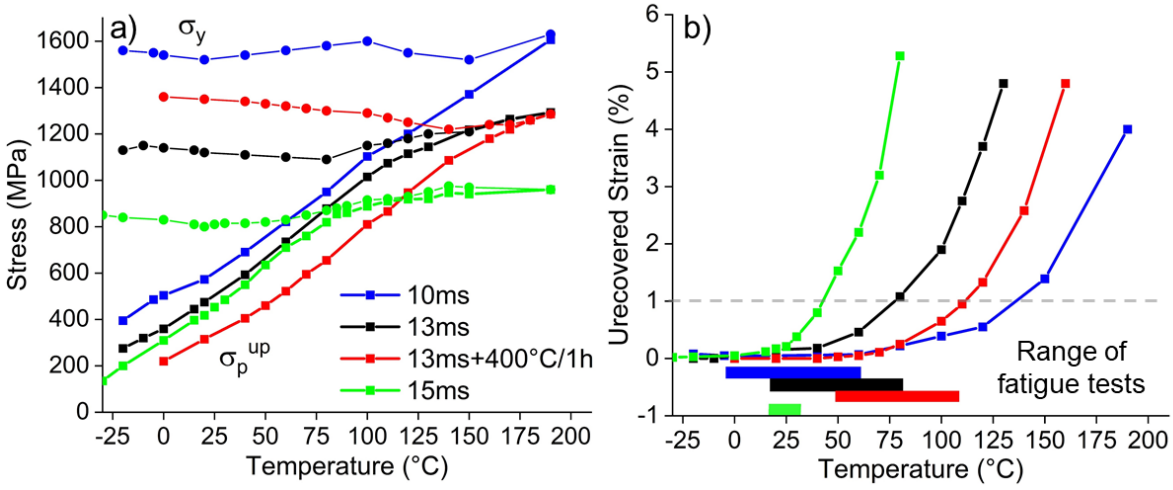

Fig. 7. Effect of temperature on superelastic properties of the NiTi wires- a) temperature dependence of upper plateau stress σ_p^{up} (showing Clausius-Clapeyron relation) and yield stress σ_y and b) unrecovered strain ε_{us} in the temperature range -30 °C to 190 °C (data points are obtained from superelastic and tensile tests shown in Figs. 4-6).

4.1.3 Analysis of unrecovered strain in thermomechanical loading cycles

An important assumption of this work is that plastic deformation accompanies martensitic transformation only when it proceeds under external stress, and that it depends on the stress levels of both forward and reverse transformations. In other words, levels of transformation stresses are more relevant for fatigue damage and accumulation of unrecovered strain than stress or strain amplitudes. Moreover, the functional degradation of stress-strain-temperature response is the display of dislocation activity and deformation twinning. These claims are substantiated by a series of thermomechanical loading tests of the 13 ms and 15 ms and 16 ms wires with grain size ranging from ~ 75 nm to 600 nm in the following sections.

15 ms microstructure

Cyclic superelastic and thermal loading tests

A series of cyclic superelastic tests at constant temperature (Fig. 8) and thermal cycling at constant stress (Fig. 9) were performed to evaluate unrecovered strain and permanent lattice defects generated by martensitic transformation proceeding under very different stress–temperature conditions. Since the superelastic strains in the tensile test at -30 °C are not recovered upon unloading (Fig. 8a), the closed-loop thermomechanical loading cycle was completed by heating under 20 MPa stress. The superelastic test at 20 °C and actuator test at 280 MPa (averaged stress of forward and reverse plateau of the superelastic test at 20 °C) are basic tests used to investigate functional thermomechanical properties of NiTi wires. The results of these tests are compared with the results of tests performed under extreme/unconventional conditions, for which the martensitic transformation proceeds at either very low or high stresses and temperatures.

A superelastic tensile test at room temperature (Fig. 8b) generates a medium unrecovered strain of 1.65 % and a significant amount of slip dislocations (Fig. 8b2). The reader is referred to our related paper [35], in which these slip dislocations were analyzed as belonging to the {011}/<100> austenite slip system. Deformation bands containing residual B19' martensite or {114} austenite twins can rarely occur. The stress–strain response in the test was unstable, and the hysteresis width decreased due to the gradual decrease of the upper plateau stress in 10 cycles. This contrasts with the test performed at -30 °C (Fig. 8a), in which only negligible unrecovered strain and few scattered dislocation segments (Fig. 8a2) were observed in the microstructure of the cycled wire and very good cyclic stability of the stress–strain–temperature response of the wire was observed. In this test, the forward martensitic transformation proceeds from the R-phase into the B19‘ martensite at low stress ~ 100 MPa, while the reverse transformation takes place upon heating under 20 MPa. Although the maximum stresses, strains, and temperature applied in the tests at -30 °C and 20 °C were comparable, the forward and reverse martensitic transformations proceeded at much higher stress in the latter. In the superelastic test at 80 °C, the recorded cyclic stress–strain response of the wire was extremely unstable (Fig. 8c). Unrecovered strain reached 6.45 % and the stress–strain curve became almost linear with small hysteresis after 10 loading cycles. The microstructure of the cycled wire is dominated by deformation bands (Fig. 8c1,c2). Detailed analysis of deformation bands created by tensile cycling of the 16 ms NiTi wire deformed superelastically at elevated temperatures have shown that the bands contain either residual B19' martensite or {114} austenite twins [41].

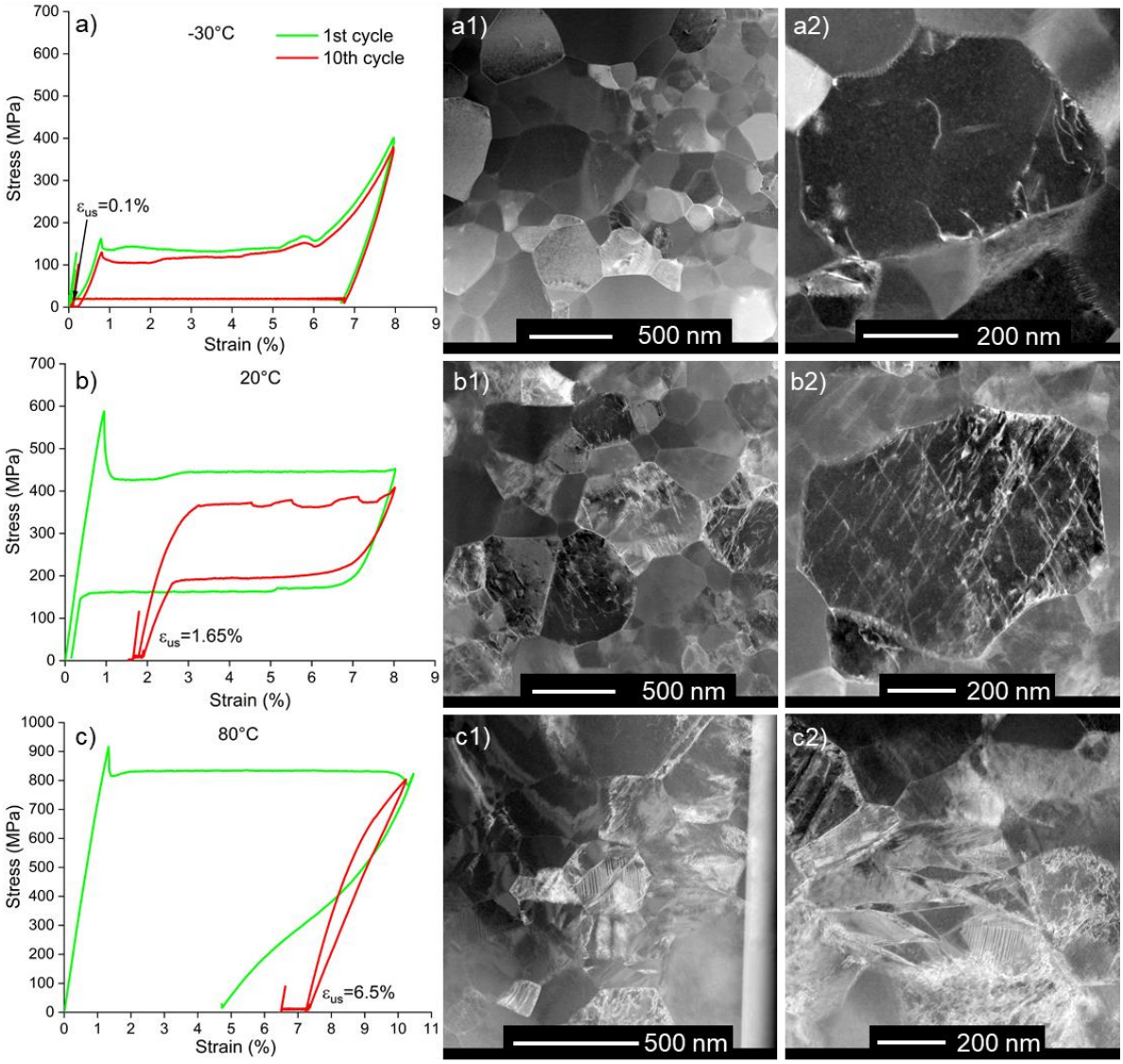

Fig. 8. Cyclic tensile tests at the temperature of a) -30 °C, b) 20 °C and c) 80 °C. Stress-strain curves recorded in the 1st and 10th cycle and resulting lattice defects observed by TEM in the microstructure of cycled wires (10 closed-loop cycles followed by heating to 150 °C to recover residual martensite).

In the thermal cycling under constant stress 280 MPa (Fig. 9b), a slightly larger unrecovered strain of 1.9 % was observed compared to the superelastic test at 20 °C. A significant amount of slip dislocations but no deformation bands were observed in the microstructure after 10 cycles (Fig. 9b1,b2). The strain–temperature response was unstable and the hysteresis width decreased significantly upon cycling, similarly as in the superelastic test at room temperature. This contrasts with the very stable strain–temperature response of the wire thermally cycled at 6.5 MPa (50 mN force) (Fig. 9a). Practically no unrecovered strain was recorded, and no lattice defects were found in the wire microstructure after 10 cycles (Fig. 9a1,a2). This result, although it seems to be trivial, is very important. There are reports in the literature showing various kinds of dislocation defects created upon stress-free thermal cycling of NiTi across a range of transformation temperatures M_f-A_f [115][116], which gives an impression that cyclic martensitic transformation proceeding even without external stress generates dislocation defects in the austenite lattice. Although this might be true as concerns point defects or faults [116] (difficult to resolve by conventional TEM), our results clearly prove that no slip

dislocations, twins, or other lattice defects easily observable by TEM were created during the first 10 thermal cycles at low stress 6.5 MPa. The most likely explanation of this contradiction is that the literature studies were typically performed on solution-treated NiTi alloys, while our experiments were performed on superelastic NiTi wire possessing nanograin microstructure. Upon thermal cycling at 750 MPa (Fig. 9c), strain-temperature response was very unstable of the ratcheting character, accumulated unrecovered strain of 20.1 % reached far into the plastic deformation range (Fig. 4), and a very high amount of deformation bands and slip dislocations were found in the microstructure of the wire. It shall be pointed out that while the reverse martensitic transformation proceeded upon heating under stress (Fig. 9c), the wire almost did not shorten. We have investigated and analyzed these ratcheting stress–strain–temperature responses upon thermal cycling of NiTi wire under large stress in [38][39]. The reader is referred to these articles for detailed explanation and interpretation of the ratcheting phenomenon.

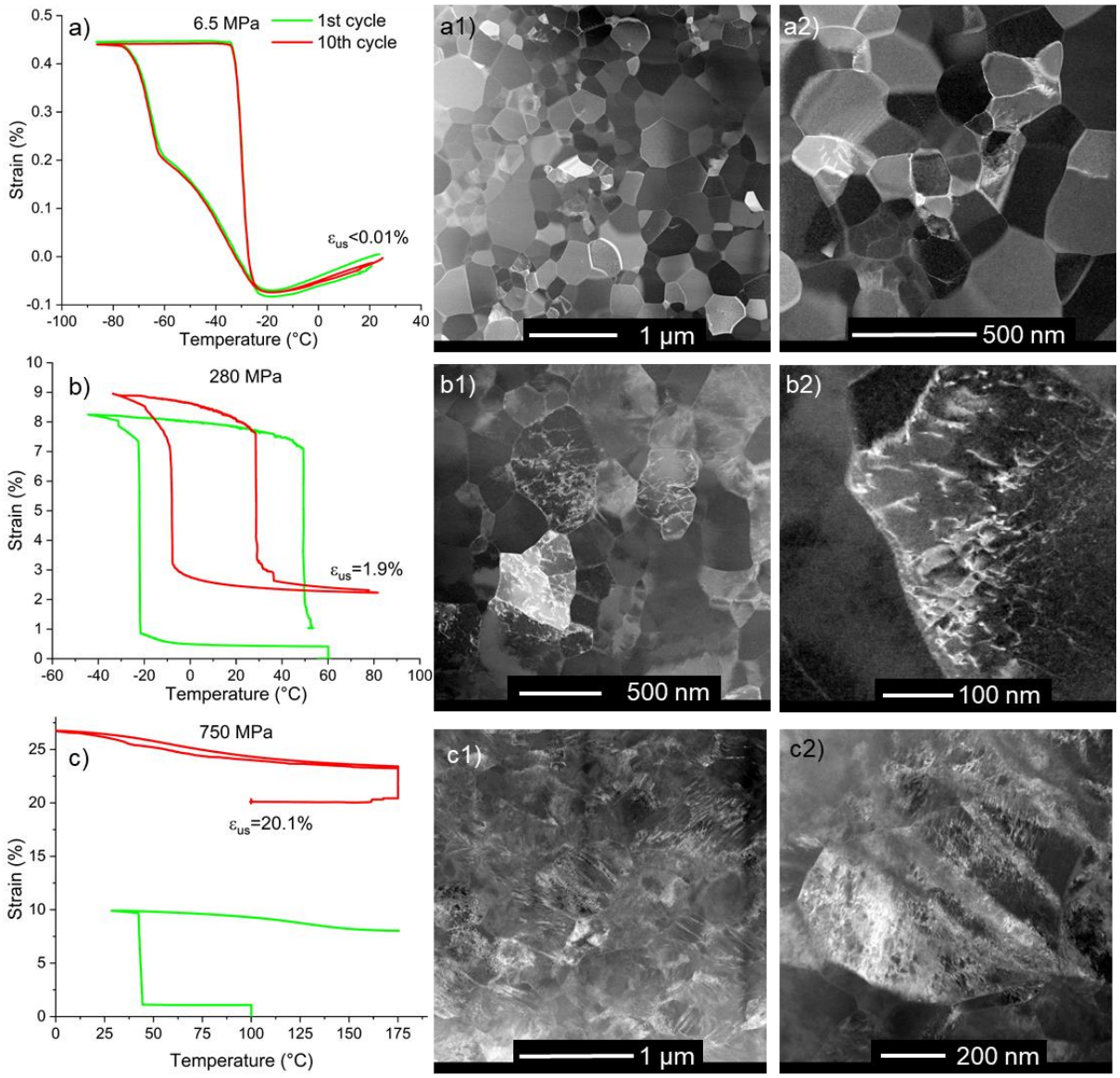

Figure 9. Thermal cycling at constant stress of a) 6.5 MPa, b) 280 MPa and c) 750 MPa. Strain-temperature curves recorded in the 1st and 10th cycle and resulting lattice defects observed by TEM in the microstructure of the cycled wires.

Cyclic Shape Memory and Recovery Stress Tests

Results of experiments reported in the previous section suggest that the stress and temperature, at which the martensitic transformation proceeds, play a key role in the mechanism generating the unrecovered strain and permanent lattice defects. This in turn implies that the stresses and temperature applied to the wire when it does not transform are less important. In order to prove that beyond any doubts, we have performed two thermomechanical loading experiments involving high stresses and temperatures, but the martensitic transformation in them never proceeded at high stresses and temperatures throughout the whole volume of the NiTi wire. The first experiment is the cyclic shape memory test (Fig. 10). The wire was loaded at -75 °C up to 400 MPa (8% strain), unloaded, and subsequently heated under 20 MPa stress up to 20 °C. The large strain induced in the martensite state recovered almost completely during the reverse transformation during heating in each cycle. The wire displayed stable stress–strain–temperature response, a small unrecovered strain of only 0.12 %, and a negligible amount of permanent lattice defects (mainly dislocation segments and loops) was generated in the 10 shape memory cycles (Fig. 10c-e). It has been empirically known that, in order to use NiTi elements in shape memory cycles multiple times, they have to be deformed below the M_s temperature in the low-temperature martensite state. It has been implicitly assumed that the element accumulates more damage when it is deformed above Ms because of the higher stress, though reliable experimental evidence is lacking. To the extent of the author's knowledge, experimental data on the stability of the cyclic shape memory effect are not available in the literature. Results published in the literature (e.g. [117]) were typically obtained on soft NiTi alloys and were limited to a few tens or hundreds of cycles.

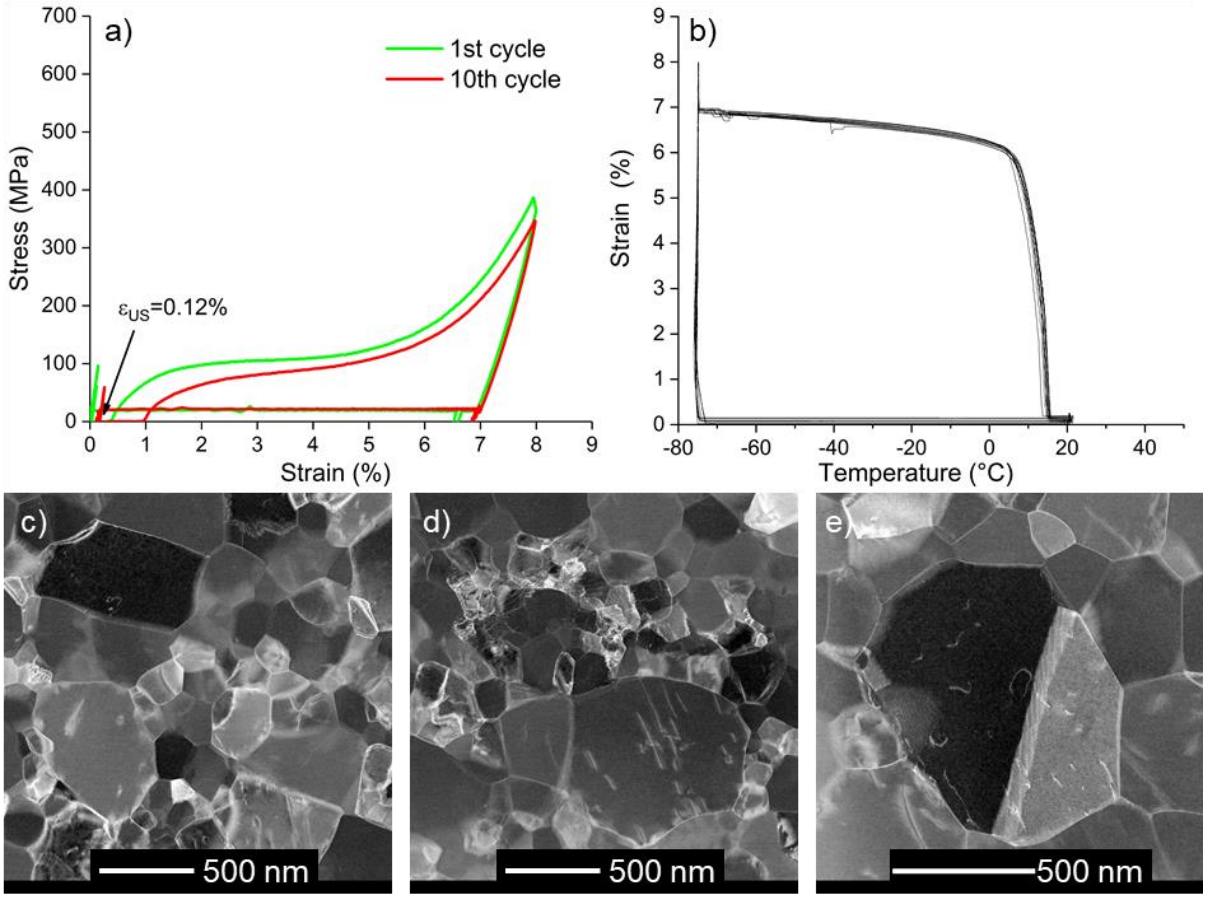

Fig. 10. Stress–strain (a), and strain-temperature (b) curves recorded in the first 10 cycles of Shape memory cycling and resulting lattice defects observed by TEM in the microstructure (c,d,e) .

The second experiment is the cyclic recovery stress test (Fig. 11). The wire was loaded at –75 °C up to 400 MPa (8% strain), unloaded to 100 MPa (7% strain), and subsequently thermally cycled under constant strain between 100 MPa and 500 MPa. Note that, although the stresses, strains, and temperature involved are rather large, the martensitic transformation does not massively occur upon thermal cycling (variation of phase fraction is negligible [118]). The stress-temperature response upon thermal cycling is stable, unrecovered strain is small (0.44 %), and only a low density of dislocation defects (no deformation bands) was observed in the microstructure of the wire after 10 thermal cycles (Fig. 11c-e).

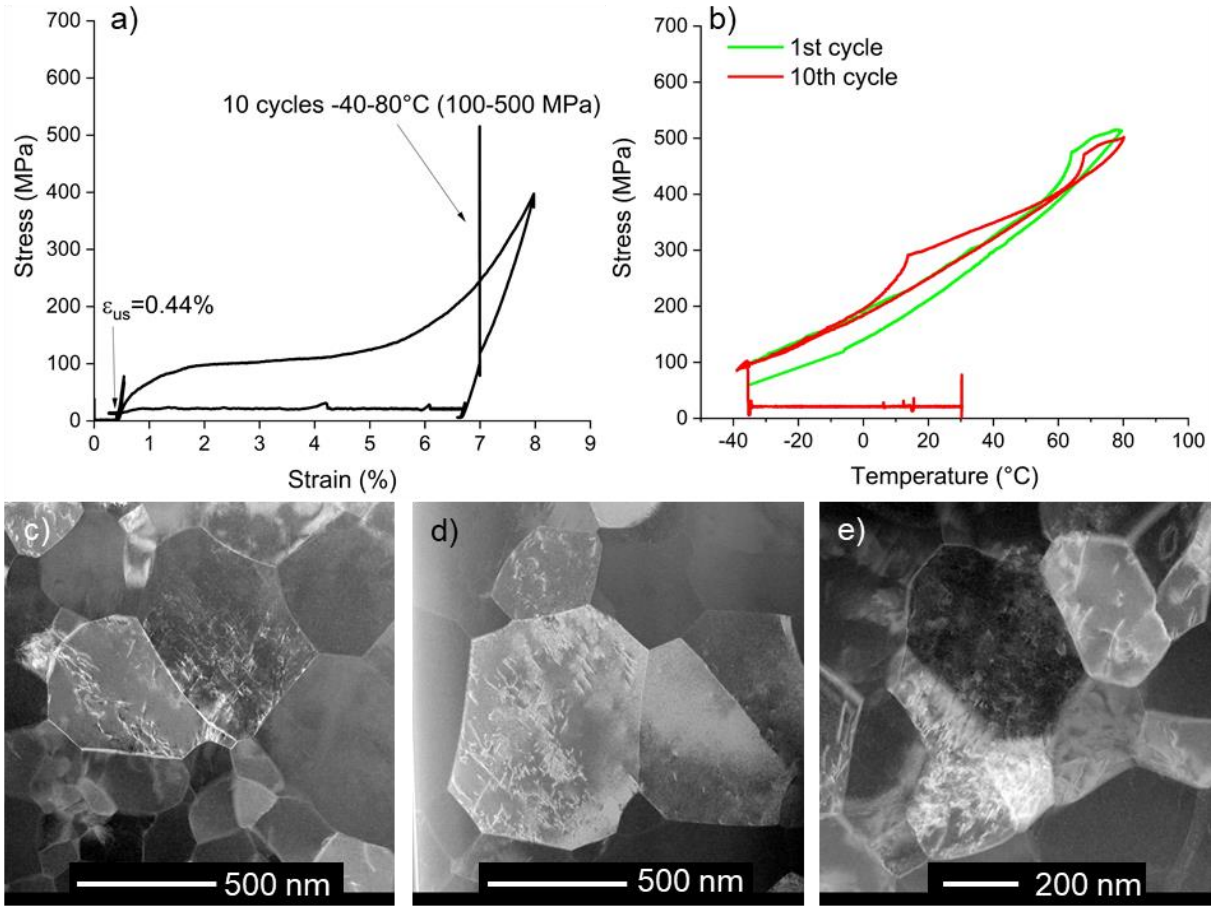

Fig. 11 Recovery stress cycling. Stress-strain (a), and stress-temperature (b) curves recorded in the first 10 cycles and resulting lattice defects observed by TEM in the microstructure (c,d,e).

Cyclic Bypass Tests Separating the Effects of Forward and Reverse Transformations

We knew from the results of [34] that the unrecovered strains generated by the forward and reverse martensitic transformation are generally different. Obviously, this cannot be analyzed based on the results of the previous superelastic and actuation tests (Figs. 8 and 9). This section presents results of thermomechanical loading experiments (Figs. 12 and 13) designed to evaluate the unrecovered strains and permanent lattice defects created upon cycling during the forward and reverse transformations, separately.

The conventional cyclic superelastic test (Figs. 12a) was performed at 30 °C (slightly higher compared to the test at 20 °C (Fig. 8b)) since we wanted a higher density of lattice defects to be generated upon cycling. The recorded accumulated unrecovered strain (2.5 %) is larger compared to 1.65% unrecovered strain in the test at 20 °C (Fig. 8b) and there appear deformation bands in the microstructure of the wire cycled at 30 °C, which correlates with a loss of transformation plateau in the 10th superelastic cycle. To find unrecovered strain generated during the forward loading and the reverse unloading branches of the superelastic curve, bypass thermomechanical loading tests were performed (Fig. 12b,c).

The forward martensitic transformation upon loading at 30 °C proceeded exactly in the same manner as in Fig. 12a, but then, instead of unloading, the wire was cooled (constrained at the

end of transformation plateau) down to -30 °C, unloaded, and heated under 20 MPa stress back to the 30 °C temperature (Fig. 12b). Such a closed-loop thermomechanical loading cycle was run 10 times. An unrecovered strain of ~ 2 % was recorded after 10 thermomechanical loading cycles. When the thermomechanical loading test was performed along with the same stress–temperature route but in the reverse order (cooling to martensite → loading to 8% strain → heating back to 30 °C → unloading to perform reverse transformation under stress), a slightly lower unrecovered strain of ~1,5 % was determined in the test (Fig. 12c). Based on the results of tests in Figs. 10 and 11, the majority of the recorded unrecovered strains and permanent lattice defects were assumed to be generated when the martensitic transformation proceeded under large stress upon the forward loading (reverse unloading), respectively.

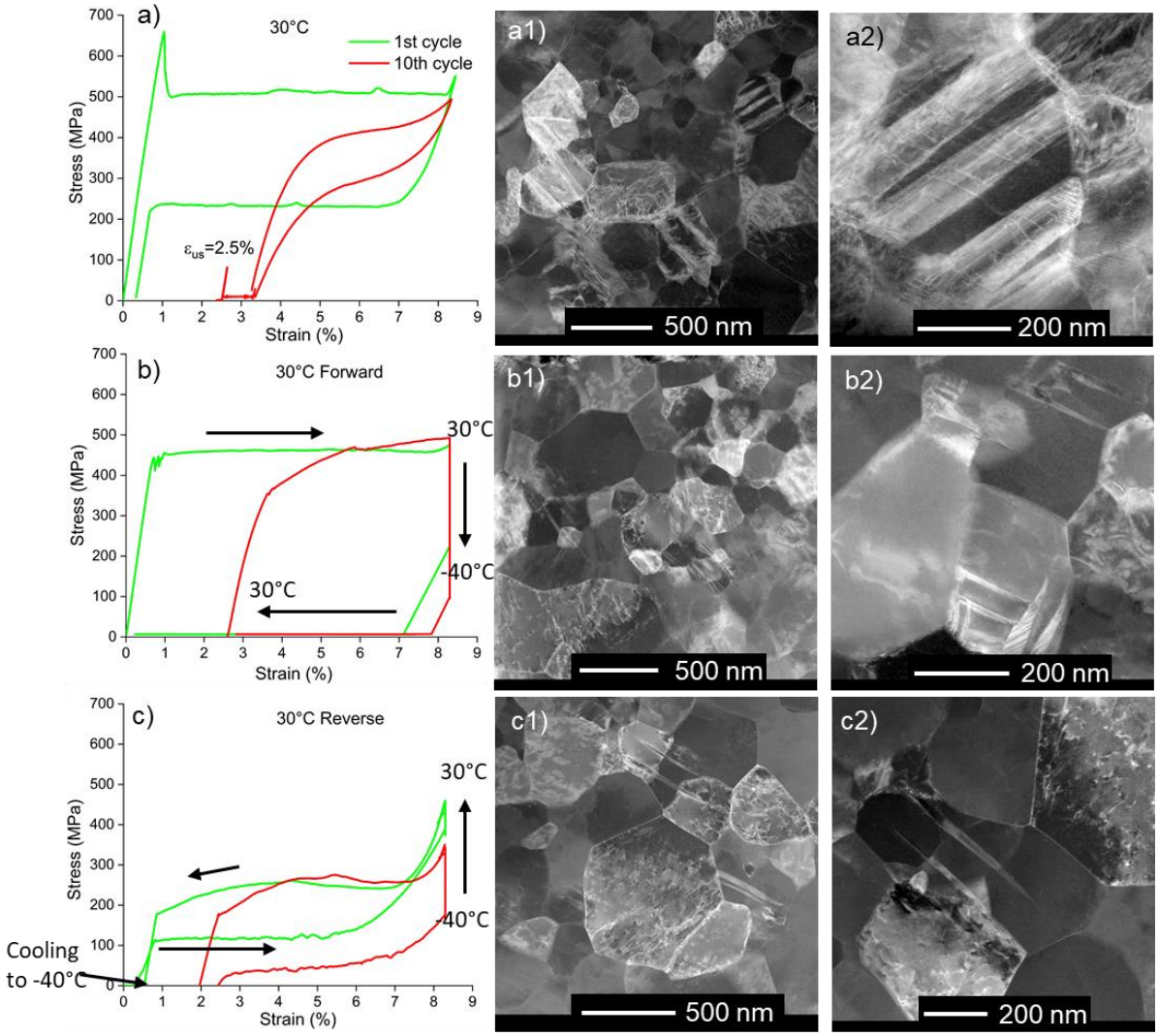

Fig. 12 Thermomechanical loading tests performed to evaluate unrecovered strains and lattice defects generated separately by the forward (b) and reverse (c) martensitic transformation in superelastic test (a). Stress-strain curves recorded in the 1st and 10th cycle in thermomechanical loading tests and lattice defects observed in the microstructure of the cycled wires. Compared to (a), there is no sharp transformation stress peak in (b), since the test was performed in dilatometer on short wire sample, in which the transformation front was nucleated within the grips.

The analysis of microstructures in wires subjected to these bypass tests showed that there are fewer slip dislocations and fewer deformation bands in both microstructures, compared to the

superelastically cycled wire (Fig. 12a1,a2). Although both microstructures look quite similar, long slip dislocations appear preferentially in the forward microstructure (Fig. 12b1,b2). Also, note that approx. 0.8% strain was recovered after 10 cycles at 30 °C during subsequent heating to 150 °C, which clears out most of the residual martensite, and only permanent defects in microstructure are observed by TEM. Residual martensite accounted for ~ 0.5% strain in the bypass tests.

Fig. 13a shows the conventional cyclic thermal test under 400MPa stress. In comparison to the similar test performed under smaller stress of 280 MPa (Fig. 9b), the accumulated unrecovered strain is significantly larger (3.7 % vs. 1.9 %), and there are more deformation bands in the microstructure of the cycled wire (Fig. 13a1,a2). The hysteresis width gets narrower to a similar extent as in the test presented in Fig. 9b but, in a contrast, the decrease of the hysteresis width is mainly due to the shift of the reverse transformation to lower temperatures.

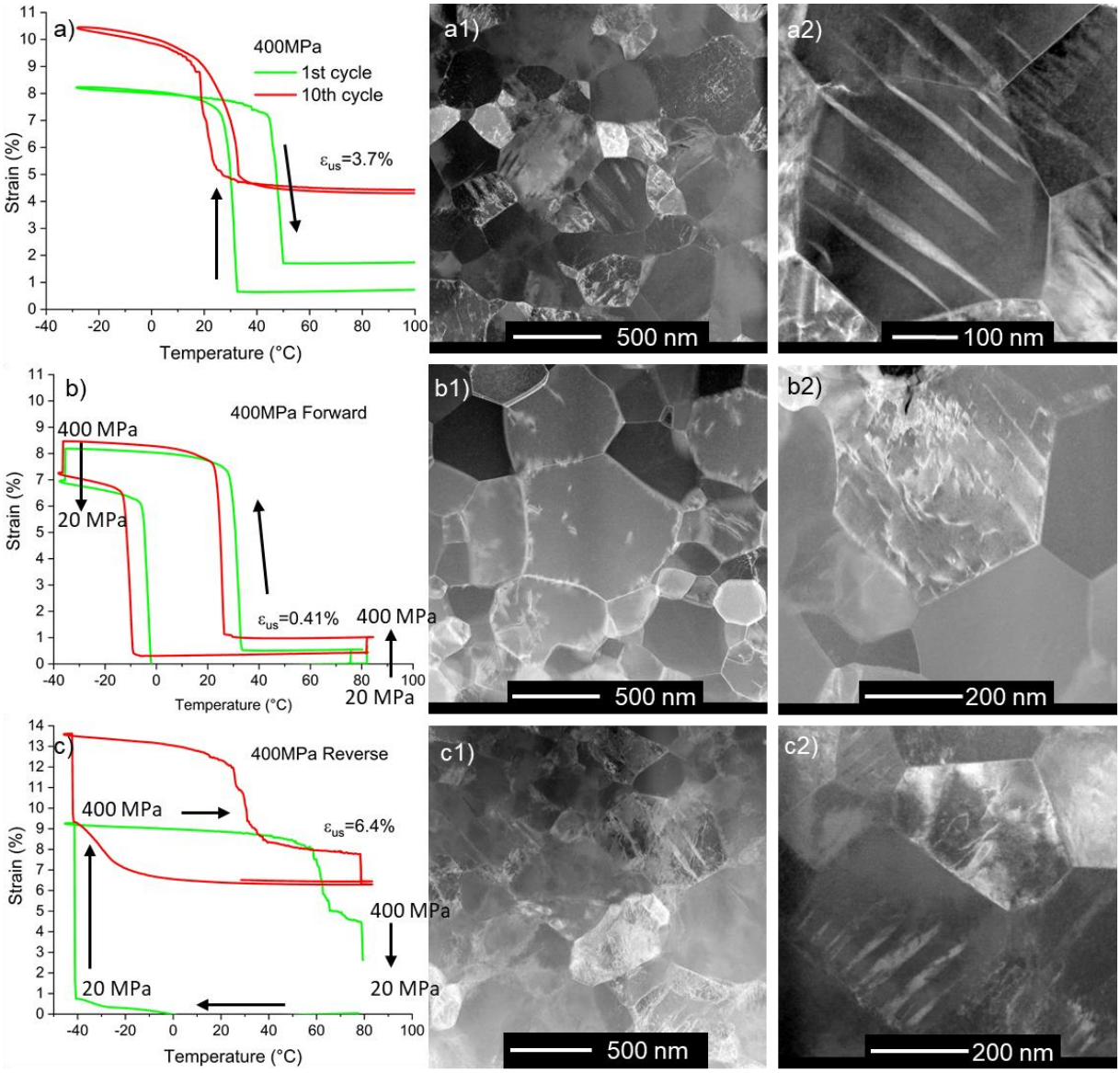

Fig. 13. Thermomechanical loading tests performed to evaluate unrecovered strains and lattice defects generated separately by the forward (b) and reverse (c) martensitic transformation in thermal cycling under constant stress (a). Stress-strain curves recorded in the 1st and 10th cycle in thermomechanical loading tests and resulting lattice defects observed in the microstructure of the cycled wires (a1-c2).

Again, we did not know from the test how much unrecovered strain and how many lattice defects were generated during the forward cooling and reverse heating. The bypass thermomechanical loading tests were performed to find out. While the only small unrecovered strain of ~0.4 % was recorded in the test of forward martensitic transformation during cooling at 400 MPa (Fig. 13b), a very large unrecovered strain of 6.4 % was recorded in Fig. 13c, in which the reverse martensitic transformation proceeded under the same stress only during heating.

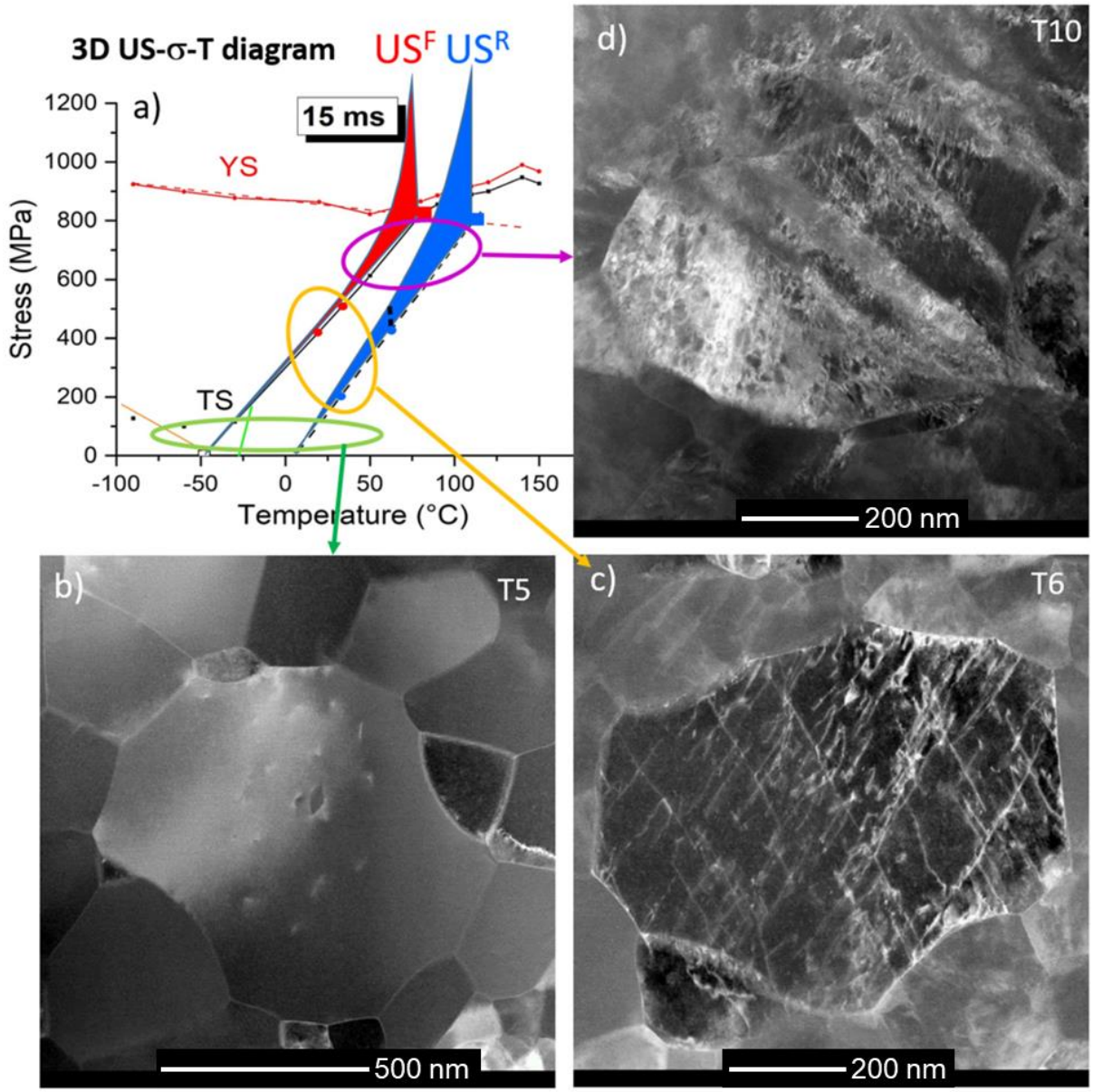

Fig. 14. (a) 3D T–σ–ε_{us} diagram for the 15 ms NiTi wire. Color ellipses mark different magnitude of unrecovered strain generated by the forward and reverse martensitic transformations proceeded at temperature and stress conditions denoted by transformation lines in stress–temperature space; (b) microstructure when martensitic transformation proceeded at low stresses - almost no unrecovered strain and very few permanent lattice defects in a form of dislocation loops were generated; (c) dislocations in {110}<001> slip system and medium unrecovered strains were generated when martensitic transformation proceeded at intermediate stresses; (d) deformation bands containing {114} austenite twins and/or single variant residual B19' martensite plates [41] together with a high density of unidentified dislocations were observed when martensitic transformation proceeded at high stresses.

The microstructures observed in the cycled wires (Fig. 13b, c) agree with the difference in unrecovered strains. It appears that the permanent lattice defects (slip dislocations and deformation bands) were generated mainly during the reverse heating under stress. The unrecovered strain and amount of lattice defects generated in the test (cyclic reverse transformation under stress) are much higher than in the conventional cyclic thermal test under 400 MPa. The unrecovered strain and type of lattice defects generated under various stresses and temperatures are summarized in Fig. 14. The 3D T–σ–ε_{us} diagram in Fig. 14 shows unrecovered strains accumulated in 10 thermomechanical loading bypass cycles, in which forward or reverse martensitic transformation proceeded at temperature and stress conditions denoted by transformation lines in stress–temperature space. The three color ellipses drawn in the 3D T–σ–ε_{us} diagram denote [temperature, stress, strain] conditions under which very different unrecovered strains and lattice defects were observed.

13 ms microstructure

Cyclic shape memory and bypass tests separating effects of forward and reverse transformations were performed in the case of the 13 ms microstructure as well. Fig. 15 demonstrates how much of unrecovered strain (ε_{us} = 1.1 %) is generated in the first superelastic cycle at 80 °C. The forward transformation from austenite to martensite generates ~ 0.65% ε_{us} and reverse transformation generates an even higher ε_{us} of 0.8 %, when it precedes the forward transformation of a conventional superelastic cycle. Note that sum of ε_{us} in the 'forward' and 'reverse' tests is larger than ε_{us} in the conventional cycle at 80 °C, where the forward precedes the reverse transformation, giving a 'strain hardening' effect.

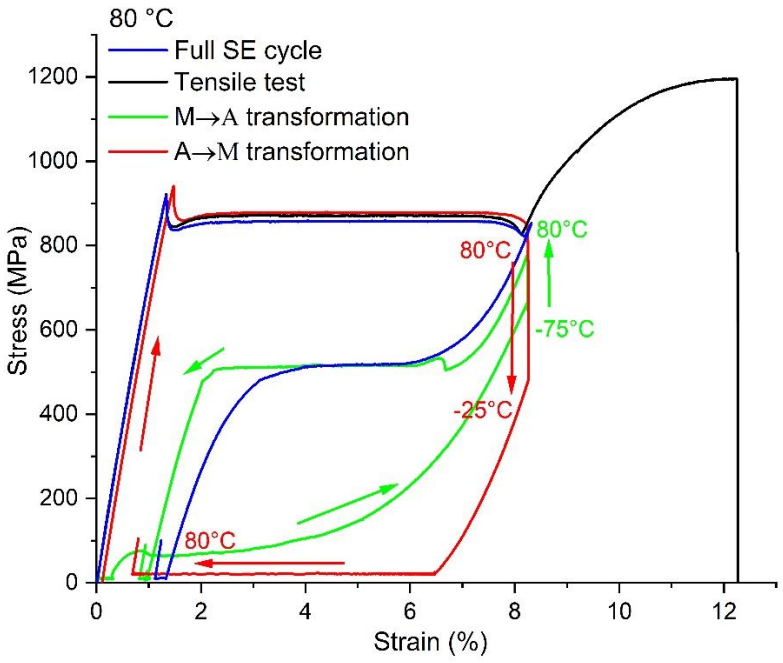

Fig. 15. Thermomechanical loading tests performed to evaluate unrecovered strains generated separately by the forward (red) and reverse (green) martensitic transformation in the superelastic test at 80 °C.

Less than 0.05 % of unrecovered strain was generated both in the tensile loading of martensite at -90 °C (Fig. 16a, g) and austenite at 150 °C (Fig. 16c, i), and very few dislocation defects were observed by TEM in the wires since there was no martensitic transformation proceeding

under stress. It shall be noted that this was the case despite the large stress (900 MPa) and large strain (9 %) applied in the shape memory tests (Fig. 16a, g). This evidence shows that if the austenite and martensite phases do not transform under high stress, they are highly resistant to dislocation slip or any other source of inelastic deformation. Additionally, a significant unrecovered strain of 1.1 % (1.3 % without recovery of residual martensite) is generated by the forward and reverse martensitic transformation in the same wire at approx. 900 MPa and 500 MPa, respectively, even though the maximum stress and strain in the loading cycle are comparable to the previous tests performed at -90 °C and 150 °C. The accumulated unrecovered strain exceeds 3 % in just 10 cycles of superelastic tensile loading at 80 °C and the wire fails at ~ 900 cycles (Fig. 16h).

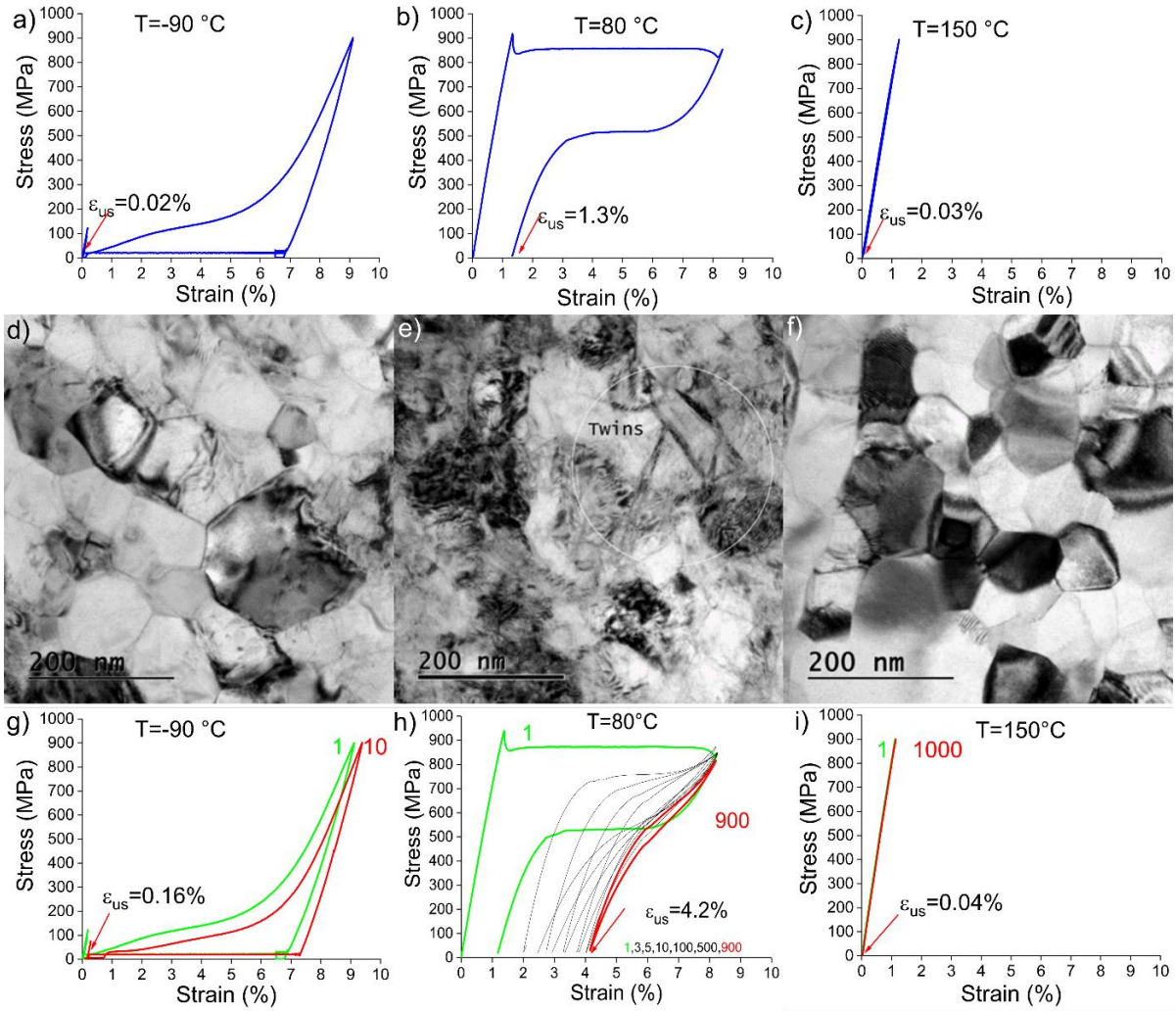

Fig. 16. Stress-strain response of the NiTi wire in tensile tests at various temperatures: (a) -90 °C (b) 80 °C, (c) 150 °C. Lattice defect observed in the microstructure (bright-field TEM micrographs) after deformation (d, e, f) and the cyclic stress-strain response recorded in cyclic tensile tests (g, h, i). The wire is heated/cooled stress-free to restore the austenite prior to the next tensile loading in the case of (g). Since no martensitic transformation under stress takes place in the tests (a, g) and (c,i), lattice defects and unrecovered strain are massively generated only in b) and h).

Although accumulation of unrecovered strain is mainly affected by transformation stresses and the maximal stress in a loading path has a minor effect, overloading of superelastic NiTi alloy beyond the plateau strain decreases reverse transformation plateau stress (Fig. 17). The downward shift of reverse transformation stress is related to the extra energy needed to

overcome problems at the habit plane during the reverse transformation as additional deformation beyond plateau strain rearranged martensitic variants. This effect is also called the "stabilization of martensite by deformation" [119]. The sample deformed up to the 1300 MPa did not recover upon unloading and had to be heated up to 35 °C (~ 40 °C above the original A_f temperature, see Fig. 17). Surprisingly, the recoverable strain after the complete thermomechanical loading cycle was 12 % (permanent strain only 0.9 %). That is nearly twice as large of a recoverable strain as commonly considered for NiTi polycrystalline wire. Therefore, the final part of the tensile test curve beyond the upper-stress plateau is not conventional elastoplastic loading and additional partially reversible martensite twinning. Based on this evidence, superelastic fatigue cycling has to be limited by the end of the transformation plateau to prevent any potential overloading and martensite stabilization effects.

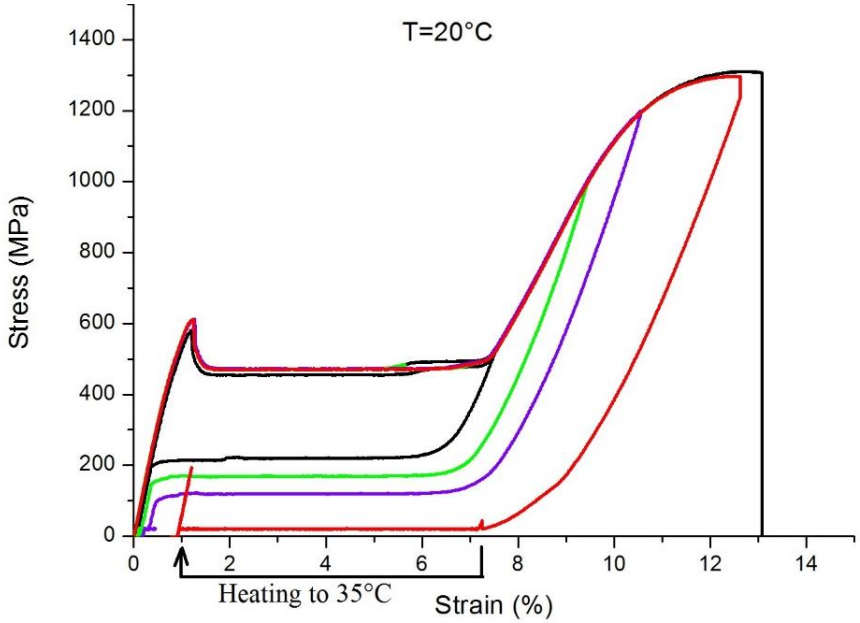

Fig. 17. Stress hysteresis increase due to the stabilization of martensite by deformation - superelastic loading of the 13 ms sample at 20 °C to 600 MPa (black), 1000 MPa (green), 1200 MPa (purple), and 1300 MPa (red).

16 ms microstructure

Experimental results in Fig. 18 (stress-strain-temperature records and bright-field (BF) TEM micrographs partially taken from [40]) demonstrate how the virgin austenitic microstructure of the NiTi wire gradually evolves upon tensile deformation from 10% to 20% strain at room temperature. Recall that after tensile deformation and unloading, the wires were always heated up to 150 - 200 °C to complete the strain recovery and the effect of martensite stabilization can be observed as well. As a result, the microstructures in Fig. 18 are thus mainly austenitic, very rarely with R-phase or B19' martensite in deformation bands. All stress-induced B19' martensite existing in the wire under peak stress thus retransformed to the austenite upon unloading and heating. In this way, lattice defects observed in Fig. 18 in the austenite phase were probably created by the tensile deformation presumably in the martensite state. Those defects were inherited by the austenite phase during the reverse transformation upon unloading and heating.

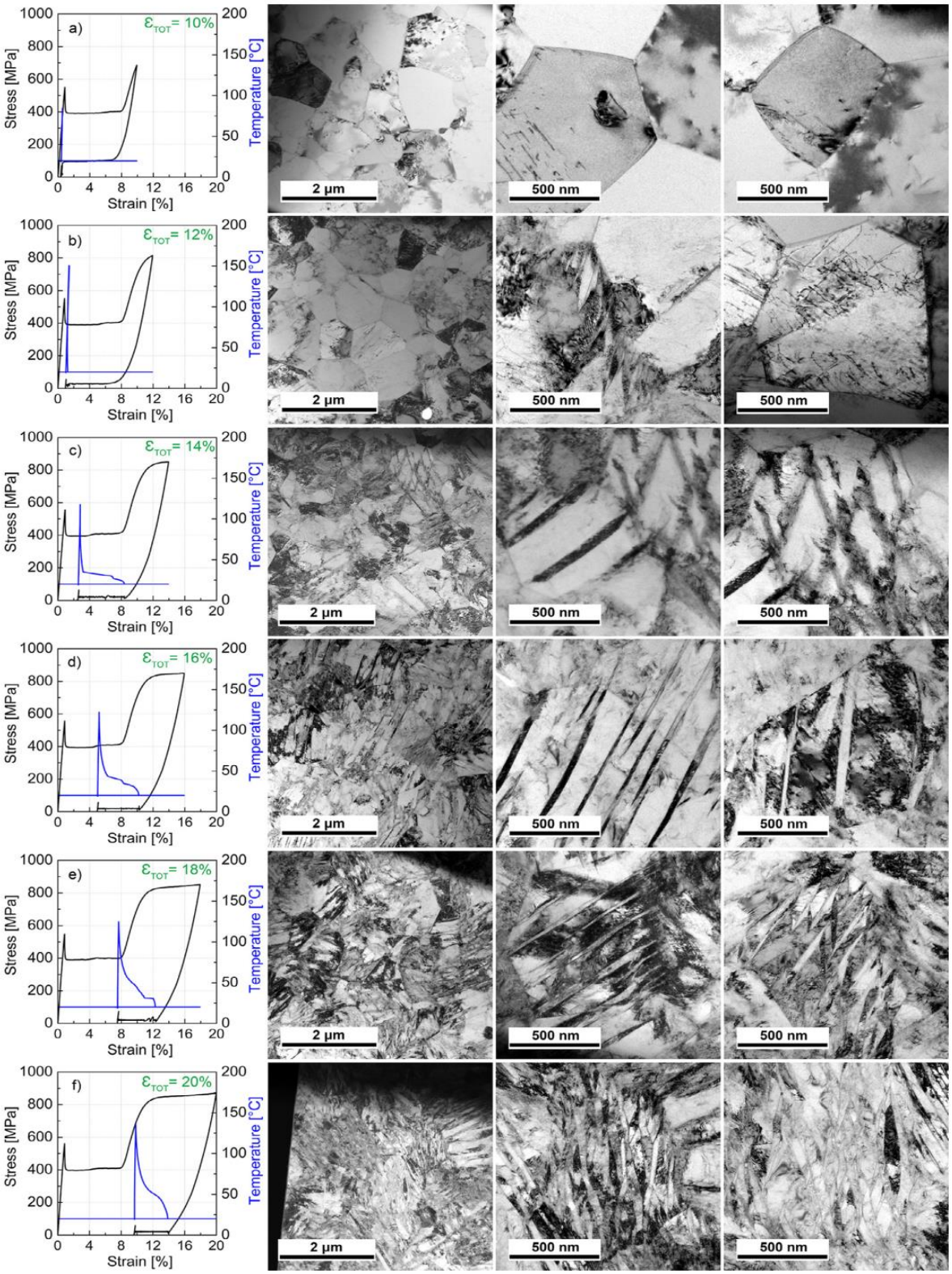

Fig. 18. Stress-strain-temperature curves and microstructures observed in superelastic NiTi wire deformed at room temperature up to 10–20% strain, unloaded, heated under 20 MPa stress until the end of the strain recovery, and cooled back to room temperature. The data were partially taken from Ref. [40]. Three BF images in each row characterize lattice defects (deformation bands with {114} austenite twins, R-phase or B19'martensite and slip dislocation) created during the thermomechanical loading tests, the results of which are shown in the left column.

After tensile deformation up to 10% strain, only isolated dislocations and dislocation loops at oxide particles remained in the unloaded and heated microstructure (Fig. 18a). At 12% strain (Fig. 8b), a significant density of slip dislocations corresponding to <100>{011} slip systems appeared in the microstructure. Starting from 14% strain (Fig. 18c-f), deformation bands appeared in the microstructure and their density gradually increased with increasing total strain. Although there is dislocation contrast within the deformation bands, these are not conventional shear bands associated with localized deformation via dislocation slip. The deformation bands were found to contain single variant crystal lattices different from the austenite matrix (austenite twin, R-phase, or B19' martensite). At 14% (Fig. 18c) and 16% strain (Fig. 18d), the deformation bands containing R-phase prevailed over those containing {114} austenite twins. At 18% strain (Fig. 18e), deformation bands containing {114} austenite twins started to dominate the microstructure (Fig. 19). There is strong dislocation contrast both within the austenite matrix and austenite twins. At 20% strain (Fig. 18f), the microstructure mainly consists of a high density of deformation bands formed by {114} austenite twins, although deformation bands containing R–phase were sometimes found in this microstructure as well.

It shall be pointed out that the wire was completely martensitic when it was loaded beyond the end of the stress plateau in the tensile test, as was confirmed by the in-situ synchrotron x-ray diffraction method [86]. We see in Fig. 18a,b, no deformation bands appear in the tensile test up to the yield point.

TEM analysis of the microstructure in the plastically deformed, unloaded, and heated/cooled wire revealed deformation bands (Figs. 18c-f) containing mainly austenite phase (Fig. 19) and/or R-phase. This means that all martensite, which remained in the microstructure of the wire deformed up to 18% after unloading, transformed to the austenite phase upon heating (Fig. 19). Note that ~5% inelastic strain was recovered on heating (Fig. 18e). The microstructure of the wire after heating/cooling is dominated by the $\{114\}_{B2}$ austenite twins (Fig. 19) extending across whole grains, sometimes forming wedges and/or crossing over grain boundaries. Note that the spots in diffraction patterns taken from the unloaded and heated/cooled microstructure in Fig. 19 are broadened in an azimuthal direction. The larger the SAED area, the stronger is the azimuthal spreading (Fig. 19c,d). This was attributed to the various austenite lattice rotations in different locations within the grain introduced during the reverse martensitic transformation upon unloading and heating under 20 MPa stress [40].

Fig. 20 shows that, even though the wire was deformed to 8% strain and transformed completely to the martensite in the first tensile cycle at room temperature, practically no lattice defects remained in its microstructure after unloading and heating. Upon further tensile cycling, however, slip dislocations and deformation bands gradually appeared in the microstructure, as evidenced by bright-field TEM images taken after the 2nd, 5th and 20th cycle at 20 °C and 50 °C. It shall be mentioned that the cycled wire was not heated to 150 °C after unloading. Massive deformation bands appear in the 20th cycle at room temperature alongside a high density of slip dislocations. The stress-strain response of the wire is much more unstable in tensile cycling at 50 °C. Deformation bands appear already in the 1st cycle and a high density of bands was found in the microstructure after the 2nd cycle.

The loss of the plateau type stress-strain response upon cycling correlates with the appearance of deformation bands in the microstructure of cycled wires. The observed deformation bands are similar to the bands observed in the same wire deformed only once beyond the yield point (Fig. 18). However, in contrast to the bands in Fig. 18, most of the bands in Fig. 20 contain a single variant of the B19' martensite or R-phase, while only very few bands contain {114} austenite twins.

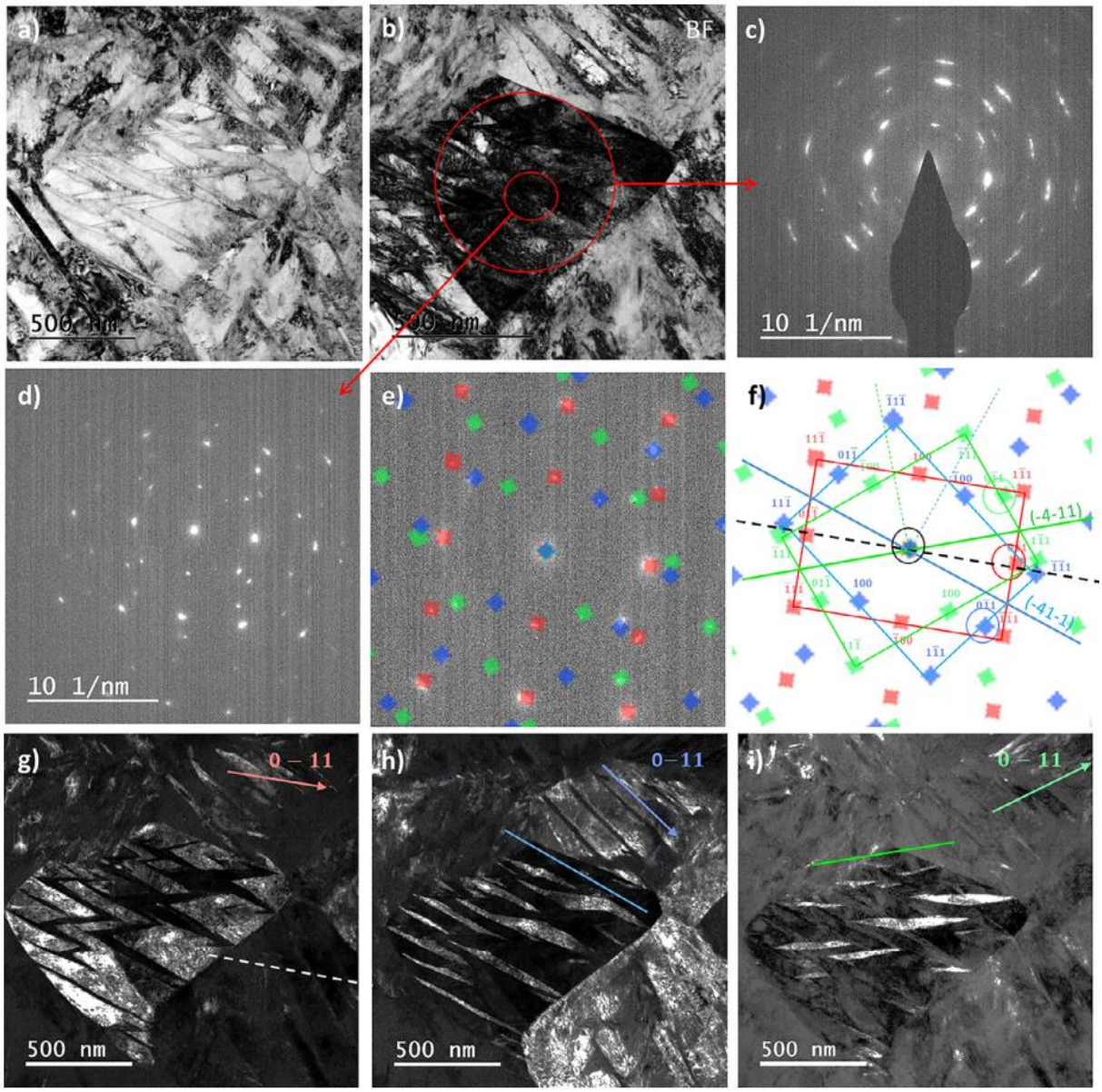

Fig. 19. Microstructure in NiTi wire deformed to 18 % at room temperature, unloaded, heated to 150 °C under 20 MPa, and cooled to room temperature (corresponding to Fig. 18e): (a) a grain with multiple wedge-shaped deformation bands was selected for the analysis; (b) the lamella was tilted into the [011] crystal zone, and the deformation bands nearly disappeared; diffraction patterns from the large (c), and small (d) selected areas differ in the azimuthal spreading of spots; pattern in (c) is due to the diffraction from multiple slightly misoriented austenite domains within the large area. The diffraction pattern from the small selected area is indexed in (e) as belonging to the austenite matrix (red) and two austenite twins (green, blue). Dark-field (DF) images taken using the denoted spots visualize the austenite matrix (g), $(11–4)_{B2}$ austenite twins (h), and $(1–14)_{B2}$ austenite twins (i). Traces of the observed austenite twin planes are denoted by colored lines in (f, g, h, i). The black dashed line denotes $(100)_{B2}$ austenite twin plane between the green and blue lattices.

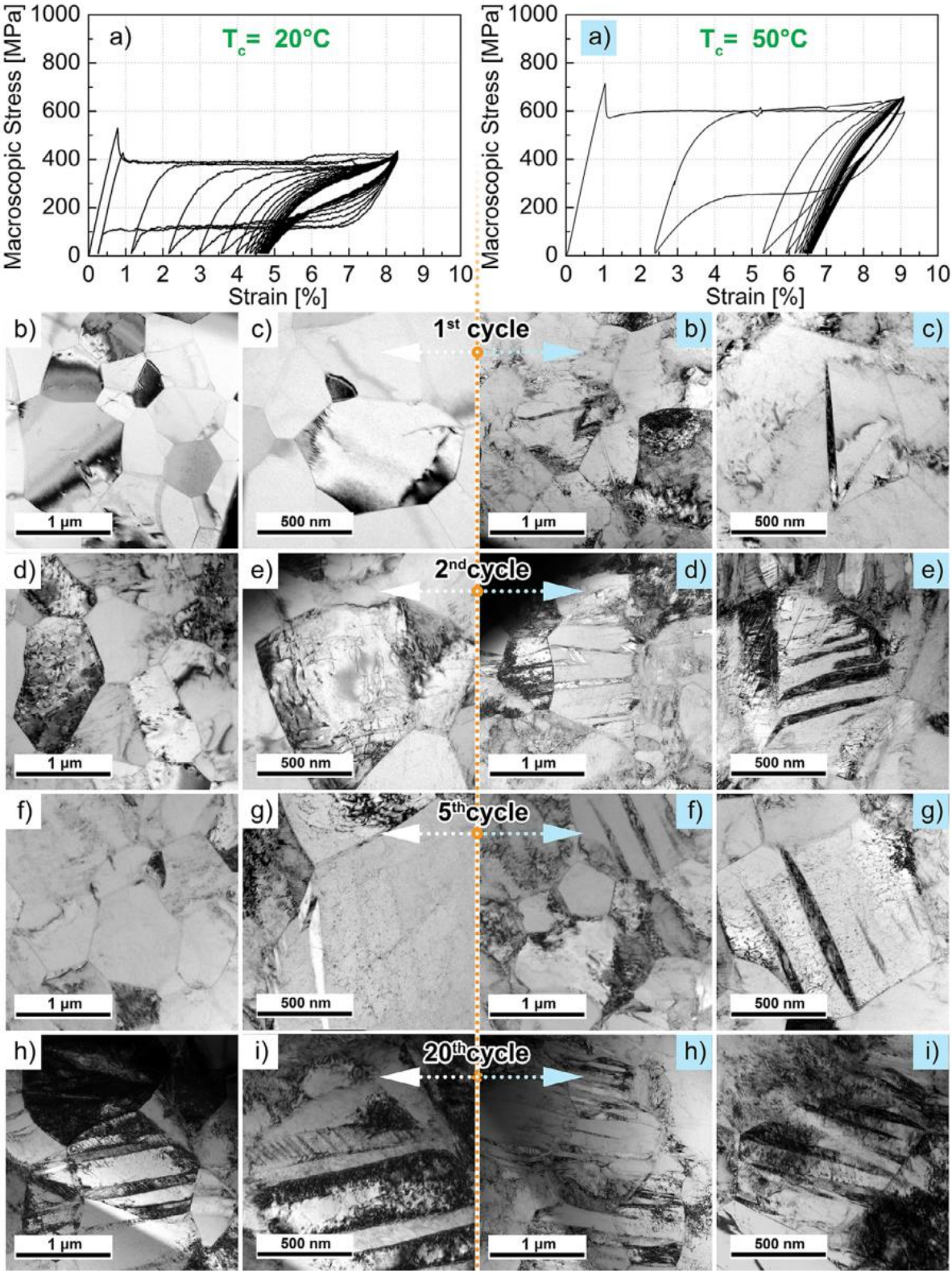

Fig. 20 Cyclic stress-strain response recorded in cyclic tensile tests on the 16 ms NiTi wire at 20 °C (left) and 50 °C (right). 20 superelastic cycles until the end of the stress plateau were performed in a strain control regime. Microstructure observed after unloading in 1st, 2nd, 5th and 20th cycle demonstrate the evolution of the wire microstructure upon cycling.

4.1.4 Characterization of NiTi wires with aged microstructures

In general, the aging of Ni-rich NiTi can significantly alter thermomechanical response (as demonstrated in sections 1.3.1 Precipitation and 1.4 R-phase). This section shows microstructures and mechanical behavior of samples that were subjected to the 400°C/1h aging after various pulse heat treatments by electric current (13 ms, 15 ms, and 20 ms) that generate microstructure with the average grain size of 75 nm, 250 nm, and 5 μm respectively. Note that the additional aging does not change even the lowest average grain size used in these experiments (see Fig. 3g,h).

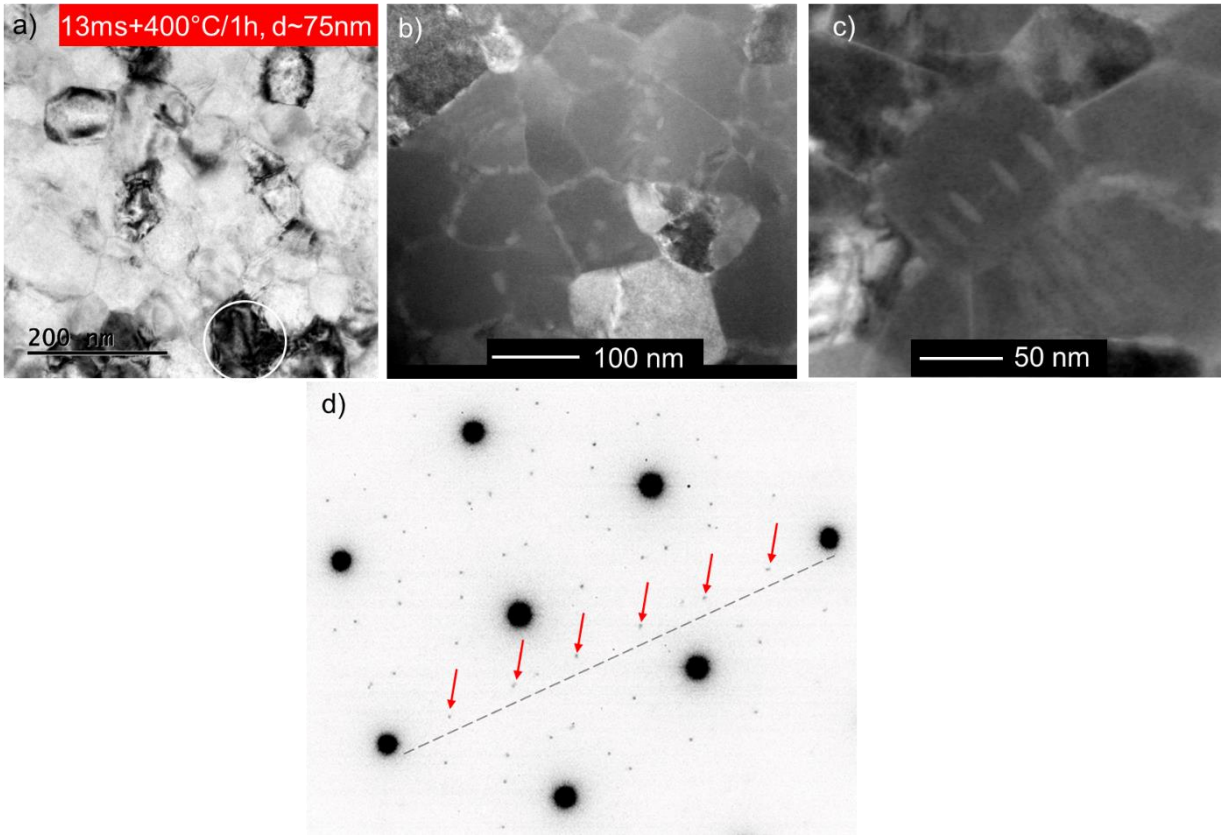

Fig. 21. Microstructure of the 13 ms NiTi wire after additional aging treatment at 400 °C for 1 h: (a) TEM micrograph, (b) STEM micrograph showing preferential precipitation along grain boundaries, (c) detail of grain with precipitates in the grain interior, and (d) the $<111>_{B2}$ SAD pattern from the region highlighted by a white circle in (a) showing additional diffraction spots at $1/7<123>_{B2}$ positions generated by the Ni_4Ti_3 precipitates.

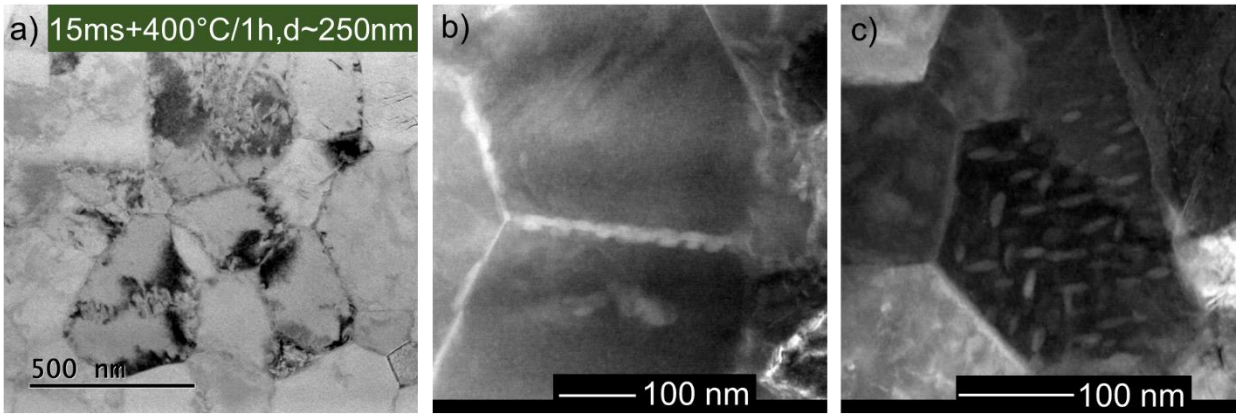

Fig. 22. Microstructure of the 15 ms NiTi wire after additional aging treatment at 400 °C for 1 h: (a) TEM micrograph, (b) STEM micrograph showing preferential precipitation along grain boundaries and c) detail of grain with precipitates in the grain interior.

As shown in Figs. 4, 23, additional 400°C/1h aging of the 13ms samples increases tensile strength by about 200 MPa and decreases transformation stresses by 170 MPa. Micrographs in Fig. 21 reveal that the aging generates Ni-rich precipitates (identified as Ni_4Ti_3 phase based on their shape, the applied aging parameters, and SAD pattern corresponding to observations in [60][64]) that nucleate preferentially along grain boundaries. The average size of precipitates is approx. 20 nm in length and 8 nm in thickness. The same aging treatment of the 15 ms microstructure (d ~ 250 nm) results in a similar distribution of precipitates (Fig. 22 b,c), but the size of these particles is slightly larger (approx. 28 nm in length and 10 nm in thickness) suggesting lower efficiency in the age hardening of the NiTi matrix. That was confirmed by the tensile test showing a lower increase in tensile strength by 100 MPa compared to the aging of 13 ms samples. Moreover, a lower decrease in plateau stress by 140 MPa indicates slower kinetics of precipitate's nucleation, probably due to the decreased amount of grain boundaries compared to the 13 ms samples and larger grain size accentuates preferential nucleation along grain boundaries as well (see Fig. 22 b). Consequently, the grain interior remains vulnerable to functional degradation at higher temperatures. As a result of the increase in transformation temperatures by the aging, the 15 ms+400°C/1h sample has to be tested at least at 45 °C to finish the superelastic cycle, which leads to extremely unstable functional behavior (Fig. 24). That could be attributed mainly to the relatively high temperature of aging and lower supersaturation by Ni promoting nucleation of Ni-rich precipitates at grain boundaries [57]. Furthermore, a significant decrease in ductility from 56 % to only 14 % indicates that the sample is incapable of homogeneous plastic deformation, and the deformation at high stresses is localized in a small area of necking, where it ruptures. Finally, the aging of 20 ms samples with a grain size of ~ 5 μm results in a negligible change of both plateau stress and tensile strength by ~ 40 MPa, and ductility is moderately decreased from 64 % to 58 %.

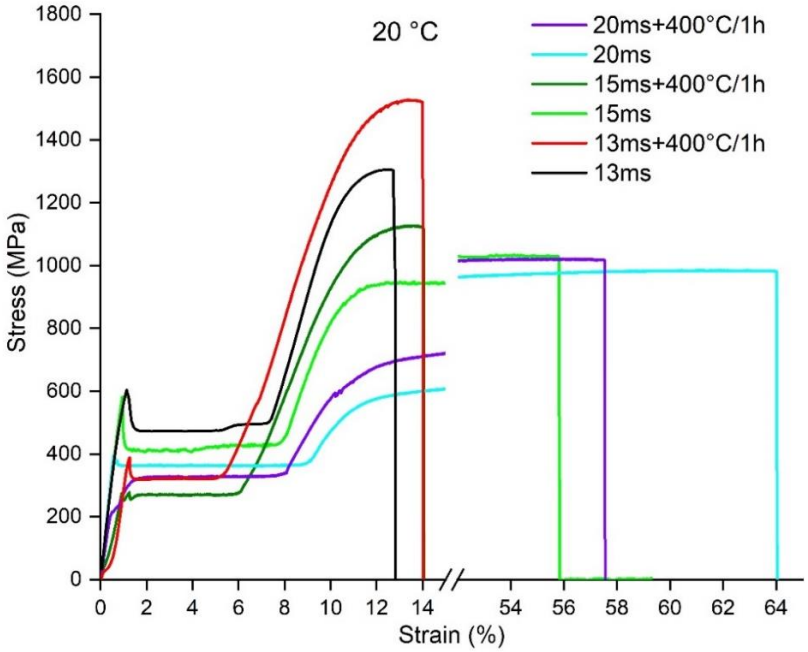

Fig. 23. Mechanical responses of NiTi wires with and without the additional 400°C/1h aging having various grain sizes (13 ms ~ 75 nm, 15 ms ~ 250 nm, and 20 ms ~ 5 μm).

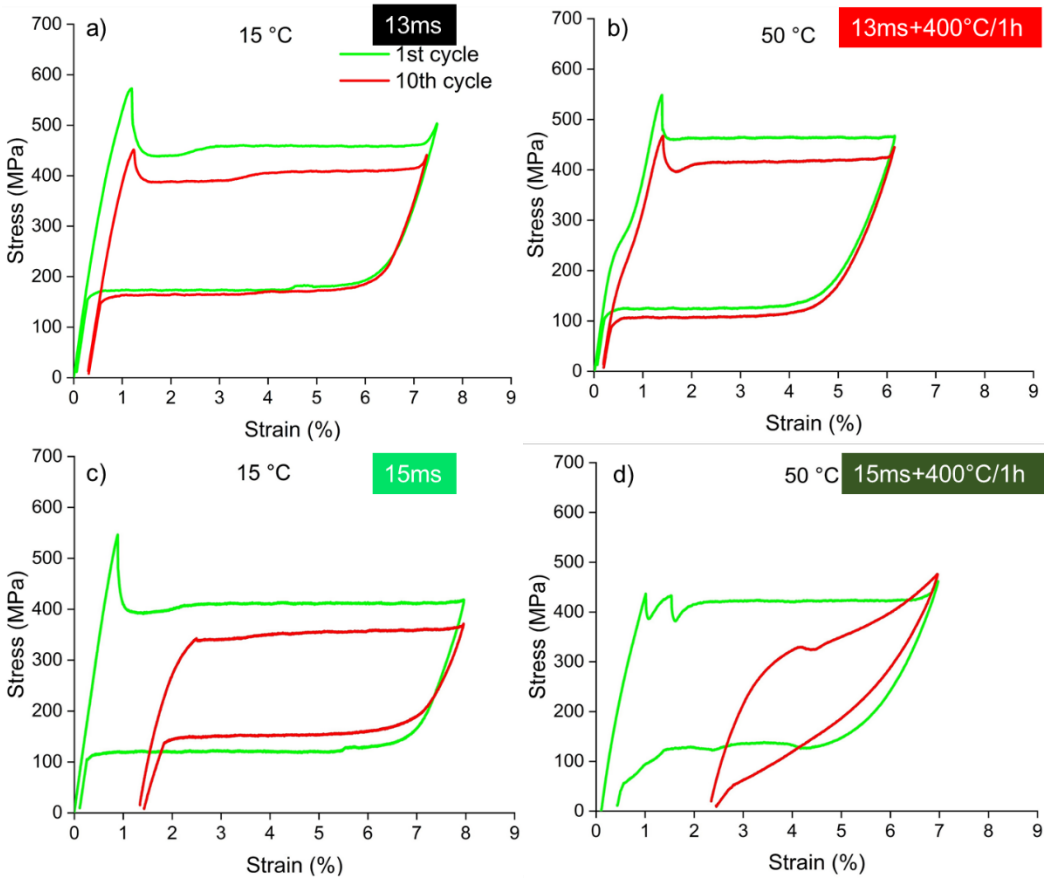

Fig. 24. Mechanical response of a) 13 ms at 15 °C, b) 13ms+400°C/1h at 50 °C, c) 15 ms at 15 °C and d) 15ms+400°C/1h at 50 °C in the first and tenth tensile loading cycle to the end of the superelastic plateau.

Further optimization of aging parameters would be needed in the case of microstructures with larger grain sizes. Initial deformation before low-temperature aging (250 °C/8h) and the introduction of nucleation sites for precipitation in the grain interior could potentially solve this issue as proposed in [20]. On the other hand, the 10 ms pulse annealing yields only partially recrystallized microstructure with similar grain size (d ~ 20 nm) as well as the length of Ni_4Ti_3 precipitates after the 400°C/1h aging. Therefore, aging of the 10 ms wires was not attempted since maintenance of the grain size during the aging was not guaranteed and the effect of aging on functional and fatigue performance would be superimposed with grain growth in this case. Thus, these two aged microstructures were not included in the following fatigue experiments and only one aged sample - 13 ms+400°C/1h (Fig. 32, Table 1) was included.

4.1.5 Characterization of NiTi wires with aged microstructures by SANS

Another possibility to study precipitation processes in NiTi alloys is small-angle neutron scattering (SANS) [17][101]. As neutrons have a much higher penetration depth than electrons, SANS provides information on microstructure (precipitates) from the whole sample (wire) compared to TEM lamella only. Another advantage is that the SANS measurement does not require any time-consuming sample preparation. On the other hand, the measured data provide information only on the size and shape of structural heterogeneities, and neither their chemical composition nor crystal structure can be determined by SANS.

Small-angle neutron scattering (SANS) experiments were performed in the SANS II of the PSI facility in Switzerland (local experimental setup covers measurement up to 100 nm size of defects/heterogeneities) and MAUD of Nuclear Physics Institute of the CAS in Řež (covers detection of defects/heterogeneities above 100 nm). Thirteen wires of a diameter 1.7 mm and length 30 mm were stacked together in a sample holder in this experiment. The samples were annealed at temperatures 350, 400, 450, 500, 550, 600, 650, and 900 °C for 2 h. A 2D record of scattered neutron intensity (Fig. 25a) was then integrated by azimuthal angle and transferred to a 1D curve (Fig. 26) from which size and volume fraction of scattering heterogeneities (Fig. 27) are determined by inverse transformation of the SANS cross-sections. Namely, if their volume fraction is low and there is no inter-particle interference, the SANS nuclear and magnetic cross-sections can be written as

$$\frac{d\Sigma(Q)}{d\Omega} = (\Delta\rho)^2 \int_0^{+\infty} N(R)[V(R)]^2 |F(Q,R)|^2 dR \tag{6}$$

where N(R) is the number per unit volume of defects with a size between R and R + dR, V their volume, $|F(Q, R)|^2$ their form factor (assumed spherical in this case) [120].

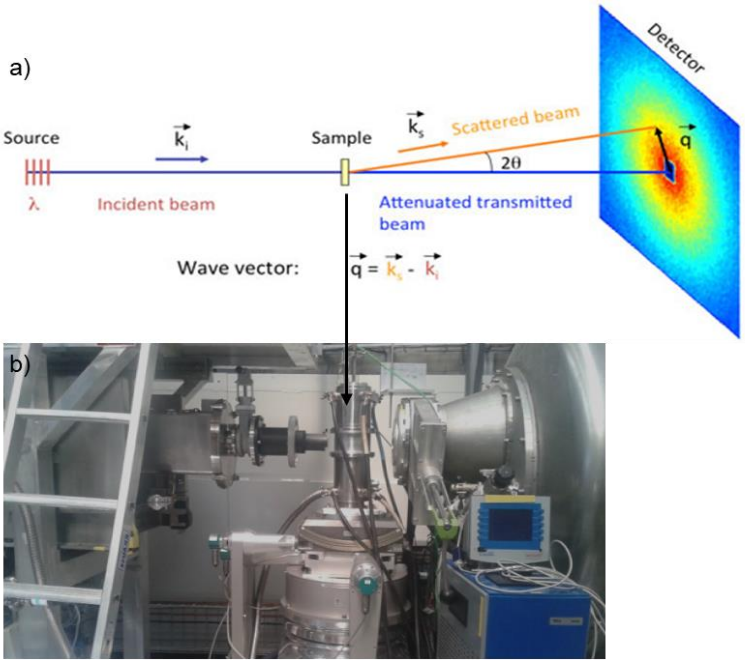

Fig. 25. a) Schematic drawing of neutron path from source through sample to detector. b) Photography of the PSI SANS facility- neutron beam collimator (left), environmental chamber (middle) and neutron detector (right)

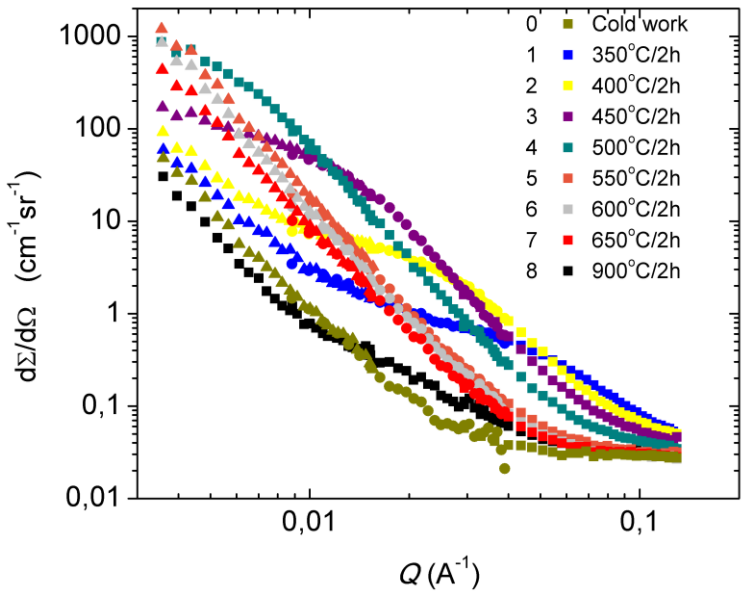

Fig. 26. Nuclear SANS cross-sections for the tested NiTi samples- cold-worked and annealed for 2 h at 350, 400, 450, 500, 550, 600, 650, and 900 °C.

At first, precipitates less than 10 nm in size are created at 350 °C (Fig. 27) and effectively increase tensile strength as stated in the previous section. The size of precipitates gradually increases with temperature. The mean size of the Ni_4Ti_3 precipitates is approx. 20 nm at 400 °C, which corresponds to the TEM observation (Figs. 21, 22). However, there is a huge gap between 500 °C and 550 °C from 50 nm to almost 500 nm, where the volume fraction of precipitates peaks. That phenomenon corresponds to the decrease in tensile strength above 500 °C [56]. Then, the size remains almost constant, but the volume fraction decreases as the solubility of excess Ni in the matrix increases. Finally, only inclusions of TiC remain at 900 °C. Those

inclusions are always present in the NiTi matrix, and the mean size is approx. 800 nm with larger scatter than precipitates, which corresponds to SEM observation of fatigue fracture surfaces (Fig. 34-37).

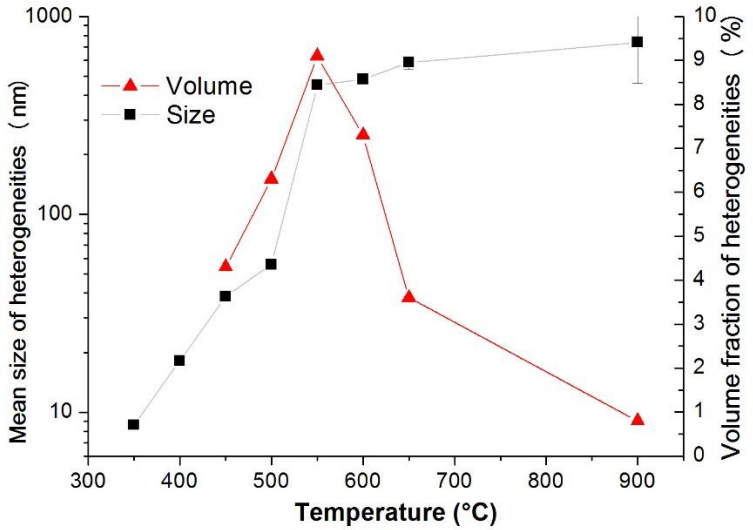

Fig. 27. Mean size of precipitates (structural heterogeneities) after aging for 2h at 350 °C, 400 °C, 450 °C, 500 °C, 550 °C, 600 °C, 650 °C, and 900 °C and their volume fraction in NiTi matrix based on the SANS measurements.

4.2 Fatigue experiments

Fatigue experiments of pulse heated and precipitation hardened wires were performed to find out the influence of precipitates and ambient temperature on fatigue life. Another motivation for the experiments is to find out a general criterion for fatigue life prediction based on available values of transformation stresses, accumulation of permanent strain, or transformation strain. The maximal strain of superelastic cycles was set to the end of the upper transformation plateau with respect to martensite stabilization.

The temperature range, in which fatigue tests were performed, was set based on the experimental results in Figs. 3-7. In order to accomplish the full superelastic cycle during the whole fatigue life, the lower temperature limit was set at a temperature well above A_f, so that the gradual decrease of the lower plateau stresses during the tensile cycling did not affect the strain recovery upon unloading. The effect of a higher strain rate applied in fatigue tests had to be also accounted for. The upper-temperature limit was set mainly with respect to an excessive accumulation of unrecovered strain ε_{us} at high temperatures. The actual temperature range of fatigue tests (indicated by color bars in Fig. 7b) varies quite significantly for the NiTi wires with different microstructures based on these criteria.

The key issue in the planning of the fatigue experiments was the cyclic instability of stress-strain response at various temperatures. In order to document qualitatively different cyclic instabilities of stress-strain curves, superelastic stress-strain curves of the tested wires were recorded as they gradually evolved during the tensile fatigue test until failure (Figs. 28-31). The cyclic stress-strain curves of the 10 ms wire maintain both upper and lower plateaus upon cycling up to the failure in the whole temperature range (Fig. 28). Moreover, the 10 ms wires exhibit the lowest accumulation of ε_{us} among the tested microstructures.

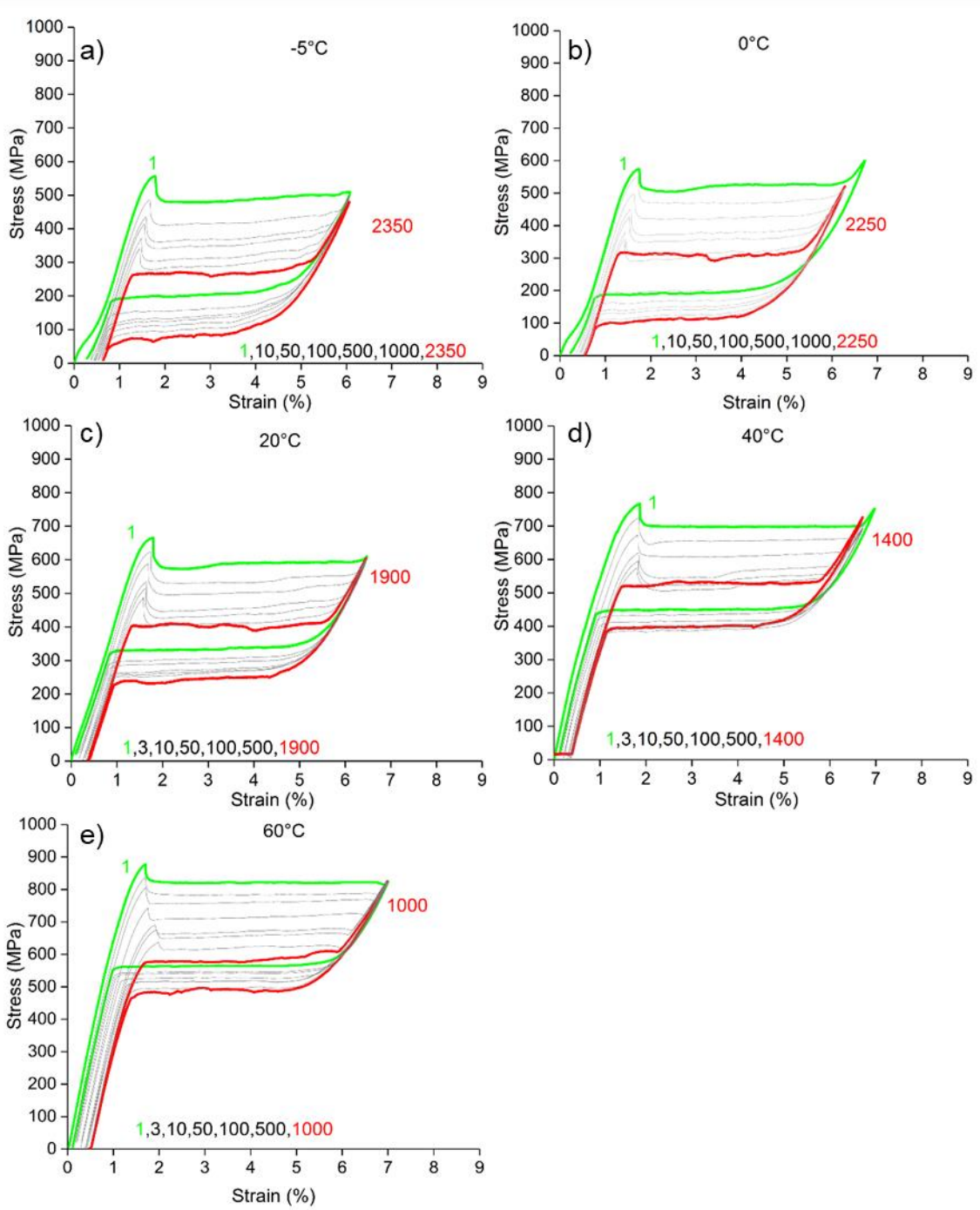

Fig. 28. Stress-strain response of the 10 ms wire in superelastic tensile cycles at constant temperature until fracture: a) -5 °C, b) 0 °C, c) 20 °C, d) 40 °C, and e) 60 °C.

However, a decrease of plateau stresses (especially the upper one) cannot be avoided at any temperature. Moreover, the decrease in upper plateau stress σ_p^{up} is always around 200-250 MPa, regardless of the applied heat treatment. The 13 ms samples show stable superelastic behavior with respect to the accumulation of ε_{us} at low temperatures close to A_f. The stability significantly decreases with increasing temperature and the wire is unable to maintain a stress plateau above 50 °C (Fig. 29).

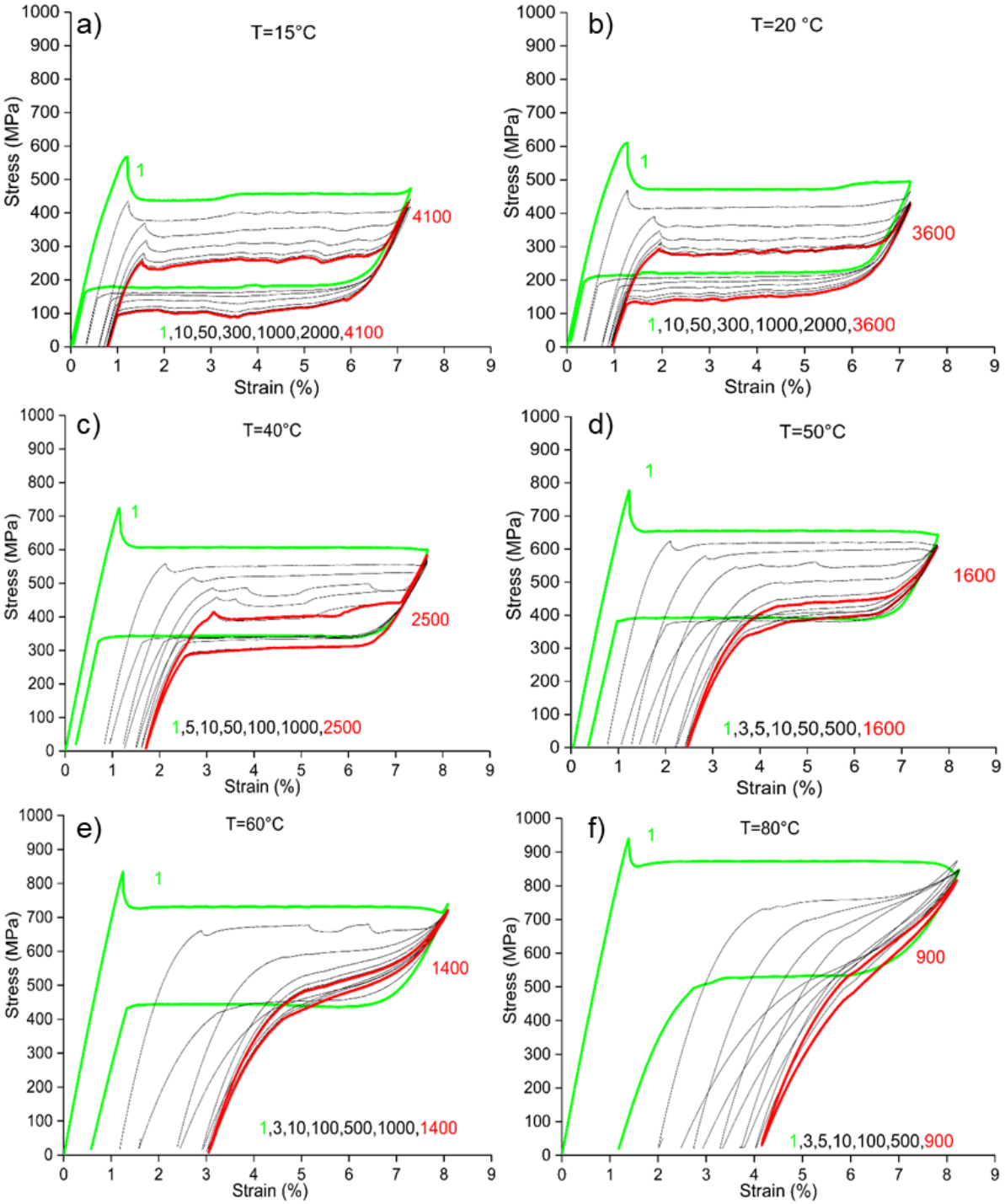

Fig. 29. Stress-strain response of the 13 ms wire in superelastic tensile cycles at constant temperature until fracture: a) 15 °C, b) 20 °C, c) 40 °C, d) 50 °C, e) 60 °C and f) 80 °C.

A similar development of stress-strain response was observed in the case of the aged sample as well, but the temperatures are shifted up by ~ 30 °C due to precipitation (Fig. 30). In contrast to the 10 ms wire, the 15 ms wire shows a rapid accumulation of ε_{us} in the initial phase that lasts only 10 to 50 cycles and slower accumulation further on, which gives rise to the two stages of the fatigue test (Fig. 31). The cyclic stress-strain curves exhibit character similar to the 13 ms microstructure at high temperatures and stress plateaus can be maintained at 15 °C only. The total accumulated ε_{us} during any fatigue test of the 15 ms wire always exceeds 2.5 %.

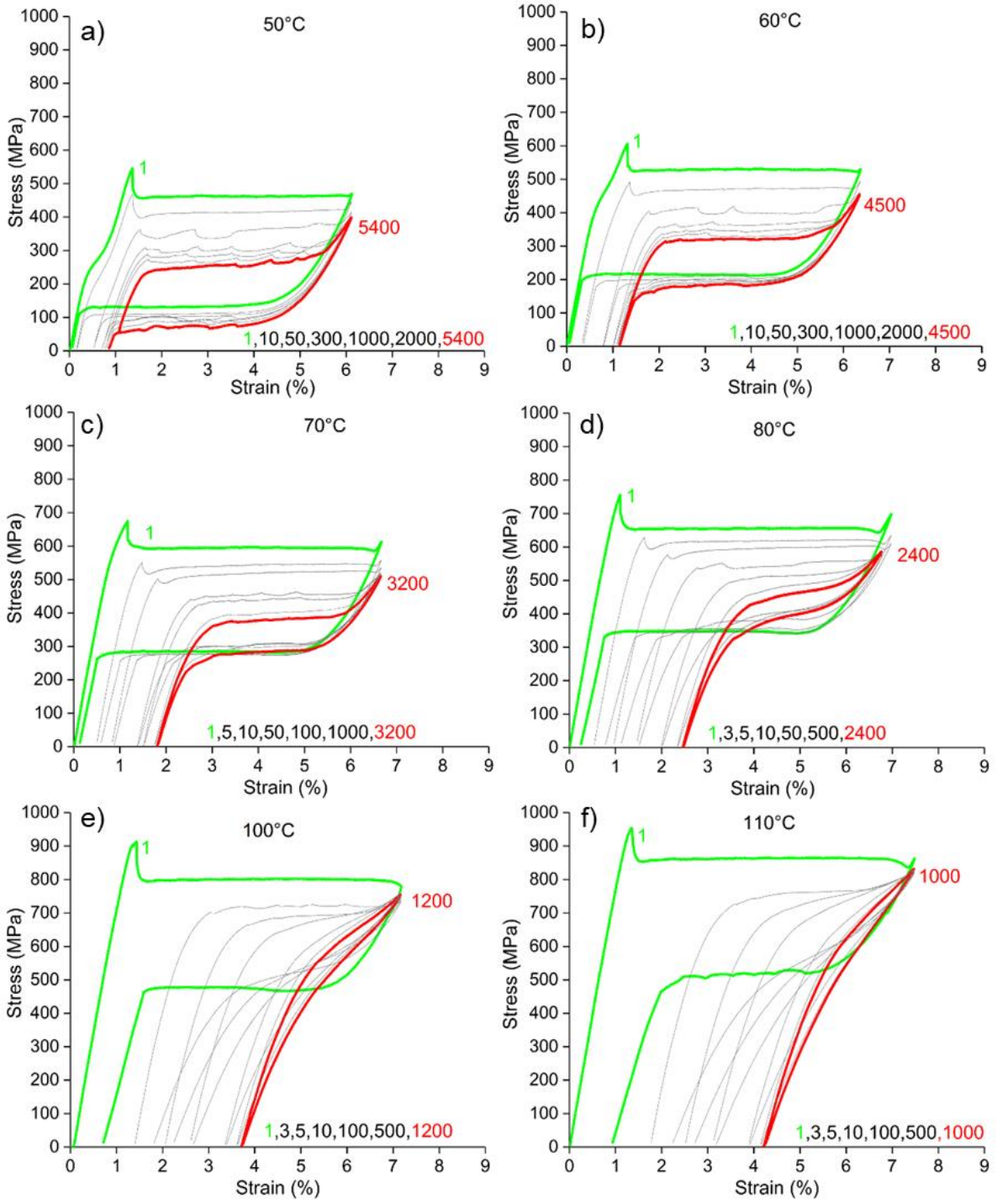

Fig. 30. Stress-strain response of the 13 ms+400°C/1h wire in superelastic tensile cycles at constant temperature until fracture: a) 50 °C, b) 60 °C, c) 70 °C, d) 80 °C, e) 100 °C, and f) 110 °C.

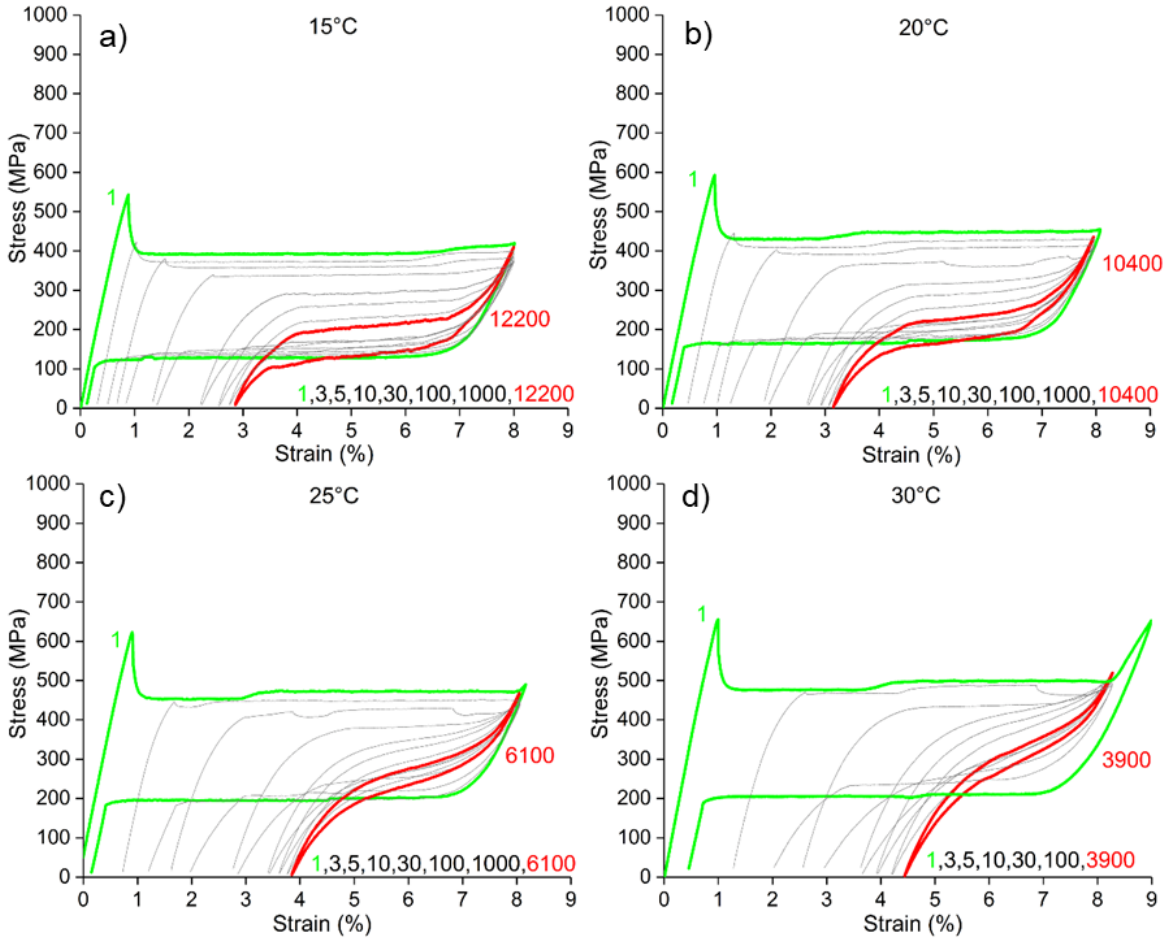

Fig. 31. Stress-strain response of the 15 ms wire in superelastic tensile cycles at constant temperature until fracture: a) 15 °C, b) 20 °C, c) 25 °C, and d) 30 °C.

Knowing that stabilization of functional degradation occurs mainly in the early stages of fatigue life, accumulation of permanent strain in a few cycles (possibly even in the first cycle) could be utilized for fatigue life prediction. The accumulated unrecovered strains evaluated from the above-presented fatigue tests are plotted as a function of the number of cycles in Fig. 32. The obtained dependences plotted in a logarithmic scale show two stages differing in slopes. The 10 ms wires show by far the best functional stability in the tested temperature range (-5 °C to 60 °C) and the accumulated ε_{us} never exceed 0.5 % strain (the effect of irreversible R-phase is excluded in Fig. 32a). Moreover, the accumulation of ε_{us} at the lowest temperatures almost lacks the initial stabilization stage, and ε_{us} thus slowly increases throughout the whole fatigue life. On the other hand, the 15 ms wire exhibits at least five times the higher accumulation of ε_{us}, and more than 70 % is accumulated in only 10 loading cycles. The 13 ms wires (with and without the aging) behave similarly to the 10 ms wire at low temperatures and similarly to the 15 ms wire at higher temperatures. Moreover, the samples show almost identical dependence of fatigue life on accumulated permanent strain (Fig. 32 and 33c) and the origin of that behavior could be related to similar grain size and dislocation activity. The wires behave in the same manner with respect to the accumulation of permanent strain regardless of aging (presence of Ni_4Ti_3 precipitates) and different tensile strength. The data shows potential to further increase fatigue life by a decrease in transformation stresses via ambient temperature or Ni-rich precipitates. Unfortunately, high-stress hysteresis of fully superelastic cycling is always a

limiting factor. Regardless of decreased transformation stresses by aging, temperature, or functional fatigue, the number of fatigue cycles is below the limit desired by industrial applications (>10^5-10^6 cycles).

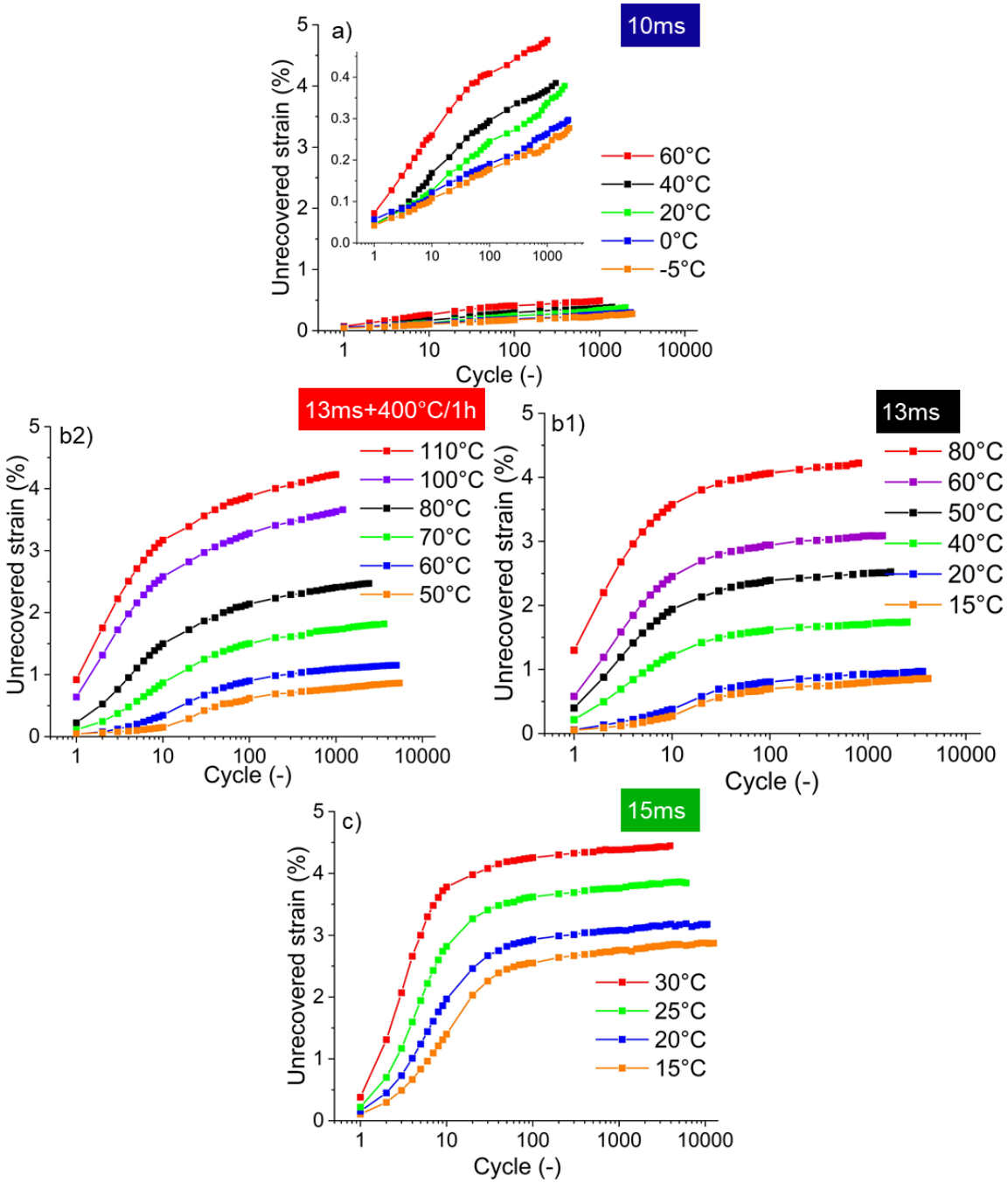

Fig 32. Accumulation of unrecovered strain in fatigue tests on NiTi wires at various temperatures: a) 10 ms, b1) 13 ms, b2) 13 ms+400°C/1h and c) 15 ms samples.in logarithmic scale. The majority of the unrecovered strain is accumulated in stage I (10-50 cycles) and after the transition to stage II, follows approximately a linear increase in the unrecovered strain.

Figure 33 is the key figure of this work summarizing the fatigue life of the 4 different microstructures dependent on the test temperature, upper plateau stress, and unrecovered strain. The results are also summarized in Table 1. In general, we observe that the closer the test temperature is to the A_f, the lower the upper plateau stress, the better the functional stability in the superelastic loading regime is and the longer is the fatigue life. This clearly points out the

essential role of upper (and lower) plateau stress in structural fatigue. Decreasing fatigue life with increasing unrecovered strain (Fig. 33c) points out the detrimental effect of plastic deformation accompanying the stress-induced martensitic transformation on structural fatigue as well.

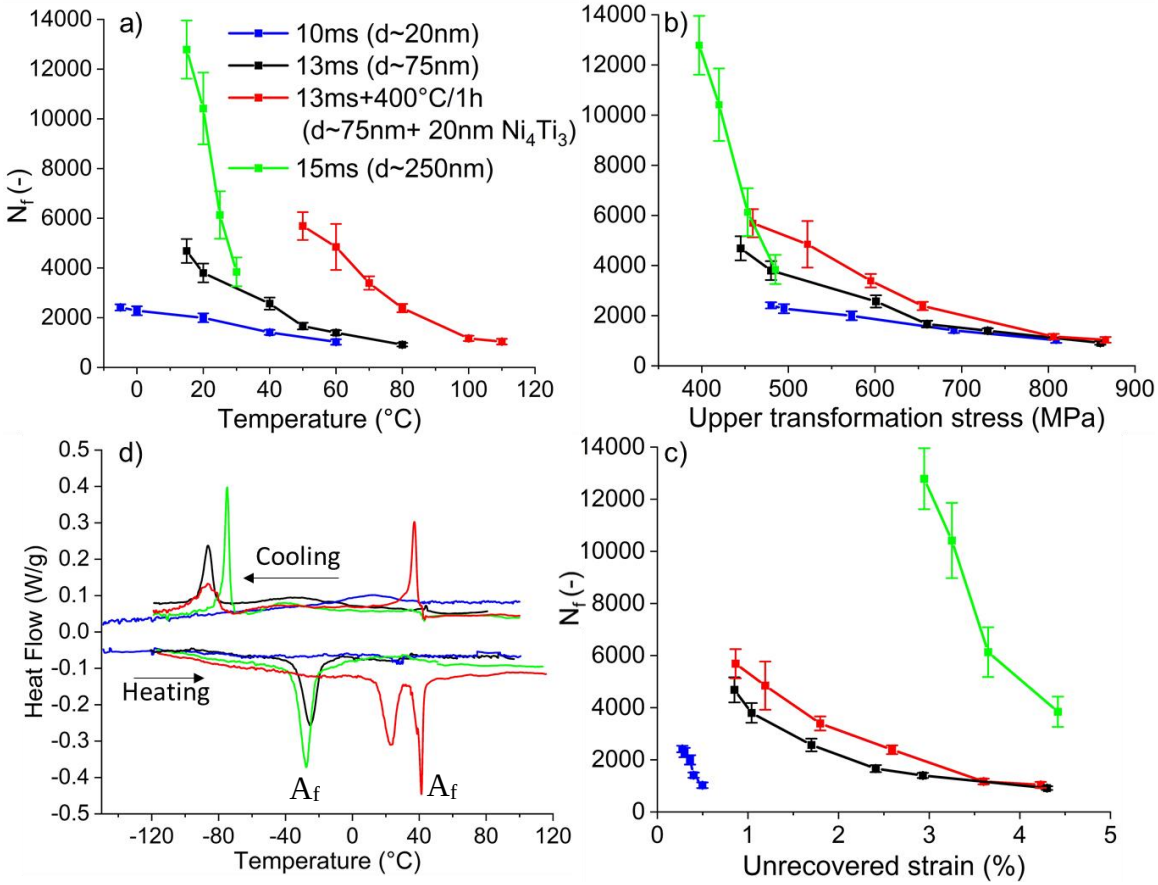

Fig 33. The fatigue life of various NiTi wires as a function of: a) temperature (in the perspective of transformation temperatures recorded by DSC (d)), b) upper plateau stress and c) unrecovered strain.

However, the conclusion appears to be different when we start to compare the fatigue life of individual wires. The 15 ms wire displaying the highest cyclic instability exhibits the highest (structural) fatigue life (N_f ~ 12 000 cycles at 15 °C) though in the narrow temperature range only. In contrast, the functionally stable 10 ms wire exhibits the lowest fatigue life (N_f < 2 500 cycles) in the wide range of temperatures and stresses. The 13 ms microstructure shows a moderate fatigue life (N_f ~ 4 000 cycles at room temperature) in a similarly wide temperature range. The aging of the 13 ms wire enables superelastic testing at the highest temperatures and slightly improves fatigue life. Similar trends can be seen in Fig. 33a,b since the transformation stress and temperature are coupled.

The upper plateau stress increasing from 400 MPa to nearly 900 MPa with increasing temperature is definitely an important factor for functional fatigue as well as for structural fatigue. However, the slopes of curves in Fig. 33 are important, too. The 15 ms wire with the largest grain size especially stands out in this perspective. As the fatigue studies reported in the literature were rarely performed using a range of microstructures and test temperatures at the same time, this is quite often overlooked. Considering NiTi wires having various virgin microstructures, the conclusion of the effect of plastic deformation on the fatigue life is

suddenly very different. A small unrecovered strain does not automatically imply better fatigue life. On the contrary, the least stable 15 ms wire shows the highest fatigue life. Since we believe that this originates from the evolution of microstructure during tensile cycling and its effect on a crack propagation rate, we analyzed the microstructures in cyclically deformed wires by TEM and studied fracture surfaces by SEM to obtain direct experimental information.

Table 1
Overview of the performed fatigue tests indicating grain size after heat treatment and fatigue life at a given temperature and upper plateau stress σ_p^{up}.

Heat treatment		160Wmm^{-3}/10ms		160Wmm^{-3}/13ms		160Wmm^{-3}/13ms + 400°C/1h		160Wmm^{-3}/15ms	
Grain size (nm)		20		75		75 (+ 20nm Ni_4Ti_3)		250	
		N_f (-)	σ_p^{up} (MPa)	N_f (-)	σ_p^{up} (MPa)	N_f (-)	σ_p^{up} (MPa)	N_f (-)	σ_p^{up} (MPa)
Temperature of fatigue tests (°C)	-5	2415	480						
	0	2280	495						
	15			4685	445			12785	397
	20	1997	573	3800	480			10416	420
	25							6131	453
	30							3844	485
	40	1412	691	2570	601				
	50			1665	660	5690	459		
	60	1025	809	1400	730	4847	522		
	70					3395	595		
	80			915	860	2388	655		
	100					1167	807		
	110					1038	866		

4.3 Characterization of lattice defects in deformed NiTi wires

4.3.1 Fatigue fracture surfaces and nonmetallic inclusions

Fatigue fracture surfaces (FFS) of the tested wires were observed in SEM with the aim to find out whether the applied heat treatment and testing conditions affect fatigue crack propagation. Figs. 34-37 document fracture surfaces of the tested microstructures at 'low' and 'high' temperatures of the temperature window shown in Fig. 33. Fig. 34a shows the FFS of the 10 ms NiTi wire cycled at -5 °C. This particular sample shows two nucleation sites of separate fatigue cracks that grow simultaneously and merge before the final fracture. The area of fatigue crack propagation is distinct from the area of the final fracture. The area of fatigue crack propagation consists of river marks and quasi-cleavage fracture surfaces in the vicinity of the nucleation site verging into the fatigue striations zone. The area of the final fracture is characterized by ductile dimples caused by microvoid coalescence nucleating on the matrix/inclusion interface. These fractographic features are common for each sample regardless of their average grain size ranging from 20 nm to 250 nm. The only ratio of crack propagation/final fracture area slightly differs probably depending on transformation stress and temperature of fatigue tests.

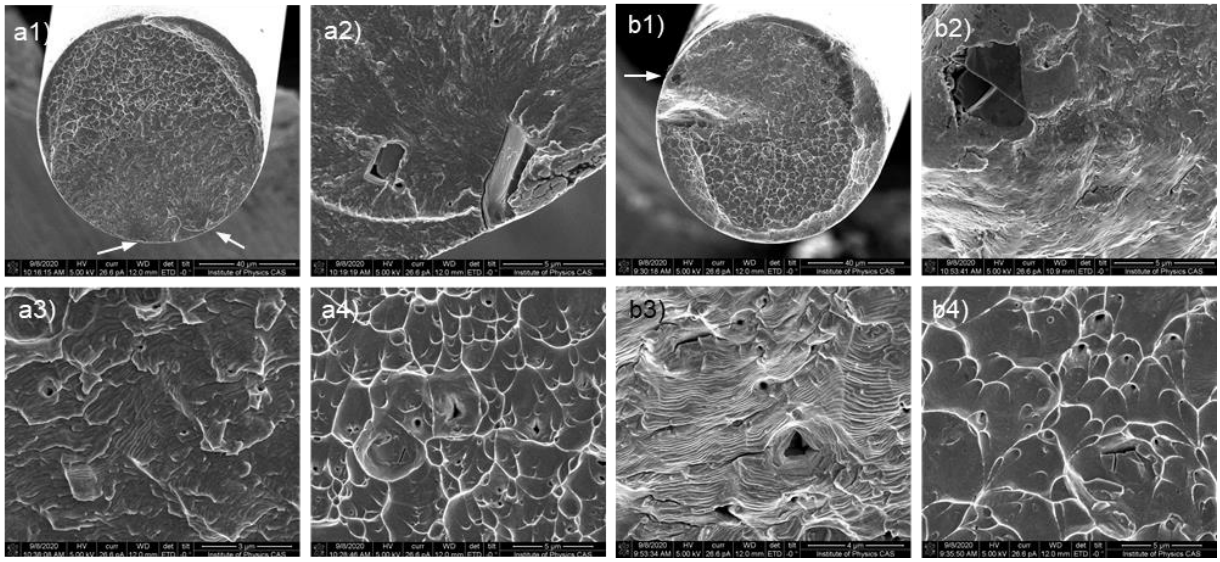

Fig. 34. Fatigue fracture surface of the 10 ms sample tested at a) -5 °C (N_f = 2550 cycles) and b) 60 °C (N_f = 890 cycles). 1) overview of the whole fracture surface, arrows indicate nucleation site of fatigue cracks), 2) detail of the nucleation site of the fatigue crack, 3) striation field and 4) detail of ductile dimples in the region of final fracture.

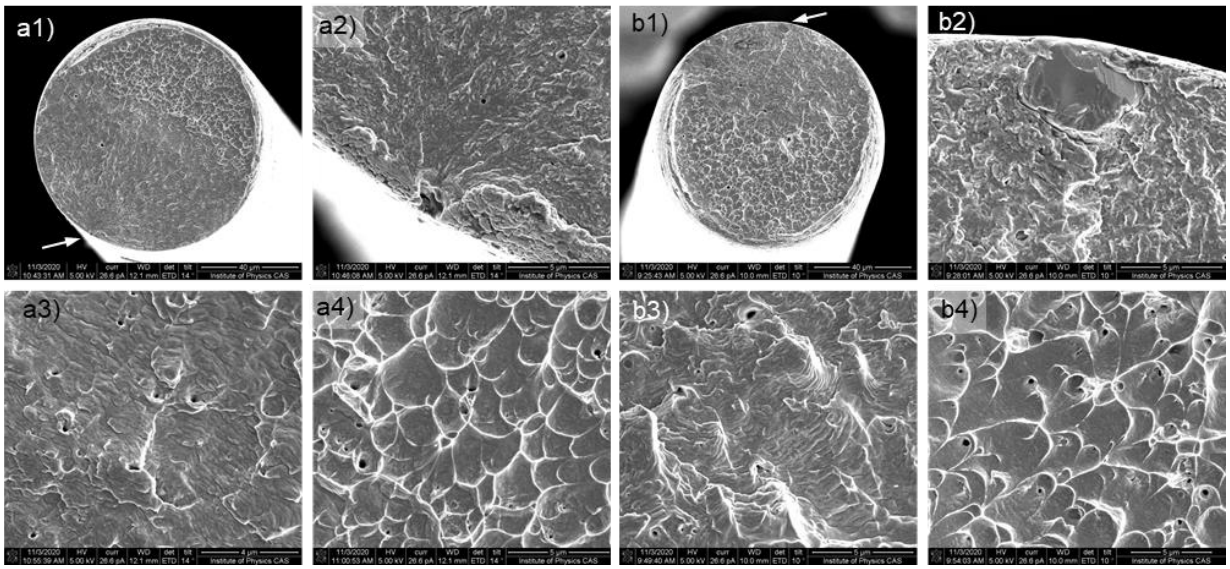

Fig. 35. Fatigue fracture surface of the 13 ms sample tested at a) 15 °C (N_f = 4850 cycles) and b) 60 °C (N_f = 1420 cycles). 1) overview of the whole fracture surface, arrows indicate nucleation site of fatigue cracks), 2) detail of the nucleation site of the fatigue crack, 3) striation field and 4) detail of ductile dimples in the region of final fracture.

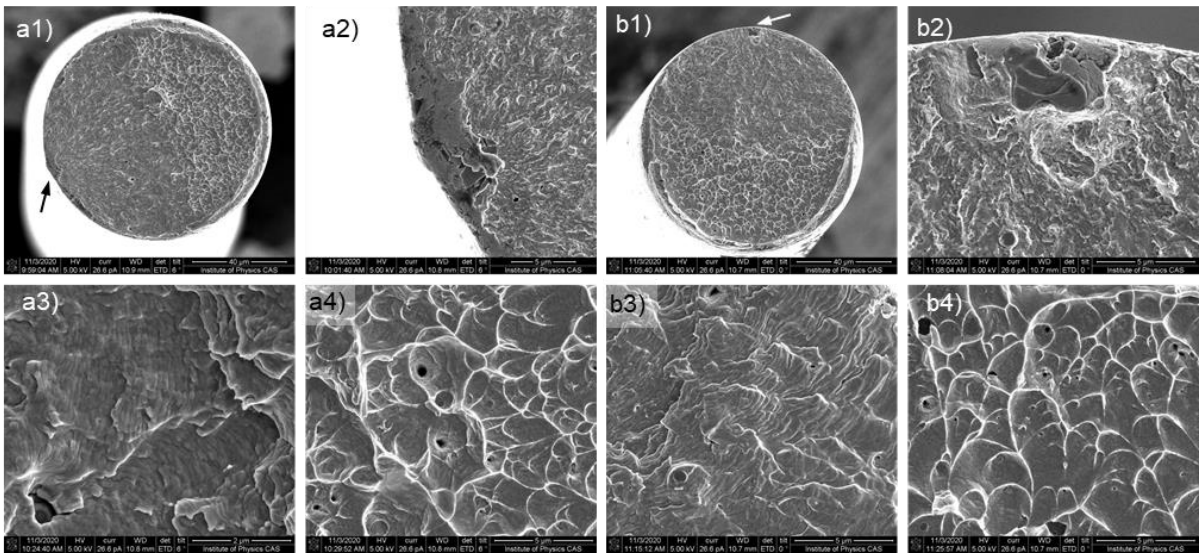

Fig. 36. Fatigue fracture surface of the 13 ms+400°C/1h sample tested at a) 50 °C (N_f = 5460 cycles) and b) 110 °C (N_f = 1010 cycles). 1) overview of the whole fracture surface, arrows indicate nucleation site of fatigue cracks), 2) detail of the nucleation site of the fatigue crack, 3) striation field and 4) detail of ductile dimples in the region of final fracture.

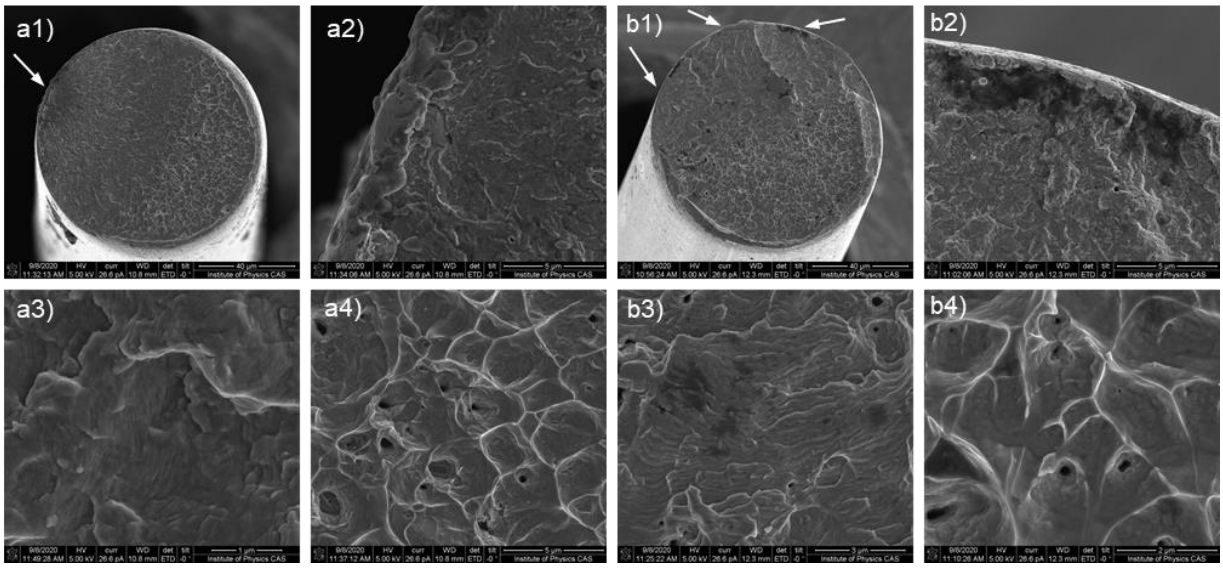

Fig. 37. Fatigue fracture surface of the 15 ms sample tested at a) 15 °C (N_f = 12700 cycles) and b) 30 °C (N_f = 3800 cycles). 1) overview of the whole fracture surface, arrows indicate nucleation site of fatigue cracks, 2) detail of the nucleation site of the fatigue crack, 3) striation field and 4) detail of ductile dimples in the region of final fracture.

The tested samples commonly contain inclusions, which are mainly titanium carbide particles (the elements detected by EELS are titanium, carbon, and trace amount of oxygen). The STEM image in Fig. 38a shows 1 µm TiC inclusion embedded in a NiTi matrix with 75 nm grain size and the SEM image (Fig. 38b) illustrates damage (longitudinal cracks) around 1.6 µm TiC inclusion in the 15 ms sample. The average size of TiC inclusions is approx. 0.8 µm, but the largest particles can exceed 3 µm (see Figs. 35b2 and 36b2). The fatigue cracks nucleated at the inclusions on the surface. These inclusions can be directly seen on the nucleation site, or a cavity is left in its original position (Fig. 35a2). These inclusions are quite common and up to 3 nucleation sites were detected on a single fracture surface (Fig. 37b1). As these inclusions are created during the solidification process of a molten NiTi containing carbon [121], the applied

heat treatment after cold-working does not change the size or distribution of the inclusions. Thus, the ductile dimples created in the area of final rupture exhibit nearly the same morphology.

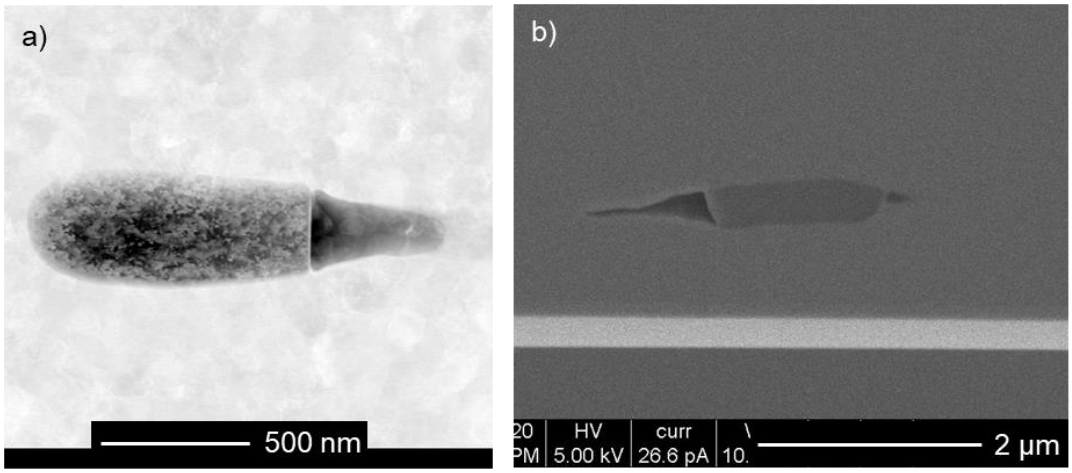

Fig. 38. Examples of TiC inclusions embedded in NiTi matrix: a) STEM image of the 13 ms+400°C/1h sample and b) SEM image of the 15 ms wire.

Although the FFS are not significantly affected by the applied heat treatment and resulting morphology is shaped mainly by the presence of TiC inclusions, the comparison of striations fields in Fig. 39 indicates some degree of difference in the fatigue crack propagation. All micrographs in Fig. 39 were taken approx. 35±5 µm from the crack nucleation site. The fatigue striations are wider and more pronounced on fracture surfaces from tests at 'higher' temperatures. A similar trend can be seen in the comparison of different microstructures. Together with fatigue life (the caption states particularly N_f of the observed samples), these fractographic features indicate higher stress intensity factor (K factor) and higher fatigue crack propagation rate in samples with smaller grain size tested at higher temperatures. However, higher degree analysis of fatigue crack propagation is beyond the focus of presented fatigue tests.

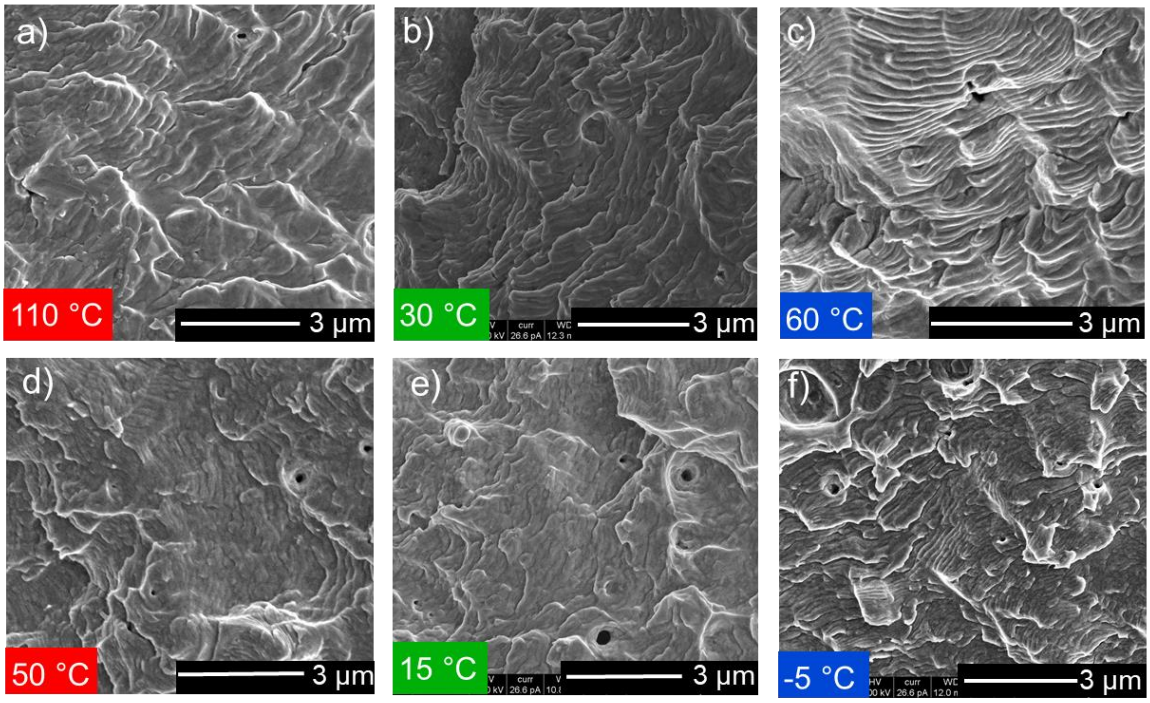

Fig. 39. Comparison of the fatigue fracture surface of tested NiTi wires formed during 'high temperature' fatigue tests on a) 13ms+400°C/1h (N_f = 1010 cycles at 110 °C), b) 15ms (N_f = 3800 cycles at 30 °C) and c) 10ms (N_f = 890 cycles at 60 °C) wires, and at 'low temperature' fatigue tests on d) 13ms+400°C/1h (N_f = 5400 cycles at 50 °C), e) 15ms (N_f = 12300 cycles at 15 °C) and f) 10ms (N_f = 2450 cycles at -5 °C) wires, respectively. The micrographs were taken approx. 35±5 µm from the crack nucleation site.

4.3.2 Evolution of microstructure during fatigue tests

As the stress-induced martensitic transformation in superelastically cycled NiTi is accompanied by plastic deformation processes [33][38][39][40][41][42], lattice defects are generated upon cycling, accumulate, and gradually change the virgin microstructure. Whether it takes place and how much the microstructure changes, depends on the virgin microstructure and test temperature [86]. Fig. 40a-c shows the completely recrystallized microstructure of the virgin 15 ms wire with a negligible density of lattice defects. This microstructure changes differently upon tensile cycling at different temperatures. After the fatigue test at 15 °C (Fig. 40d-f), the microstructure contains a high density of slip dislocations and only a few deformation bands, mainly in smaller grains (Fig. 40f). On the contrary, the microstructure of wire fatigued at 30 °C exhibits a large number of deformation bands, which frequently extend across multiple grains (Fig. 40g-i). The dislocation density does not significantly increase compared to the sample tested at 15 °C. This demonstrates that, although the virgin microstructures of the wires were the same, fatigue cracks propagated through different microstructures depending on temperature.

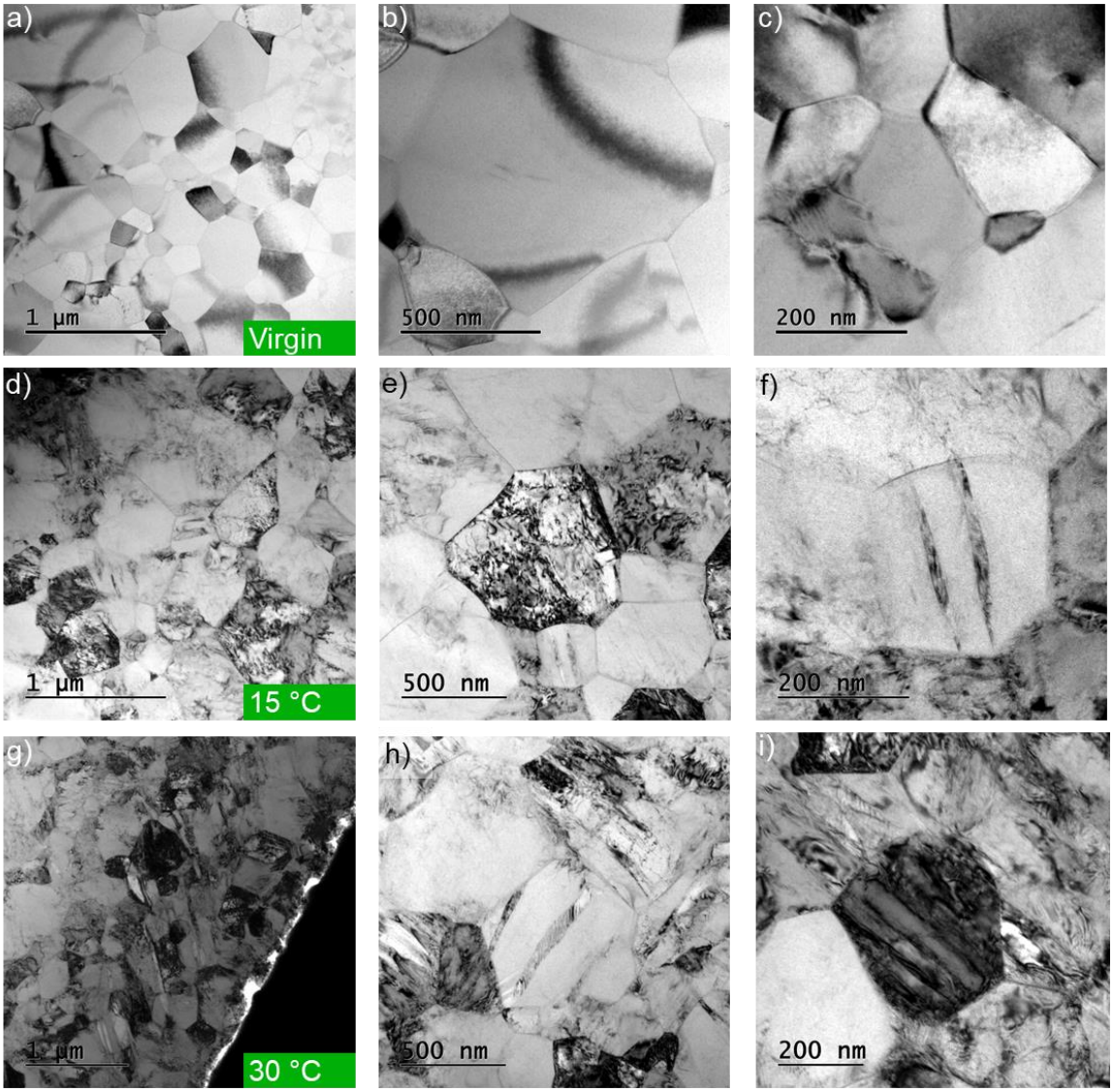

Fig. 40. TEM micrographs showing virgin microstructure of the 15 ms NiTi wire (a-c), after fatigue tests at 15 °C (N_f = 12300 cycles) (d-f), and at 30 °C (N_f = 3900 cycles) (g-i).

However, as the material deforms differently ahead of the propagating crack and in the bulk [103], we wanted to see the microstructure through which the fatigue crack actually propagated. Hence, we extracted TEM lamellae from the fatigue fracture surface of the 15 ms wires tested at 15 °C and 30 °C (Fig. 41). Both lamellae were extracted approx. 20-25 µm from the crack nucleation site so that the wire axis lies in the lamella plane (Fig. 42). Compared to the microstructures in lamellae extracted from elsewhere in the bulk (Fig. 40), the microstructures observed in Fig. 41 contain a significantly higher amount of deformation bands. Nevertheless, there are differences between microstructures created at 15 °C and 30 °C temperatures as well. The microstructure of the wire cycled at 15 °C contains mainly short deformation bands, even in the grains bisected by a propagating fatigue crack (see Fig. 41b,d), whereas the microstructure of the wire cycled at 30 °C contains long deformation bands spreading deeper across multiple grains throughout the majority of the crack path (Fig. 41f-h). The crack propagates mainly transgranularly (Fig. 41b,c), as observed also by other authors [113]. Both samples show a higher density of deformation bands in the areas of sharp change in crack propagation direction (Fig. 41c,g), which is more pronounced in the sample cycled at higher temperature again. It is thus confirmed that the fatigue cracks indeed propagate through

different microstructures in tests at 15 °C and 30 °C and the stress concentration at the fatigue crack tip significantly contributes to the microstructure evolution.

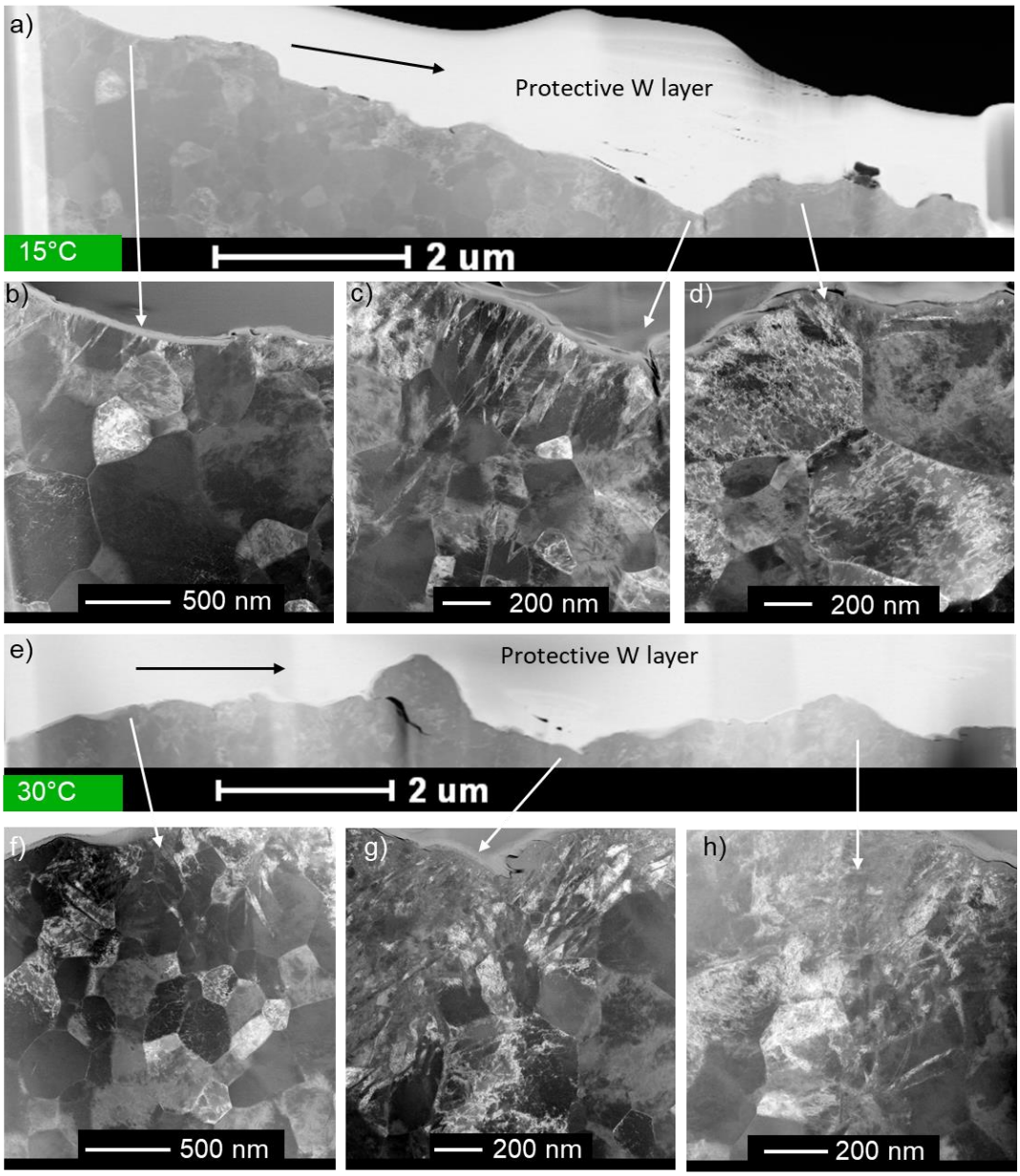

Fig. 41. TEM micrographs showing the near fatigue crack microstructure of the 15 ms NiTi wire after the fatigue test at 15 °C (a-d) and at 30 °C (e-h). TEM lamellae were cut perpendicularly to the wire cross-section and black arrows indicate propagation of the fatigue cracks. The fatigue crack is covered by a protective tungsten (W) layer during the process of lamella preparation.

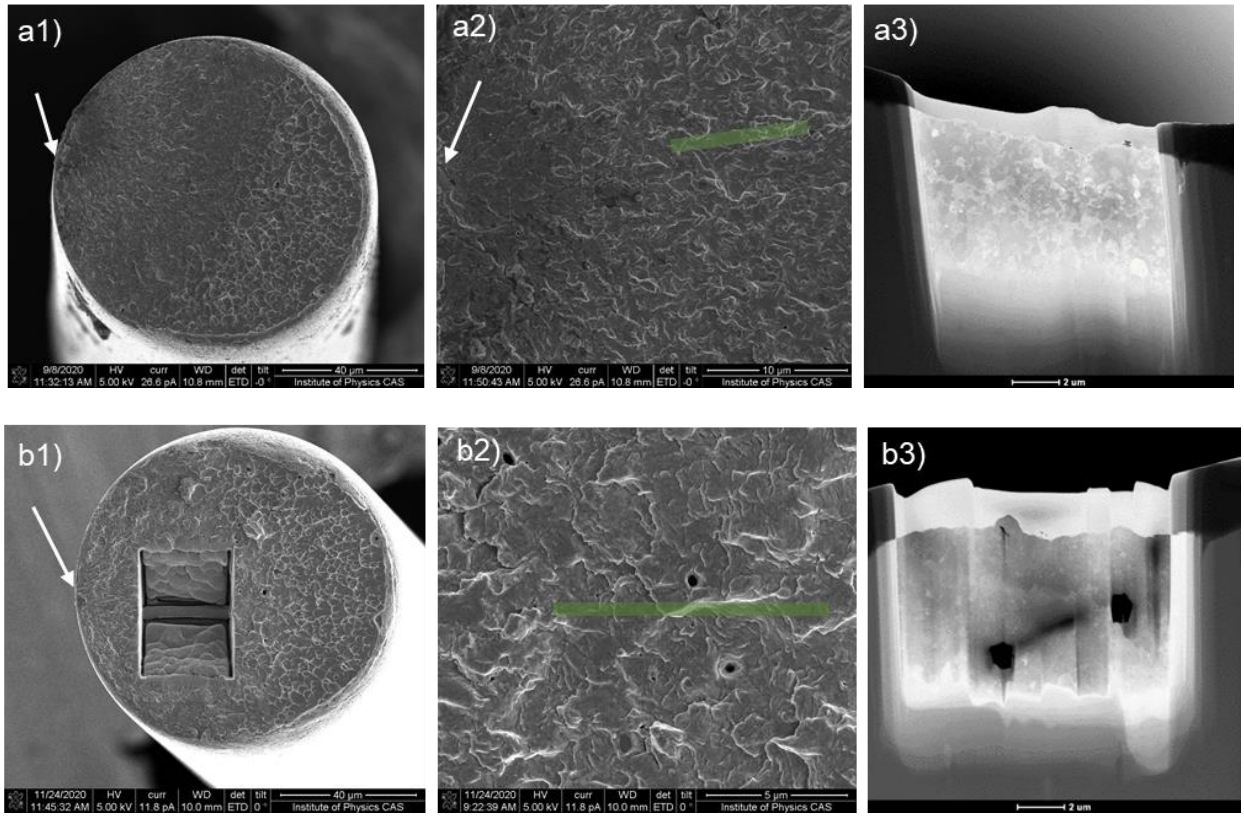

Fig. 42. Extraction of TEM lamellae from fatigue fracture surface of wires tested at a) 15 °C and b) 30°C. White arrows indicate the position of the crack nucleation site and green rectangles show the position of TEM lamella before FIB extraction.

4.3.3 Short cracks at the wire surface

The surface of the tested wires was observed by TEM as well, as surface finish treatment can significantly affect the results of fatigue tests. It was found that the surface is covered by an approx. 50 nm thick oxide layer of TiO_2 (Fig. 43 - the darker layer between NiTi matrix and tungsten protective coating applied during lamella preparation process). The wire was not subjected to any kind of polishing. Therefore, all samples exhibit higher surface roughness and contain pre-existing notches that can be up to 200 nm deep, probably created during the cold-working process. However, the thickness of the TiO_2 layer and surface roughness are unaffected by the applied heat treatment methods.

Short cracks (<100 nm) were observed after only 10 loading cycles in both superelastic (Fig. 43) and actuation regimes (Fig. 44). These cracks nucleate preferentially in the area of stress concentration (Fig. 43b). Moreover, deformation twinning and increased density of dislocations were observed around the crack as well. Despite the high density of those small cracks underneath the surface, the terminal fatigue cracks always nucleated at TiC inclusions.

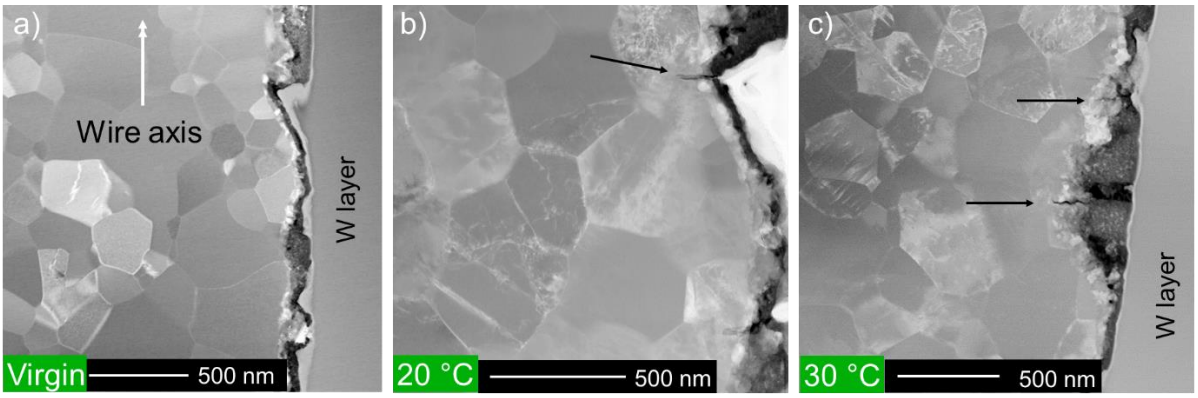

Fig. 43. STEM micrographs showing microstructure underneath the 15 ms wire surface in a) virgin wire, b) after 10 superelastic cycles at 20 °C and c) after 10 cycles at 30 °C. A dark surface oxide layer is covered by a bright Tungsten cover layer applied while preparing the TEM lamella. Small cracks in the NiTi (black arrows) appear at stress risers already after 10 cycles.

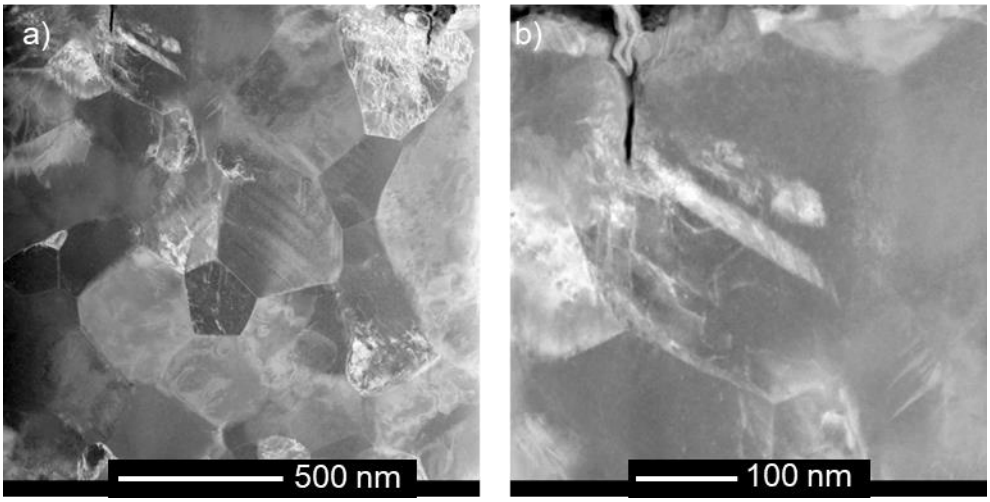

Fig. 44. STEM micrographs of the 15 ms wire subjected to 10 thermal cycles at a constant stress of 400 MPa. a) Overview of a subsurface microstructure with two surface cracks created during the thermal cycling and b) detail of the surface with deformation band nucleated at the crack tip.

5 Discussion

5.1 Effect of Heat Treatment on Functional Properties

Four different heat treatments were applied to the cold worked superelastic NiTi wire to explore the effect of microstructure on functional and structural fatigue. Heat treatments by 10 ms, 13 ms, and 15 ms pulses of electric power resulted in microstructures characterized by the average grain size of 20 nm, 75 nm, and 250 nm, respectively. The applied heat treatments adjusted the microstructure and functional properties of the NiTi wire as shown in Figs. 3-7.

The additional aging of the 13 ms wire at 400 °C for 1h created approx. 20 nm long Ni-rich Ni_4Ti_3 precipitates in the microstructure but did not affect the grain size. Aging is more effective in lowering the upper plateau stress σ_p^{up} than heat treatment from the 10 ms to the 15 ms microstructure. Simultaneously, the aging shifts the R-phase transformation to higher temperatures and increases yield stress σ_y, which improves the cyclic stability of the stress-strain response. However, the aging could also be disadvantageous in some applications, as the upper plateau strain ε_p^{up} is reduced from 6.7 % to nearly 5 % and the A_f temperature increases up to 44 °C (Fig. 3b).

In order to select a suitable temperature range for fatigue experiments, superelastic tensile tests were performed in the temperature range from -30 °C to 190 °C (Figs. 5-7). Although all tested samples show stable stress-strain-temperature curves at room temperature (less than 0.1% unrecovered strain is measured in a single closed-loop cycle), the stress-strain response of the 15 ms wire is considerably less stable at elevated temperatures (reaches 1% ε_{us} at only 40 °C while the 10 ms wire reaches that at ~ 140 °C). The 13 ms sample without and with the aging reaches 1% ε_{us} at 80 °C and 110 °C, respectively. The instability of cyclic stress-strain response of wires with different microstructures had to be considered when designing the fatigue experiments. Moreover, the decrease in σ_p^{up} by approx. 200 MPa always occurs regardless of the virgin microstructure or low accumulation of ε_{us} (Figs. 28-31).

5.2 Lattice Defects Generated by Cyclic Thermomechanical Loading

Based on the presented results (Figs. 8-16) it appears that plastic deformation occurs (unrecovered strains and permanent lattice defects are generated) during the thermomechanical cycling of NiTi wire only if the martensitic transformation proceeds under elevated external stress (i.e. not when the wire transforms under low stress, when it is deformed in the low-temperature martensite state or when it is loaded elastically to very high stresses at high temperatures in the austenite state). This is the key result of this work. Concerning the unrecovered strain, this was the main conclusion of our previous work [34] but very little was known about the permanent lattice defects. Of course, this conclusion applies only for NiTi wires deformed within the transformation range. If the wire is deformed plastically beyond the crystallographic limits of the B2-B19' transformation, plastic deformation proceeds within the martensite phase, and lattice defects created in the martensite are inherited into the austenitic microstructure upon the reverse martensitic transformation (Figs. 17-19) [19][122].

With respect to our earlier experiments in [34] on the 13 ms wires (Figs. 15,16), the thermomechanical loading experiments on the 15 ms wires (Fig. 8-14) were performed with

three important innovations: 1) the experiments were performed on recrystallized NiTi wire with suitable grain size so that permanent lattice defects created in the virgin austenitic microstructure upon cycling can be better observed and analyzed, 2) the type of experiments were carefully selected to cover the whole range of stress and temperature conditions at which the martensitic transformations may proceed in real applications, and 3) 10 thermomechanical cycles were performed instead of one cycle only (this is important since deformation bands are promoted by cycling). These tests also better represent damage sustained during fatigue life.

5.2.1 Stable functional responses

Considering that unrecovered strains are generated only if martensitic transformation proceeds under elevated external stress, questions appear whether this wire can be used in thermomechanical loading tests without generating unrecovered strains and lattice defects. We have reported that marginal unrecovered strains and only very few permanent lattice defects were generated in cyclic thermomechanical loading tests in which:

- martensitic transformation proceeded under very small stress (Fig. 8a,9a),
- no transformation proceeded under stress in the cyclic shape memory regime (Fig. 10),
- the transformation proceeded only marginally upon thermal cycling in the cyclic recovery stress regime (Fig. 11).

The observed stress-strain-temperature responses in all these tests were found to be very stable, despite the large stresses, strains, and temperatures applied in some of these tests. This observation is very important since it contradicts the results of many literature reports, in which massive dislocation generation in transforming NiTi was observed upon stress-free thermal cycling [115], martensite reorientation by deformation [123][124], or martensitic transformation under low stress [35][96].

The problem is that the NiTi alloys used in these experiments were frequently either solution-treated or annealed alloys, which were simply too soft to show functional behavior. The solution-treated NiTi single crystals and polycrystals show different properties from the nanocrystalline NiTi wires studied in this work. The two most important differences are that i) the solution-treated alloys have very low yield stress for plastic deformation and ii) martensitic transformation upon stress-free cycling proceeds via propagation of habit plane interphases between B2 austenite and type II twinned martensite interfaces [49]. In contrast, the NiTi wires with nanocrystalline microstructure are highly resistant to plastic deformation in martensite [34] and the microstructure of thermally induced martensite is formed by (001) compound twins [125][126][127].

The results of the above-mentioned tests (Fig. 8a, 9a, 10, 11) clearly show that martensitic transformation may proceed in thermomechanically cycled nanocrystalline NiTi wire without generating unrecovered strains and permanent lattice defects observable by conventional TEM. This allows for stable stress-strain-temperature responses in thermomechanical loading tests under specific conditions. High cycle thermomechanical loading tests to determine the functional and structural fatigue of such wires remain to be performed.

5.2.2 Permanent lattice defects

Since the martensitic transformation, in theory, does not leave behind any lattice defects, the permanent lattice defects observed in the microstructure of deformed wires are considered to be relics of the plastic deformation processes that potentially accompanied the cyclic martensitic transformation during the closed-loop cycling. In other words, if an incremental plastic deformation occurred within the cycled wire, we shall evaluate unrecovered strain, and we might observe permanent lattice defects in the austenitic microstructure of the cycled wire. If it did not occur, we shall see no unrecovered strains and shall not find any new permanent lattice defects in the microstructure of cycled wires.

We have performed 10 thermomechanical loading cycles to increase the probability that the observed type and density of lattice defects are statistically representative for the martensitic transformation taking place under given stress/temperature conditions. To provide the reader with relevant experimental information on the observed defects, we used STEM mode, in which dislocation defects, austenite twins, and deformation bands are better highlighted in a large number of variously oriented grains within one micrograph and in which the disrupting contrast on bending contours is suppressed. For a detailed investigation of individual lattice defects, particularly slip dislocations [35], residual martensite bands [42], and austenite twins [86], see our related papers.

The permanent lattice defects observed by TEM in the microstructure of NiTi wires subjected to 10 thermomechanical loading cycles are:

- **dislocation loops and isolated dislocation segments** observed in tests, in which martensitic transformation proceeds at very low stresses and temperatures (Fig. 8a, 9a, 10)
- **(110)/<001> slip dislocations** at intermediate stresses and temperatures (Fig. 8b, 9b, 11, 12, 13b)
- **deformation bands** typically containing {114} austenite twins with a high density of unidentified slip dislocations both inside the twins and surrounding matrix at high stresses and temperatures (Fig. 8c,9c,12,13a,c).

The type of the observed permanent lattice defects depends mainly on the stresses/temperatures, at which the forward and/or reverse martensitic transformation proceeded in the test. This will be further discussed in section 5.2.3 (Effect of temperature/stress at which the forward and reverse martensitic transformation takes place).

Isolated dislocation loops and segments were observed in the austenitic microstructure after thermal cycling under the lowest stresses of 6.5 MPa (Fig. 9a). The recorded strain–temperature response was stable and the hysteresis width was about 40 °C. The thermally induced martensite in this nanocrystalline wire is formed by domains of (001) compound twinned B19’ martensite [125] which form via R-phase, reorients upon tensile deformation into a single domain martensite [125], and transforms back into parent austenite upon stress-free heating during the shape memory cycle. Since the forward and reverse martensitic transformations proceed in the absence of stress during the shape memory cycle, very small unrecovered strains and very few permanent lattice defects were generated upon cycling.

The compound twinned martensite in nanograined NiTi was analyzed in detail in a series of articles by Waitz [126][127][128]. He argued that the B2 austenite in nanograined NiTi transforms into single or multiple compound twinned domains of B19' martensite because of energy reasons [128]. Our results [125] show that this is also the case for the 15 ms NiTi wire with a significantly larger mean grain size ~ 250 nm. Anyway, there must exist a mobile interface between the B2 austenite (R-phase) and the B19' martensite, which propagates cyclically under low stress without generating unrecovered strain and lattice defects with ~40 °C hysteresis, which has a potential to operate for a very large number of transformation cycles.

Slightly more dislocation loops and segments were observed in shape memory tests (Fig. 8a - deformation at $M_s < T < A_f$) and (Fig. 10 - deformation at $T < M_s$), in which the reverse transformation of oriented martensite took place upon heating at 20 MPa stress. Compared to the thermal cycling under 6.5 MPa (Fig. 9a), the wire was deformed in the martensite state to a large strain via martensite reorientation. For information on the change of martensitic microstructure upon straining see [125]. It shall be pointed out that, the A_f temperature was shifted 40 °C upwards (Fig. 10b) compared to the thermal cycle (Fig. 9a), and yet practically no lattice defects were created upon cycling in the microstructure and the stress-strain-temperature response was remarkably stable. This upward shift of the A_f temperature (martensite stabilization) is caused by the deformation in martensite but not with lattice defects. It is thus evident that the martensite stabilization by deformation does not involve any plastic deformation and cannot be ascribed to slip dislocations, as frequently argued in the literature [129]. It is solely due to the additional energy required to form strain-compatible austenite/martensite interfaces on the grain scale within the deformed martensitic microstructure before the reverse transformation takes place on heating [34][125]. This martensite stabilization by deformation is the reason why the reverse transformation line in the σ-T diagram never coincides with the A_f temperature determined from the stress-free DSC or electric resistivity tests on thermally cycled NiTi wires.

(110)/<001> slip dislocations were systematically observed in all tests, in which martensitic transformation proceeded at elevated stresses (Figs. 8b, 9b, 11, 12, 13b). There are basically two types of slip dislocations observed in the microstructure of cycled wires (Fig. 14)– individual slip dislocations segments, while the recorded accumulated unrecovered strains were relatively low (< 2 %), and dense dislocation fields within deformation bands left in the microstructure of NiTi wire subjected to highest stresses and temperatures in thermomechanical loading tests, while the recorded unrecovered strains were typically large (> 2 %). These dislocations were analyzed and ascribed to the {011}<100> austenite slip system in our work [35]. The dense dislocation fields in deformation bands were observed in the tests at high stresses and temperatures (Fig. 8c, 9c, 13c). We assume that these dislocations originate from the dislocation slip on the (001) plane in the B19' martensite lattice (lattice correspondent plane to the {011} austenite plane) and are inherited by the austenite during the reverse martensitic transformation [125].

There are various theoretical predictions in the literature for the origin of the slip dislocation generated by superelastic cycling [34][38][115][130][131][132]. Several authors claim that the {011}<100> austenite slip dislocations are generated at the propagating habit plane interface at the cross-section between the habit planes and type-II twins inside the martensite. Since type-II twins were never observed in stress-induced martensite in nanocrystalline NiTi [125], these

predictions do not fit our experiments. However, they may still work for NiTi single crystals and solution-treated NiTi. We have proposed earlier [34][38] that slip dislocations form mainly during the reverse martensitic transformation behind the propagating habit plane interface by the slip in the austenite phase, facilitating strain compatibility at the habit plane. This proposition has to be revised as well since Fig. 12 clearly shows that {011}<100> slip dislocations are generated during both forward and reverse transformations. An alternative plausible explanation would be that the observed slip dislocations simply form by the activation of the {011}<100> slip in the austenite matrix due to stress concentrations during the martensitic transformation. Interestingly, the individual {011}<100> dislocations appear mainly in large grains (Figs. 8b, 9b), while isolated single deformation bands are more frequently observed in small grains (Figs. 12b2, 40e,f). This most likely originates from different stress states in small and large grains of the transforming polycrystal. Further theoretical and experimental research is currently in progress to reveal the mechanism by which the slip dislocations actually form during the thermomechanical cycling of nanograined NiTi.

In summary, individual {011}<100> slip dislocations were observed in the microstructure of NiTi wire superelastically or thermally cycled at intermediate stresses, while the recorded accumulated unrecovered strains were relatively low (~ 2%). The dense dislocation fields, alternatively, were observed within the isolated deformation bands left in the microstructure of the NiTi wire subjected to the highest stresses and temperatures in thermomechanical loading tests while the recorded accumulated unrecovered strains were typically very large (> 5 %).

Deformation bands were commonly observed in tests, in which martensitic transformation proceeded at high stresses (Figs. 8c, 9c, 12, 13a,c). The unrecovered strains recorded in these tests were typically very large (> 2 %). In our opinion, the deformation mechanism leading to the creation of deformation bands (and large unrecovered strains) has its origin in the plastic deformation of the oriented B19' martensite phase by (100) deformation twinning [42][125] and/or kwinking [44] occurring selectively in polycrystal grains experiencing high stresses during the thermomechanical loading tests.

Recent TEM analyses of stress-induced martensite in deformed NiTi reported in the literature [42][125][134][135] suggest that the stress-induced B19' martensite in nanocrystalline NiTi wires is not formed by <011> type II twinned martensite plates but (001) compound twinned single domains of the B19' phase [125]. It is claimed in [125] that the dislocation slip on the (001) plane in the B19' martensite lattice is likely to occur at elevated stresses. Sittner et al. [42] identified the interfaces separating the B19' deformation bands from the B2 austenite matrix in the residual martensite observed in a very similar 16 ms NiTi wire subjected to two superelastic cycles as the $(-21-1)_{B2}//(10-1)_{B19'}$ interfaces. Two martensite variants forming the $(20-1)_{B19'}$ deformation twin in Fig. 2 in Ref. [92] are separated from the surrounding austenite matrix by the same interface. Casalena et al. [133] recently observed this interface in the microstructure of NiTiHf alloy subjected to 10 superelastic cycles at room temperature. Although these interfaces are not strain compatible and shall not exist in NiTi from the theoretical point of view [49], they were regularly observed experimentally in deformed NiTi alloys. We suspect that (100) deformation twinning in overstressed B19' martensite is responsible for the initiation of martensite bands [42][125] upon cyclic superelastic loading (Fig. 12) and actuator cycling (Fig. 13).

The microstructure observed in some tests (Fig. 9c), however, contains a very large density of deformation bands and very large unrecovered strains introduced by the kwinking deformation [44]. The kwinking (combination of deformation twinning and dislocation-based kinking in the B19' martensite) was claimed to be responsible for the onset of plastic yielding of martensite [125]. It gives rise to the deformation bands containing {114} austenite twins in the microstructure of the wire observed by TEM after unloading and heating above A_f temperature [40][42]. We originally treated the deformation mechanism leading to the creation of deformation bands as deformation twinning in the B19' martensite followed by reverse transformation of the crystal within the band to the austenite twin [40][42], but there is a high density of slip dislocations within the deformation bands (e.g. Figs. 12a2) as well as in the surrounding austenite matrix (Fig. 9c), which needs to be taken into account. Later on, we realized that this localized deformation involves a combination of deformation twinning and dislocation-based kinking, called kwinking in [44]. Since the kwinking deformation takes place, when the material is loaded in the martensite phase, it can take place during the forward and/or reverse transformation, whenever the stress acting on the B19' martensite locally increases in thermomechanical loading tests.

As introduced in [44], kwinking deformation leads to mesoscopically localized plastic deformation of the stress-induced martensite. It may occur during the forward loading (or cooling under large stress), during loading in martensite state, or during the reverse transformation upon reverse unloading (or heating under large stress). In fact, the results of the bypass experiments seem to suggest that deformation bands tend to appear preferentially during the reverse transformation on unloading and heating. Hence, unrecovered strain and deformation bands accumulate upon thermomechanical cycling involving heating under large stress (Fig. 12c). In the case of reverse martensitic transformation proceeding under very large temperature/stress (Fig. 9c), the wire almost did not shorten upon heating under 750 MPa stress. The detailed mechanism of the kwinking deformation accompanying the cyclic martensitic transformation remains to be investigated both experimentally and theoretically. It was observed that the martensite lattice within the deformation band transforms to the {114} austenite twins upon the constrained heating to high temperatures [38][42][125]. The austenite phase is, thus, completely restored during the reverse transformation upon heating but large unrecovered strain remains. Reverse martensitic transformation upon heating proceeding into austenite twins within the deformation bands [38][39][42] is considered to play a key role in this.

In summary, the deformation bands observed in the microstructure of NiTi wire subjected to thermomechanical cycling at high temperatures/stresses correlate with very large unrecovered strains recorded in these tests. The deformation mechanism by which the deformation bands are created is related to the (100) deformation twinning [42][125] and/or kwinking deformation [44][125] in oriented B19' martensite.

5.2.3 Effect of temperature/stress at which the martensitic transformation takes place

The results of superelastic (Fig. 8) and actuation/thermal (Fig. 9) tests provide clear evidence that the amount of unrecovered strains and permanent lattice defects recorded after 10 closed-loop cycles dramatically increases with increasing temperature and stress, at which the

martensitic transformation proceeds. Concerning unrecovered strains, we already knew that from the work [34]. New information brought in by the present experiments is that the type and density of lattice defects vary with increasing temperature and stress as well.

The conventional superelastic and thermal cycles, in which martensitic transformation proceeded at intermediate stresses (Fig. 8b, 9b), show that the observed unrecovered strains and lattice defects are comparable in superelastic cycling and thermal cycling if they take place at comparable temperatures/stresses. The problem is that the forward and reverse transformation proceed at different temperatures/stresses (Fig. 14) and analysis of unrecovered strains and lattice defects from the conventional tests is impossible. We knew from the results of [34] that the amount of unrecovered strain generated in a single thermomechanical cycle on NiTi wire can be evaluated separately for the forward and reverse transformation by employing bypass tests. This bypass test analysis was applied to cyclic superelastic loading tests (Fig. 11) and actuation/thermal tests (Fig. 12) to determine unrecovered strains and permanent lattice defects created by the cyclic forward and reverse transformations, separately.

Let us discuss the results of the cyclic bypass tests with the help of Fig. 14 in which the unrecovered strains and lattice defects, generated by martensitic transformation proceeding at denoted temperature and stress conditions, are presented. The 3D ε_{us}-σ-T diagram in Fig. 14 shows unrecovered strains accumulated in 10 thermomechanical loading bypass cycles, in which forward or reverse martensitic transformation proceeded at temperature/stresses denoted by the transformation lines in stress-temperature space. The diagram is just a sketch (adopted from [34]) reflecting the experimental data.

The upper plateau transformation stress is generally considered in the SMA field to be relevant for estimating functional fatigue of NiTi wires. In this respect, it is somehow surprising to learn that roughly equal unrecovered strains (and permanent lattice defects) were generated during the forward and reverse martensitic transformations in the superelastic cycling, even if the forward transformation stress is much higher than the reverse one. At the same time, much larger unrecovered strains were generated during the reverse martensitic transformation in the actuation cycle, in which both forward and reverse transformations proceed at equal stresses. This is reflected by the shape of the US curves in the 3D ε_{us}-σ-T diagram (Fig. 14).

The difference in lattice defects generated by the forward and reverse transformation is even more evident in the thermal cycling at constant stress 400 MPa (Fig. 13). The unrecovered strain generated during 10 cycles of forward transformation under stress was only 0.4 %, while that generated through the reverse transformation was 6.4 %. The permanent lattice defects observed by STEM are very different as well. The plastic deformation upon thermal cycling under stress takes place during the heating and the strain-temperature response upon heating, thus gradually shifts towards lower temperatures during the 10 cycles (Fig. 13a). However, it also depends on the applied stress. The strain-temperature response upon thermal cycling under 280 MPa shifts on both cooling and heating sides, suggesting minor comparable problems during both forward and reverse transformation. In this case, however, no deformation bands were found in the microstructure of the cycled wire. Obviously, these results are of key importance for the design of NiTi actuators.

It is interesting to see that the gradual evolution of stress-strain-temperature response upon cycling (cyclic instability) reflects the accumulation of unrecovered strains and lattice defects by the forward and/or reverse martensitic transformations. In the case of the cyclic superelastic

stress-strain curves, this frequently means that the hysteresis decreases because the forward transformation stress decreases upon cycling (see Fig. 8b). In the case of the strain-temperature response upon thermal cycling under stress, this frequently means that the hysteresis width decreases because of the shift of the strain recovery upon heating to lower temperatures (see Fig. 13a). Nevertheless, it shall be pointed out that superelastic cycling at constant temperature and thermal cycling under constant stress are special cases of general cyclic thermomechanical loading tests which include also cyclic shape memory tests, recovery stress tests, or bypass tests. The 3D ε_{us}-σ-T diagram represents a unique tool enabling the estimation of cyclic instability of NiTi in any general thermomechanical loading test.

The three color ellipses drawn into the 3D ε_{us}-σ-T diagram in Fig. 14 denote [temperature, stress] conditions under which very different unrecovered strains and lattice defects were observed. Lattice defects were discussed in section 5.2.2, 'Permanent lattice defects'. Since the defects could have been partially created by plastic deformation processes in the martensite phase, it would be great to know the martensitic microstructures existing in polycrystal grains in these tests. The reader can find relevant information on the martensitic microstructures in thermomechanical tests on a similar NiTi wire in [125].

Based on the 3D ε_{us}-σ-T diagram we can understand why cyclically stable superelasticity is in fact hardly achievable for the 15 ms NiTi wire but it is relatively easy to achieve stable cyclic strain-temperature responses in thermal cycling under constant stress. In other words, we can understand why commercial NiTi wires can survive millions of thermal cycles under constant stress but only thousands of superelastic cycles. To achieve cyclic stability in thermomechanical cyclic tests on NiTi wires, the temperatures/stresses at which martensitic transformation proceeds have to be kept under some critical values to prevent the generation of unrecovered strains and permanent lattice defects. It shall be pointed out that the 15ms NiTi is a model alloy, on which the permanent lattice defects could be beneficially investigated. The commercial superelastic NiTi wires are much stronger (σ_y > 1300 MPa) and the values of the critical stresses/temperatures are hence higher [34][37].

5.2.4 The effect of virgin austenitic microstructure

It is well known that functional responses of NiTi wires depend on the virgin austenitic microstructure [19]. Although the experiments were performed only on the 15 ms NiTi wire with the optimized microstructure, we would like to briefly discuss the effect of the virgin austenitic microstructure on the stability of cyclic functional behavior of NiTi wires because this is, after all, of great importance for engineering applications of NiTi wires.

We use the term "microstructure" in a general sense covering grain size, dislocations, twins, precipitates, internal stress, and texture of the wire. In the SMA modeling literature, however, the meaning of the term microstructure is frequently reduced to the grain size. In reality, however, excluding NiTi wires with partially recrystallized microstructures having a grain size below 100 nm [134], the superelastic stress-strain response of NiTi is only slightly affected by the grain size, but the cyclic instability of the stress-strain response varies dramatically with the grain size since the yield stress for plastic deformation of martensite decreases with increasing grain size [35][37].

In view of the anticipated impact of the yield stress σ_y for plastic deformation of martensite on the cyclic stability, we have introduced the material parameter YS determined as the yield stress needed to trigger the plastic deformation of martensite in the tensile test. While the parameter decreases only slightly with the increasing test temperature, the transformation stress $\sigma^{F,R}$ increases with increasing temperature at ~6MPa/°C rate as common for NiTi (Fig. 7a) in the superelastic regime. In general, the parameter $\sigma^{F,R}$ denotes both forward and reverse martensitic transformation in both superelastic and actuation regime. Since the generation of unrecovered strains and lattice defects is different during the forward and reverse martensitic transformations (Figs. 14), we propose to use a parameter

$$YT^{F,R}=\|[\sigma^*,T^*]-[\sigma,T]^{F,R}\| \quad (7)$$

$YT^{F,R}$ are actually the distances from the $[\sigma,T]^{F,R}$ states (at which the transformation proceeds) to the critical states $[\sigma^*,T^*]^{F,R}$ (at which the forward (reverse) transformation line meets the yield stress line in the σ-T diagram (Fig. 7a)). The shorter the distance is, the larger the unrecovered strain (Fig. 14) and the more unstable the cyclic stress-strain-temperature response of the NiTi wire will be in the thermomechanical loading test passing through the $[\sigma,T]^{F,R}$ states. Based on the parameters $YT^{F,R}$ for given thermomechanical loading test and 3D ε_{us}-σ-T diagram, one can estimate the cyclic instability of any NiTi wire in any thermomechanical loading test.

This scheme makes it possible to fully understand the results of our earlier work [35] focussed on the TEM analysis of lattice defects in NiTi wires with a range of microstructures subjected to 10 superelastic cycles at room temperature. While no evidence for dislocation slip was observed in 12 ms NiTi wires with small grain size ~50 nm, the pronounced activity of dislocation slip in three austenite slip systems {0 1 1}<100> was observed in 16 ms NiTi wires with ~500 nm mean grain size, the {114} austenite twins were observed only in 18 ms NiTi wires with the largest mean grain size of ~1000 nm. The 3D ε_{us}-σ-T diagram of these three wires would be very different.

The key advantage of this scheme is thus that it can be used to estimate the cyclic instability of stress-strain-temperature response of various NiTi alloys (various compositions given various cold work/heat treatment) subjected to many kinds of cyclic thermomechanical loading tests. Transformation stress $\sigma^{F,R}$ at a given temperature for a particular wire depends mainly on the chemical composition of the alloy. The yield stress σ_y (varies between ~1 700 MPa and ~500 MPa with the heat treatment [19]) depends significantly on the grain size. This is because the plastic yielding is due to combined deformation twinning and dislocation-based kinking [125] constituting the kwinking deformation mechanism [44], which is very sensitive to the grain size. In the case of NiTi wires with small grain size [19], the massive activity of this deformation mechanism leads to strain localization, necking, and fracture at 13-15% macroscopic/engineering strain. The cyclic instability of any NiTi wire in any thermomechanical loading test thus depends on the type of wire (characterized by σ_y and $\sigma^{F,R}$) and the type of the test (characterized by $\sigma^{F,R}$ and T).

There are three basic approaches to how to try to achieve a more stable stress-strain-temperature response from NiTi shape memory alloy. The first classical one consists in the strengthening of the wire to increase the yield stress as much as possible. The second is to determine the 3D ε_{us}-σ-T diagram and perform the thermomechanical loading in such a way that the martensitic

transformation takes place under conditions at which no unrecovered strains and lattice defects are generated. The third one would require the discovery of the mechanisms by which the slip dislocations are generated by the martensitic transformation and modifying the martensitic transformation (lattice parameters of involved phases by adjusting chemical composition) so that it does not generate unrecovered strain and permanent lattice defects when it proceeds cyclically under large stress [136][137][138]. All three approaches can be beneficially combined.

5.3 Correlation between functional and structural fatigue

As illustrated in Fig. 5, the stress-induced martensitic transformation proceeds in a wide range of upper plateau stress in the first superelastic cycle at temperatures between the A_f and M_d. However, as concerns cyclic superelastic deformation, there are limitations at low as well as high temperatures stemming from the cyclic instability. If more than 1 000 cycles and less than 4% ε_{us} in the fatigue life in superelastic regime is demanded, the temperature range is drastically reduced as indicated by color bars in Fig. 7b.

The correlation between functional and structural fatigue of wires with different microstructures tested can be analyzed based on the results presented in Figs. 32, 33. The 10 ms wire with partially recrystallized microstructure (20 nm grain size) exhibits great functional stability (ε_{us} < 0.5 %) and N_f decrease only slightly with increasing temperature. However, the fatigue life is very limited (N_f < 2500 cycles). The fatigue life of the 13 ms wire (75 nm grain size) is longer (N_f ~ 4000 cycles), however, the N_f decreases with increasing temperature faster than in the case of the 10 ms wire, so that the N_f become comparable at the highest temperatures/stresses. The 15 ms microstructure (250 nm grain size) has an excellent fatigue life (N_f ~ 12 000 cycles at 15 °C) compared to the other tested wires, but the temperature window in which the fatigue tests could be performed is severely limited and the N_f sharply decreases with increasing temperature (Fig. 33a).

The numbers of cycles till failure N_f decrease with increasing test temperature for all four wires because the upper (and lower) plateau stress increases with increasing temperature (Fig. 33a, b). That is related to the increasing amount of plastic deformation (Fig. 33c). At the same time, however, the N_f increases with increasing grain size, while larger grains are prone to higher plastic deformation. The amount of plastic deformation accompanying the stress-induced martensitic transformation thus evidently plays a dubious role in controlling both functional fatigue (negative) and structural fatigue (both negative and positive depending on temperature and microstructure). In other words, the functional and structural fatigue of NiTi are coupled in a more complex way than usually assumed.

This intricate phenomenon can be partially resolved when grain size and fracture mechanics is considered. It is well known that the rate of crack propagation upon tensile cycling is strongly affected by plastic deformation at a crack tip. The plastic zone ahead of the propagating crack tip in NiTi was observed in the literature by various methods such as X-ray microdiffraction [57] or DIC/SEM-DIC [54][139]. Gall et al. [106] demonstrated that NiTi has a rather low threshold value of stress intensity factor ΔK_{th} compared to 316 stainless steel or CoCr alloy and fatigue cracks propagate at a quite high rate. Further evidence on the compromised ΔK_{th} of NiTi is shown in [107]. Moreover, cracks propagate even faster and the ΔK_{th} is further decreased in

NiTi containing nanograin microstructure, in which the plastic zone at a crack tip is suppressed and fracture toughness K_{IC} is lowered [54][140]. On the other hand, 'softer' NiTi wires containing recrystallized microstructures with larger grains (as the present 15 ms wires) display a larger compressive zone at the crack tip and provide better shielding against the crack opening (higher opening stress intensity factor K_{op}) [107]. As the 15 ms microstructure with compromised functional stability provides a larger plastic zone and a lower rate of fatigue crack propagation, fatigue life is higher compared to the 10 ms and 13 ms wires.

The analysis of fatigue fracture surfaces provided supplemental information on fatigue crack propagation. Since the fatigue cracks always nucleated at the TiC inclusions (Figs. 34-37) and short cracks (<100 nm) can be found after only 10 superelastic cycles (Figs. 37,38), the rate of fatigue crack propagation controls fatigue life in the superelastic (low cycle fatigue) regime. Although the performed fatigue tests were not designed to evaluate the fatigue crack propagation rate and the number of cycles per striation is unknown, it is evident that the observed fatigue striations are more pronounced and show wider spacing in fatigue tests at higher temperatures and in tests of wires having smaller grain size– i.e. the fatigue cracks most likely propagated faster in tests in which the martensitic transformation proceeded at high stresses and plastic deformation was suppressed.

5.4 Effect of microstructure evolution on fatigue life

As introduced in the previous section, fatigue life in the case of the 15 ms wire is high (N_f ~ 12 000 cycles at 15 °C) but rapidly decreases with increasing temperature (compared to the other samples). The virgin microstructure (grain size) alone cannot fully explain this phenomenon (since plateau stress increases with increasing temperature equally in all wires), it should be somehow related to a microstructure evolution upon tensile cycling. In order to confirm or deny this, TEM lamellae were extracted from the 15 ms wires subjected to fatigue tests at 15 °C and 30 °C (Figs. 40, 41). Note that while microstructure of the 15 ms wire subjected to the fatigue test at 15 °C contained mainly slip dislocations and only a few deformation bands in small grains (after 12 300 cycles), the microstructure of the 15 ms wire tested at 30 °C contained a significantly higher number of deformation bands (after 3 900 cycles) (Fig. 40). This clearly proves that even a very small difference in the temperature of the fatigue test (ΔT = 15 °C) gives rise to a significantly different microstructure of the fatigued wire. Since the difference in upper plateau stress (~ 80 MPa) is rather small (compared to that observed for the 10 ms and 13 ms samples), we believe that the upper plateau stress affects fatigue life indirectly, through its effect on the microstructure evolution accompanying the stress-induced martensitic transformation.

Based on the results in Fig. 40 and systematic analysis of lattice defects in thermomechanically cycled NiTi wires, we believe that the acting deformation mechanism qualitatively changes with increasing temperature and stress, at which the stress-induced martensitic transformation proceeds. This is evidenced by the appearance of deformation bands in the microstructure of the wire tested at 30 °C. The deformation bands are created upon tensile cycling because the fraction of the stress-induced martensite undergoes deformation twinning [41][43][95]. It shall be pointed out that cyclic deformation promotes the creation of deformation bands. It may take tens, hundreds, or thousands of cycles before deformation bands appear in the microstructure depending on temperature, upper plateau stress, and grain size.

Many grains in the bulk microstructure of the 15 ms wire cycled at 15 °C and 30 °C still contain only slip dislocations. However, the microstructure underneath the fatigue fracture surface (Fig. 41) contains grains filled with a large number of deformation bands suggesting that the material, which transformed ahead of the propagating crack tip, was exposed to higher stress than the material elsewhere in the bulk. While at 15 °C, we can see isolated deformation bands in the grains bisected by the propagating fatigue crack (Fig. 41b), there is a high density of deformation bands spreading frequently across multiple grains at 30 °C (Fig. 41f-h). These observations also confirm that fatigue cracks in superelastic NiTi propagate mainly transgranularly (Fig. 41b,c), as also observed by other investigators [113].

We may consider the microstructure observed along the crack path as being gradually "cold-worked" by the plastic zone ahead of the advancing crack into a laminate of deformation bands that are ~50 nm wide. This microstructure resembles the microstructure of NiTi wire deformed above yield stress [40]. Furthermore, the twinned microstructure creates high strain gradients and local strain can increase above 30 % while a macroscopic strain is below 10 % [96]. Therefore, the virgin microstructure of the 15 ms wire (Fig. 40 a-c) becomes gradually rebuilt ahead of the advancing crack by the cyclic martensitic transformation proceeding at high stresses approaching yield stress. The fatigue crack in the test at 30 °C thus propagated through the refined microstructure containing laminate of deformation bands. As short fatigue cracks (< 100 nm) were observed after 10 loading cycles only (Fig. 43,44), we believe that these processes control the fatigue life of NiTi in the superelastic regime. Although the wire surface is rough, as no polishing was applied, this is the same for all microstructures. Despite the high density of those small cracks underneath the surface, the terminal fatigue cracks always nucleated at TiC inclusions and further investigation of the crack nucleation and growth is needed to verify the formation of deformation bands around inclusions and fatigue cracks in the early stage of the crack nucleation. Nevertheless, our findings agree with the results in the literature [24][27] claiming that the majority of fatigue life is spent in the crack propagation stage.

Although no direct observation of the deformed microstructure in the 10 ms wire after fatigue tests has been performed, the formation of deformation bands in this sample is unlikely, since the observed accumulation of unrecovered strain ε_{us} is negligible (Figs. 32 and 33). In the case of the 13 ms wires, the deformation bands appear in fatigue tests performed at high temperatures [37]. However, the formation of deformation bands on a larger scale at room temperature is unlikely. The experimentally observed decrease of the fatigue life with increasing test temperature (stress, unrecovered strain) (Fig. 33) was thus rationalized by considering the effect of the initial microstructure and its susceptibility to the refinement during superelastic loading on the rate of fatigue crack propagation.

Considering aspects of grain size and microstructure evolution, the 13 ms wire seems to be a good compromise between the 10 ms wire (short fatigue life due to the lack of plastic deformation at any test temperature) and the 15 ms wire (short fatigue life due to microstructure refinement by the plastic deformation ahead of the advancing crack at elevated temperature). In order to improve the fatigue life of superelastic NiTi wire in the required temperature range, we thus need to manipulate its microstructure so that it allows for some plastic deformation but suppresses the formation of deformation bands.

5.5 Effect of aging treatment on functional properties and fatigue life

Precipitation processes in Ni-rich NiTi were extensively studied in the literature [22][57][59][60][69]. Information on functional properties and fatigue life of the aged NiTi can be found in [3][17] and [9][21], respectively. It appears that the precipitation of Ni_4Ti_3 upon aging generally increases transformation temperature (depletion of Ni from the NiTi matrix) and improves the stability of stress-strain responses (strengthening by nanoprecipitates) of Ni-rich NiTi compared to the solution-treated alloys.

This is nicely confirmed in our experiments, as the 400 °C for 1h aging treatment shifts M_s temperature upwards by around 30 °C, functional stability at elevated temperatures is improved (Fig. 32b), fatigue life is longer, but the wire does not show superelasticity below 40 °C, which is, of course, a serious limitation for medical applications. The fatigue life of the aged sample is up to 300 % longer when compared with the 13ms sample without aging tested at the same temperature (Fig. 33a) but only up to ~ 20 % longer in tests at the same upper plateau stress σ_p^{up} (Fig. 33b) or unrecovered strain (Fig. 33c). So, the fatigue life improvement due to aging very much depends on how we look at it and what are the application-related requirements.

As the fatigue life is controlled by the crack propagation rate, we have to understand why and how aging affects the crack propagation rate. It can be concluded from the discussion in section 4.3 that the fatigue life improvement by aging is achieved via three simultaneous beneficial effects that slow down the crack propagation upon tensile cycling: i) decrease of upper plateau stress, ii) enabling crack tip shielding by plastic deformation (ductility is not deteriorated by aging) and iii) improvement of resistance against microstructure evolution upon tensile cycling.

There is no warranty that the employed 13 ms+400 °C/1h heat treatment is ideal, however, it is a suitable compromise leading to sufficient fatigue life and functional stability. We originally thought that applying short electro-pulse treatments after cold work will result in improvement of fatigue performance compared to NiTi alloys cold-worked and heat-treated in an environmental furnace but this turned out not to be the case. In reality, plastic deformation is very limited in NiTi wires treated by a short electric pulse (< 12 ms) containing nanocrystalline microstructures (d < 50nm). Optimized cold work/heat treatment (~ 13 ms) leading to grain size d = 50 – 100 nm followed by aging at 400 °C for 1h improves the resistance against deformation twinning in martensite and allows the creation of larger plastic at a crack tip at the same time, which is desired. On the other hand, it destroys the superelasticity of the wire at room or body temperature, which is obviously a problem. There might be several ways how to improve that. Superelasticity at body temperature can be achieved by varying the aging time and/or temperature and the problem with preferential precipitation of Ni_4Ti_3 along grain boundaries can be solved by applying a small plastic deformation prior to the low temperature (< 300 °C) aging to introduce nucleation sites for precipitation in the grain interior according to Li et al. [20], which would be even more beneficial for the 15 ms microstructure with larger grains.

6 Conclusions

Functional thermomechanical properties and fatigue life of NiTi wires with specific microstructures adjusted by cold work/heat treatment were investigated by thermomechanical testing in a wide temperature range and by electron microscopy (SEM, TEM, and STEM). The key results can be summarized as follows:

Adjustment of the virgin microstructure by heat treatment

A cold-worked NiTi wire (cut from a single spool) was subjected to pulse heat treatments by electric current, where constant power (160 Wmm^{-3}) of the pulse was applied for 10 ms, 13 ms, and 15 ms to produce samples with different grain sizes. Moreover, a part of the samples was further aged at 400 °C for 1 h to introduce Ni-rich precipitates. The grain size d of the NiTi samples heat-treated by the 10 ms, 13 ms, and 15 ms pulse is 20 nm, 75 nm, and 250 nm, respectively. The 400°C/1h aging does not increase the grain size of microstructures with $d > 75$ nm, which is ideal for assessing the precipitation effect on functional and fatigue performance.

Functional fatigue

A series of cyclic thermomechanical loading tests (10 closed-loop cycles) on the 15 ms wire were performed to investigate the origin of the cyclic instability of functional behaviors of NiTi. The recorded accumulated unrecovered strains and density of permanent lattice defects increased rapidly with increasing temperature/stress, at which the forward and/or reverse martensitic transformation proceeded in the test.

Two distinctly different cyclic stress-strain-temperature responses of the wire were found:

- relatively stable, generating only marginal accumulated unrecovered strain and/or few isolated lattice defects if both the forward and reverse martensitic transformations proceeded at low external stress ($\sigma < 100$ MPa)
- very unstable, generating significant accumulated unrecovered strain and high density of slip dislocations and deformation bands if the forward or reverse martensitic transformation proceeded under large external stress ($\sigma > 250$ MPa).

The type of permanent lattice defects observed in the microstructure of the cycled wire by TEM was found to be dependent on the temperature/stress, at which the forward and reverse martensitic transformation proceeded in the test, in particular:

- at low stresses ($\sigma < 100$ MPa), the cyclic martensitic transformation generated only a few dislocation loops and segments, and the recorded accumulated unrecovered strains were negligible ($\varepsilon_{us} < 0.1$ %)
- at intermediate stresses (100 MPa $< \sigma <$ 400 MPa), high density of (110)<001> slip dislocations and a few isolated deformation bands were observed in the microstructure and accumulated unrecovered strains reached few percent (~ 0.5-2 %)
- at high stresses ($\sigma > 400$ MPa), deformation bands containing B19’ martensite or {114} austenite twins alongside high density of slip dislocations were observed in the

microstructure, and accumulated unrecovered strains became very large (> 2 %) accompanied by loss of transformation plateau

Similar microstructural changes occur in the 10 ms and 13 ms samples. However, these changes are suppressed by the smaller grain size of these samples and occur higher above A_f. Therefore, the 10 ms samples exhibit excellent performance in functional fatigue (ε_{us} < 0.5 % in fatigue tests) and flat transformation plateau in the majority of cyclic superelastic tests.

Fatigue life in superelastic tests

The samples exhibit the highest fatigue life and best functional stability when superelastically cycled at low temperatures slightly above A_f. This is not surprising since the magnitude of the upper plateau transformation stress is the essential parameter in fatigue life in the superelastic regime. However, it was found that the NiTi wire containing the smallest 20 nm grains, which shows remarkably stable superelasticity, displayed the lowest fatigue life (N_f < 2 500 cycles) among the tested samples. The NiTi wire containing recrystallized 250 nm grains showing unstable stress-strain response exhibits the best fatigue performance (N_f ~ 12 000 cycles), although in a narrow temperature range only, since the N_f decreased rapidly with the increasing test temperature (stress). This suggests that the superelastic fatigue performance of NiTi wires is different from the state-of-the-art view if the range of microstructures (grain sizes) and test temperatures are considered.

It is claimed that, for the same material parameters (wire diameter, surface quality, inclusions, etc.), the superelastic fatigue life of NiTi wires is largely controlled by the crack propagation rate, which depends on the: i) upper plateau stress at which the stress-induced martensitic transformation proceeds as well as on the ii) crack shielding effect of the plastic zone ahead of a propagating crack. Moreover, it was found that short cracks (~ 100 nm within the surface grain) are generated already in a couple of superelastic cycles, and TiC inclusions are common nucleation sites of fatigue cracks, causing final failure of the tested samples.

A strategy how to improve the fatigue life of superelastic NiTi is proposed. It consists of a modification of the alloy microstructure to allow for some plastic deformation to accompany the stress-induced martensitic transformation upon tensile cycling but to suppress the plastic deformation processes in martensite leading to the formation of deformation bands in the microstructure (microstructure refinement). Among the tested microstructures, these requirements are best complied by the aged 13 ms wire containing 75 nm grains and Ni_4Ti_3 nano-precipitates.

The effect of Ni_4Ti_3 precipitation on functional fatigue and superelastic fatigue life

The average size of the precipitates created by aging at 400 °C for 1 h is approx. 20 nm in length and 8 nm in thickness in the microstructure with grain size d ~ 75 nm. A direct comparison of the microstructures with and without Ni-rich precipitates shows that although precipitates nucleate mainly on grain boundaries, the tensile strength of the aged samples increases by 200 MPa (15 % of the initial value) at room temperature. Aging shifts superelastic temperature window up by approx. 30 °C, slightly increases fatigue life (10-15 %) and decreases plateau strain by approx. 1 %. The same aging of microstructure with d ~ 250 nm results in 30 % larger precipitates and a lower increase in tensile strength (by ~ 100 MPa).

Author's publications related to dissertation

[1] Tyc O, Heller L, Vronka M, Šittner P. Effect of temperature on fatigue of superelastic NiTi wires. International Journal of Fatigue 2020;134:105470. https://doi.org/10.1016/j.ijfatigue.2020.105470.

[2] Tyc O, Molnárová O, Šittner P. Effect of microstructure on fatigue of superelastic NiTi wires. International Journal of Fatigue 2021. https://doi.org/10.1016/j.ijfatigue.2021.106400

[3] Tyc O, Heller L, Šittner P. Lattice defects generated by cyclic thermomechanical loading of superelastic NiTi wire. Shape Memory and Superelasticity 2021;7:65-88. https://doi.org/10.1007/s40830-021-00315-4.

[4] Tyc O, Pilch J, Šittner P, Haušild P. Investigation of the Precipitation Processes in NiTi Wires. Proceedings of the International Conference on Martensitic Transformations: Chicago 2018:173–7. https://doi.org/10.1007/978-3-319-76968-4_27.

[5] Tyc O, Pilch J, Sittner P. Fatigue of superelastic NiTi wires with different plateau strain. Procedia Structural Integrity 2016;2:1489–96. https://doi.org/10.1016/j.prostr.2016.06.189.

[6] Chen Y, Tyc O, Molnárová O, Heller L, Šittner P. Tensile Deformation of Superelastic NiTi Wires in Wide Temperature and Microstructure Ranges. Shape Memory and Superelasticity 2018;5:42–62. https://doi.org/10.1007/s40830-018-00205-2.

[7] Heller L, Seiner H, Šittner P, Sedlák P, Tyc O, Kadeřávek L. On the plastic deformation accompanying cyclic martensitic transformation in thermomechanically loaded NiTi. International Journal of Plasticity 2018;111:53–71. https://doi.org/10.1016/j.ijplas.2018.07.007.

[8] Heller L, Šittner P, Sedlák P, Seiner H, Tyc O, Kadeřávek L, et al. Beyond the strain recoverability of martensitic transformation in NiTi. International Journal of Plasticity 2019;116:232–64. https://doi.org/10.1016/j.ijplas.2019.01.007.

[9] Chen Y, Molnárová O, Tyc O, Kadeřávek L, Heller L, Šittner P. Recoverability of large strains and deformation twinning in martensite during tensile deformation of NiTi shape memory alloy polycrystals. Acta Materialia 2019;180:243–59. https://doi.org/10.1016/j.actamat.2019.09.012.

[10] Šittner P, Molnárová O, Kadeřávek L, Tyc O, Heller L. Deformation twinning in martensite affecting functional behavior of NiTi shape memory alloys. Materialia 2020;9:100506. https://doi.org/10.1016/j.mtla.2019.100506.

[11] Chen Y, Tyc O, Kadeřávek L, Molnárová O, Heller L, Šittner P. Temperature and microstructure dependence of localized tensile deformation of superelastic NiTi wires. Materials & Design 2019;174:107797. https://doi.org/10.1016/j.matdes.2019.107797.

[12] Šittner P, Heller L, Sedlák P, Chen Y, Tyc O, Molnárová O, et al. B2 ⇒ B19′ ⇒ B2T Martensitic Transformation as a Mechanism of Plastic Deformation of NiTi. Shape Memory and Superelasticity 2019;5:383–96. https://doi.org/10.1007/s40830-019-00250-5.

References

[1] Mahtabi MJ, Shamsaei N, Mitchell MR. Fatigue of Nitinol: The state-of-the-art and ongoing challenges. Journal of the Mechanical Behavior of Biomedical Materials 2015;50:228–54. https://doi.org/10.1016/j.jmbbm.2015.06.010.

[2] Hartl DJ, Lagoudas DC. Aerospace applications of shape memory alloys. Proceedings of the Institution of Mechanical Engineers, Part G: Journal of Aerospace Engineering 2007;221:535–52. https://doi.org/10.1243/09544100jaero211.

[3] Pelton AR, Dicello J, Miyazaki S. Optimisation of processing and properties of medical grade Nitinol wire. Minimally Invasive Therapy & Allied Technologies 2000;9:107–18. https://doi.org/10.3109/13645700009063057.

[4] Duerig T, Pelton A, Stöckel D. An overview of nitinol medical applications. Materials Science and Engineering: A 1999;273-275:149–60. https://doi.org/10.1016/S0921-5093(99)00294-4.

[5] Takayuki Yoneyama, Shuichi Miyazaki. Shape memory alloys for biomedical applications. Woodhead Publishing Limited; 2009.

[6] Furuya Y, Shimada H. Shape memory actuators for robotic applications. Materials & Design 1991;12:21–8. https://doi.org/10.1016/0261-3069(91)90088-l.

[7] Qian S, Geng Y, Wang Y, Ling J, Hwang Y, Radermacher R, et al. A review of elastocaloric cooling: Materials, cycles and system integrations. International Journal of Refrigeration 2016;64:1–19. https://doi.org/10.1016/j.ijrefrig.2015.12.001.

[8] Langan M, O'Toole K. A new technology for cost effective low grade waste heat recovery. Energy Procedia 2017;123:188–95. https://doi.org/10.1016/j.egypro.2017.07.261.

[9] Silva JD, Martins SC, Lopes NI de A, Resende PD, Santos LA, Buono VTL. Effects of aging treatments on the fatigue resistance of superelastic NiTi wires. Materials Science and Engineering: A 2019;756:54–60. https://doi.org/10.1016/j.msea.2019.04.037.

[10] Jaureguizahar SM, Chapetti MD, Yawny AA. Fatigue of NiTi shape memory wires. Procedia Structural Integrity 2016;2:1427–34. https://doi.org/10.1016/j.prostr.2016.06.181.

[11] Tyc O, Pilch J, Sittner P. Fatigue of superelastic NiTi wires with different plateau strain. Procedia Structural Integrity 2016;2:1489–96. https://doi.org/10.1016/j.prostr.2016.06.189.

[12] Zhang K, Kang G, Sun Q. High fatigue life and cooling efficiency of NiTi shape memory alloy under cyclic compression. Scripta Materialia 2019;159:62–7. https://doi.org/10.1016/j.scriptamat.2018.09.012.

[13] Wu Y, Ertekin E, Sehitoglu H. Elastocaloric cooling capacity of shape memory alloys – Role of deformation temperatures, mechanical cycling, stress hysteresis and inhomogeneity of transformation. Acta Materialia 2017;135:158–76. https://doi.org/10.1016/j.actamat.2017.06.012.

[14] Casati R, Passaretti F, Tuissi A. Effect of electrical heating conditions on functional fatigue of thin NiTi wire for shape memory actuators. Procedia Engineering 2011;10:3423–8. https://doi.org/10.1016/j.proeng.2011.04.564.

[15] Mohd Jani J, Leary M, Subic A, Gibson MA. A review of shape memory alloy research, applications and opportunities. Materials & Design (1980-2015) 2014;56:1078–113. https://doi.org/10.1016/j.matdes.2013.11.084.

[16] Karhu M, Lindroos T. Long-term behaviour of binary Ti–49.7Ni (at.%) SMA actuators—the fatigue lives and evolution of strains on thermal cycling. Smart Materials and Structures 2010;19:115019. https://doi.org/10.1088/0964-1726/19/11/115019.

[17] Tyc O, Pilch J, Šittner P, Haušild P. Investigation of the Precipitation Processes in NiTi Wires. Proceedings of the International Conference on Martensitic Transformations: Chicago 2018:173–7. https://doi.org/10.1007/978-3-319-76968-4_27.

[18] Delville R, Malard B, Pilch J, Sittner P, Schryvers D. Microstructure changes during non-conventional heat treatment of thin Ni–Ti wires by pulsed electric current studied by transmission electron microscopy. Acta Materialia 2010;58:4503–15. https://doi.org/10.1016/j.actamat.2010.04.046.

[19] Chen Y, Tyc O, Molnárová O, Heller L, Šittner P. Tensile Deformation of Superelastic NiTi Wires in Wide Temperature and Microstructure Ranges. Shape Memory and Superelasticity 2018;5:42–62. https://doi.org/10.1007/s40830-018-00205-2.
[20] Li X, Chen H, Guo W, Guan Y, Wang Z, Zeng Q, et al. Improved superelastic stability of NiTi shape memory alloys through surface nano-crystallization followed by low temperature aging treatment. Intermetallics 2021;131:107114. https://doi.org/10.1016/j.intermet.2021.107114.
[21] Kollerov M, Lukina E, Gusev D, Mason P, Wagstaff P. Impact of material structure on the fatigue behaviour of NiTi leading to a modified Coffin–Manson equation. Materials Science and Engineering: A 2013;585:356–62. https://doi.org/10.1016/j.msea.2013.07.072.
[22] Gall K, Maier HJ. Cyclic deformation mechanisms in precipitated NiTi shape memory alloys. Acta Materialia 2002;50:4643–57. https://doi.org/10.1016/s1359-6454(02)00315-4.
[23] Miyazaki S, Mizukoshi K, Ueki T, Sakuma T, Liu Y. Fatigue life of Ti–50 at.% Ni and Ti–40Ni–10Cu (at.%) shape memory alloy wires. Materials Science and Engineering: A 1999;273-275:658–63. https://doi.org/10.1016/s0921-5093(99)00344-5.
[24] Bahia M, Fonsecadias R, Buono V. The influence of high amplitude cyclic straining on the behaviour of superelastic NiTi. International Journal of Fatigue 2006;28:1087–91. https://doi.org/10.1016/j.ijfatigue.2005.11.008.
[25] Maletta C, Sgambitterra E, Furgiuele F, Casati R, Tuissi A. Fatigue properties of a pseudoelastic NiTi alloy: Strain ratcheting and hysteresis under cyclic tensile loading. International Journal of Fatigue 2014;66:78–85. https://doi.org/10.1016/j.ijfatigue.2014.03.011.
[26] Sedmák P, Pilch J, Heller L, Kopeček J, Wright J, Sedlák P, et al. Grain-resolved analysis of localized deformation in nickel-titanium wire under tensile load. Science 2016;353:559–62. https://doi.org/10.1126/science.aad6700.
[27] Figueiredo A, Modenesi P, Buono V. Low-cycle fatigue life of superelastic NiTi wires. International Journal of Fatigue 2009;31:751–8. https://doi.org/10.1016/j.ijfatigue.2008.03.014.
[28] Pelton AR, Fino-Decker J, Vien L, Bonsignore C, Saffari P, Launey M, et al. Rotary-bending fatigue characteristics of medical-grade Nitinol wire. Journal of the Mechanical Behavior of Biomedical Materials 2013;27:19–32. https://doi.org/10.1016/j.jmbbm.2013.06.003.
[29] Alarcon E, Heller L, Chirani SA, Šittner P, Kopeček J, Saint-Sulpice L, et al. Fatigue performance of superelastic NiTi near stress-induced martensitic transformation. International Journal of Fatigue 2017;95:76–89. https://doi.org/10.1016/j.ijfatigue.2016.10.005.
[30] Racek J, Šittner P. Environmental fatigue of superelastic NiTi wire with two surface finishes. Journal of the Mechanical Behavior of Biomedical Materials 2020;111:104028. https://doi.org/10.1016/j.jmbbm.2020.104028.
[31] Rahim M, Frenzel J, Frotscher M, Pfetzing-Micklich J, Steegmüller R, Wohlschlögel M, et al. Impurity levels and fatigue lives of pseudoelastic NiTi shape memory alloys. Acta Materialia 2013;61:3667–86. https://doi.org/10.1016/j.actamat.2013.02.054.
[32] Launey M, Robertson SW, Vien L, Senthilnathan K, Chintapalli P, Pelton AR. Influence of microstructural purity on the bending fatigue behavior of VAR-melted superelastic Nitinol. Journal of the Mechanical Behavior of Biomedical Materials 2014;34:181–6. https://doi.org/10.1016/j.jmbbm.2014.02.008.
[33] Robertson SW, Launey M, Shelley O, Ong I, Vien L, Senthilnathan K, et al. A statistical approach to understand the role of inclusions on the fatigue resistance of superelastic Nitinol wire and tubing. Journal of the Mechanical Behavior of Biomedical Materials 2015;51:119–31. https://doi.org/10.1016/j.jmbbm.2015.07.003.
[34] Heller L, Seiner H, Šittner P, Sedlák P, Tyc O, Kadeřávek L. On the plastic deformation accompanying cyclic martensitic transformation in thermomechanically loaded NiTi. International Journal of Plasticity 2018;111:53–71. https://doi.org/10.1016/j.ijplas.2018.07.007.
[35] Delville R, Malard B, Pilch J, Sittner P, Schryvers D. Transmission electron microscopy investigation of dislocation slip during superelastic cycling of Ni–Ti wires. International Journal of Plasticity 2011;27:282–97. https://doi.org/10.1016/j.ijplas.2010.05.005.
[36] Sedmák P, Šittner P, Pilch J, Curfs C. Instability of cyclic superelastic deformation of NiTi investigated by synchrotron X-ray diffraction. Acta Materialia 2015;94:257–70. https://doi.org/10.1016/j.actamat.2015.04.039.

[37] Tyc O, Heller L, Vronka M, Šittner P. Effect of temperature on fatigue of superelastic NiTi wires. International Journal of Fatigue 2020;134:105470. https://doi.org/10.1016/j.ijfatigue.2020.105470.
[38] Šittner P, Sedlák P, Seiner H, Sedmák P, Pilch J, Delville R, et al. On the coupling between martensitic transformation and plasticity in NiTi: Experiments and continuum based modelling. Progress in Materials Science 2018;98:249–98. https://doi.org/10.1016/j.pmatsci.2018.07.003.
[39] Heller L, Šittner P, Sedlák P, Seiner H, Tyc O, Kadeřávek L, et al. Beyond the strain recoverability of martensitic transformation in NiTi. International Journal of Plasticity 2019;116:232–64. https://doi.org/10.1016/j.ijplas.2019.01.007.
[40] Chen Y, Molnárová O, Tyc O, Kadeřávek L, Heller L, Šittner P. Recoverability of large strains and deformation twinning in martensite during tensile deformation of NiTi shape memory alloy polycrystals. Acta Materialia 2019;180:243–59. https://doi.org/10.1016/j.actamat.2019.09.012.
[41] Šittner P, Molnárová O, Kadeřávek L, Tyc O, Heller L. Deformation twinning in martensite affecting functional behavior of NiTi shape memory alloys. Materialia 2020;9:100506. https://doi.org/10.1016/j.mtla.2019.100506.
[42] Tyc O, Heller L, Šittner P. Lattice defects generated by cyclic thermomechanical loading of superelastic NiTi wire. Shape Memory and Superelasticity 2021;proof. https://doi.org/10.1007/s40830-021-00315-4 .
[43] Molnárová O, Šittner P, Veselý J, Cieslar M. TEM analysis of deformation bands created by tensile deformation of superelastic NiTi wires. Materials Characterization 2020;167:110470. https://doi.org/10.1016/j.matchar.2020.110470.
[44] H. Seiner, P. Sedlák, L. Heller, O. Molnárová, P. Šittner, On the origin of (20-1) interfaces in B19‘ NiTi martensite, in preparation, H. Seiner, The (20¯1) interfaces in plastically formed NiTi martensite - twins or 'kwinks'? Presentation available online from ASM international, www.asminternational.org/news/videos/-/journal_content/56/10192/42847968/VIDEO
[45] Gao Y, Casalena L, Bowers ML, Noebe RD, Mills MJ, Wang Y. An origin of functional fatigue of shape memory alloys. Acta Materialia 2017;126:389–400. https://doi.org/10.1016/j.actamat.2017.01.001.
[46] Gao Y. Symmetry and pathway analyses of the twinning modes in Ni–Ti shape memory alloys. Materialia 2019;6:100320. https://doi.org/10.1016/j.mtla.2019.100320.
[47] Bowers ML, Gao Y, Yang L, Gaydosh DJ, De Graef M, Noebe RD, et al. Austenite grain refinement during load-biased thermal cycling of a Ni49.9Ti50.1 shape memory alloy. Acta Materialia 2015;91:318–29. https://doi.org/10.1016/j.actamat.2015.03.017.
[48] Bucsek AN, Casalena L, Pagan DC, Paul PP, Chumlyakov Y, Mills MJ, et al. Three-dimensional in situ characterization of phase transformation induced austenite grain refinement in nickel-titanium. Scripta Materialia 2019;162:361–6. https://doi.org/10.1016/j.scriptamat.2018.11.043.
[49] Otsuka K, Ren X. Physical metallurgy of Ti–Ni-based shape memory alloys. Progress in Materials Science 2005;50:511–678. https://doi.org/10.1016/j.pmatsci.2004.10.001.
[50] Tang W, Sundman B, Sandström R, Qiu C. New modelling of the B2 phase and its associated martensitic transformation in the Ti–Ni system. Acta Materialia 1999;47:3457–68. https://doi.org/10.1016/s1359-6454(99)00193-7.
[51] Clarence Marvin Wayman, Kazuhiro Ōtsuka. Shape memory materials. Cambridge; New York: Cambridge University Press; 1999.
[52] Benafan O, Noebe RD, Padula SA, Garg A, Clausen B, Vogel S, et al. Temperature dependent deformation of the B2 austenite phase of a NiTi shape memory alloy. International Journal of Plasticity 2013;51:103–21. https://doi.org/10.1016/j.ijplas.2013.06.003.
[53] Malard B, Pilch J, Sittner P, Delville R, Curfs C. In situ investigation of the fast microstructure evolution during electropulse treatment of cold drawn NiTi wires. Acta Materialia 2011;59:1542–56. https://doi.org/10.1016/j.actamat.2010.11.018.
[54] Ahadi A, Sun Q. Grain size dependence of fracture toughness and crack-growth resistance of superelastic NiTi. Scripta Materialia 2016;113:171–5. https://doi.org/10.1016/j.scriptamat.2015.10.036.
[55] Humphreys F, Hatherly M. Recrystallization and Related Annealing Phenomena. Elsevier; 2004.
[56] Tyc O. Studium precipitace v tenkých kovových vláknech ze slitiny NiTi. Výzkumný úkol, FJFI ČVUT, Praha, 2014.

[57] Fan G, Chen W, Yang S, Zhu J, Ren X, Otsuka K. Origin of abnormal multi-stage martensitic transformation behavior in aged Ni-rich Ti–Ni shape memory alloys. Acta Materialia 2004;52:4351–62. https://doi.org/10.1016/j.actamat.2004.06.002.
[58] Wang X, Kustov S, Li K, Schryvers D, Verlinden B, Van Humbeeck J. Effect of nanoprecipitates on the transformation behavior and functional properties of a Ti–50.8 at.% Ni alloy with micron-sized grains. Acta Materialia 2015;82:224–33. https://doi.org/10.1016/j.actamat.2014.09.018.
[59] Michutta J, Somsen C, Yawny A, Dlouhy A, Eggeler G. Elementary martensitic transformation processes in Ni-rich NiTi single crystals with Ni4Ti3 precipitates. Acta Materialia 2006;54:3525–42. https://doi.org/10.1016/j.actamat.2006.03.036.
[60] Tirry W, Schryvers D. Quantitative determination of strain fields around Ni4Ti3 precipitates in NiTi. Acta Materialia 2005;53:1041–9. https://doi.org/10.1016/j.actamat.2004.10.049.
[61] Frick CP, Ortega AM, Tyber J, Gall K, Maier HJ, El.M. A, et al. Thermal Processing of Polycrystalline NiTi Shape Memory Alloys. MRS Proceedings 2004;855. https://doi.org/10.1557/proc-855-w1.9.
[62] Ren X, Miura N, Zhang J, Otsuka K, Tanaka K, Koiwa M, et al. A comparative study of elastic constants of Ti–Ni-based alloys prior to martensitic transformation. Materials Science and Engineering: A 2001;312:196–206. https://doi.org/10.1016/s0921-5093(00)01876-1.
[63] Nishida M, Wayman CM. Electron microscopy studies of precipitation processes in near-equiatomic TiNi shape memory alloys. Materials Science and Engineering 1987;93:191–203. https://doi.org/10.1016/0025-5416(87)90424-1.
[64] Khalil-Allafi J, Dlouhy A, Eggeler G. Ni4Ti3-precipitation during aging of NiTi shape memory alloys and its influence on martensitic phase transformations. Acta Materialia 2002;50:4255–74. https://doi.org/10.1016/s1359-6454(02)00257-4.
[65] Drexel MJ, Selvaduray GS, Pelton AR. The Effects of Cold Work and Heat Treatment on the Properties of Nitinol Wire. Proceedings of the International Conference on Shape Memory and Superelastic Technologies, 2006, p. 447–54.
[66] Li DY, Chen LQ. Selective variant growth of coherent Ti11Ni14 precipitate in a TiNi alloy under applied stresses. Acta Materialia 1997;45:471–9. https://doi.org/10.1016/s1359-6454(96)00207-8.
[67] Bojda O, Eggeler G, Dlouhý A. Precipitation of Ni4Ti3-variants in a polycrystalline Ni-rich NiTi shape memory alloy. Scripta Materialia 2005;53:99–104. https://doi.org/10.1016/j.scriptamat.2005.03.006.
[68] Shakeri MS, Khalil-Allafi J, Abbasi-Chianeh V, Ghabchi A. The influence of Ni4Ti3 precipitates orientation on two-way shape memory effect in a Ni-rich NiTi alloy. Journal of Alloys and Compounds 2009;485:320–3. https://doi.org/10.1016/j.jallcom.2009.05.084.
[69] Nishida M, Wayman CM. Electron microscopy studies of the “Premartensitic” transformations in an aged Ti-51 at%Ni shape memory alloy. Metallography 1988;21:255–73. https://doi.org/10.1016/0026-0800(88)90024-9.
[70] Vojtěch D, Michalcová A, Čapek J, Marek I, Dragounová L. Structural and mechanical stability of the nano-crystalline Ni–Ti (50.9 at.% Ni) shape memory alloy during short-term heat treatments. Intermetallics 2014;49:7–13. https://doi.org/10.1016/j.intermet.2013.12.013.
[71] Yin H, He Y, Moumni Z, Sun Q. Effects of grain size on tensile fatigue life of nanostructured NiTi shape memory alloy. International Journal of Fatigue 2016;88:166–77. https://doi.org/10.1016/j.ijfatigue.2016.03.023.
[72] Pilch J, Šittner P. A method of heat treatment and/or inspection of functional mechanical properties, particularly transformation strain and/or strength, of shape memory alloy wires and apparatus for the application of this method. Patent applications PV2009-279, PCT/CZ2010/000058.
[73] Pilch J. Studium funkčních vlastností tenkých vláken niti pro aplikace v smart strukturách a textiliích. Dissertation. 2011.
[74] Pilch J, Heller L, Sittner P. Final thermomechanical treatment of thin NiTi wires for textile applications by electric current. ESOMAT 2009 - 8th European Symposium on Martensitic Transformations 2009. https://doi.org/10.1051/esomat/200905024.

[75] Šittner P, Landa M, Lukáš P, Novák V. R-phase transformation phenomena in thermomechanically loaded NiTi polycrystals. Mechanics of Materials 2006;38:475–92. https://doi.org/10.1016/j.mechmat.2005.05.025.
[76] Helbert G, Saint-Sulpice L, Arbab Chirani S, Dieng L, Lecompte T, Calloch S, et al. Experimental characterisation of three-phase NiTi wires under tension. Mechanics of Materials 2014;79:85–101. https://doi.org/10.1016/j.mechmat.2014.07.020.
[77] Uchil J, Mohanchandra KP, Kumara KGanesh, Mahesh KK. Study of critical dependence of stable phases in Nitinol on heat treatment using electrical resistivity probe. Materials Science and Engineering: A 1998;251:58–63. https://doi.org/10.1016/s0921-5093(98)00636-4.
[78] Eggeler G, Hornbogen E, Yawny A, Heckmann A, Wagner M. Structural and functional fatigue of NiTi shape memory alloys. Materials Science and Engineering: A 2004;378:24–33. https://doi.org/10.1016/j.msea.2003.10.327.
[79] Pelton AR. Nitinol Fatigue: A Review of Microstructures and Mechanisms. Journal of Materials Engineering and Performance 2011;20:613–7. https://doi.org/10.1007/s11665-011-9864-9.
[80] Weighardt SC, Maier HJ, Chumlyakov YI. Dependence of functional degradation on crystallographic orientation in NiTi shape memory alloys aged under stress. Journal of Alloys and Compounds 2013;577:S219–21. https://doi.org/10.1016/j.jallcom.2012.02.005.
[81] Schaefer A, Wagner MF-X . Strain mapping at propagating interfaces in pseudoelastic NiTi. ESOMAT 2009 - 8th European Symposium on Martensitic Transformations 2009. https://doi.org/10.1051/esomat/200906031.
[82] Dong L, Zhou RH, Wang XL, Hu GK, Sun QP. On interfacial energy of macroscopic domains in polycrystalline NiTi shape memory alloys. International Journal of Solids and Structures 2016;80:445–55. https://doi.org/10.1016/j.ijsolstr.2015.10.006.
[83] Nishida M, Ii S, Kitamura K, Furukawa T, Chiba A, Hara T, et al. New deformation twinning mode of B19′ martensite in Ti-Ni shape memory alloy. Scripta Materialia 1998;39:1749–54. https://doi.org/10.1016/s1359-6462(98)00366-2.
[84] Ezaz T, Sehitoglu H, Abuzaid W, Maier HJ. Higher Order twin modes in martensitic NiTi—The (20-1) case. Materials Science and Engineering: A 2012;558:422–30. https://doi.org/10.1016/j.msea.2012.08.022.
[85] Chowdhury P, Sehitoglu H. Deformation physics of shape memory alloys – Fundamentals at atomistic frontier. Progress in Materials Science 2017;88:49–88. https://doi.org/10.1016/j.pmatsci.2017.03.003.
[86] Chen Y, Tyc O, Kadeřávek L, Molnárová O, Heller L, Šittner P. Temperature and microstructure dependence of localized tensile deformation of superelastic NiTi wires. Materials & Design 2019;174:107797. https://doi.org/10.1016/j.matdes.2019.107797.
[87] Goo E, Duerig T, Melton K, Sinclair R. Mechanical twinning in Ti50Ni47Fe3 and Ti49Ni51 alloys. Acta Metallurgica 1985;33:1725–33. https://doi.org/10.1016/0001-6160(85)90167-1.
[88] Karaman I, Yapici GG, Chumlyakov YI, Kireeva IV. Deformation twinning in difficult-to-work alloys during severe plastic deformation. Materials Science and Engineering: A 2005;410-411:243–7. https://doi.org/10.1016/j.msea.2005.08.021.
[89] Tyumentsev AN, Surikova NS, Litovchenko IYu, Pinzhin YuP, Korotaev AD, Lysenko OV. Mechanism of deformation and crystal lattice reorientation in strain localization bands and deformation twins of the B2 phase of titanium nickelide. Acta Materialia 2004;52:2067–74. https://doi.org/10.1016/j.actamat.2004.01.001.
[90] Hu L, Jiang S, Zhang Y, Zhao Y, Liu S, Zhao C. Multiple plastic deformation mechanisms of NiTi shape memory alloy based on local canning compression at various temperatures. Intermetallics 2016;70:45–52. https://doi.org/10.1016/j.intermet.2015.12.003.
[91] Bhattacharya K, Kohn RV. Elastic Energy Minimization and the Recoverable Strains of Polycrystalline Shape-Memory Materials. Archive for Rational Mechanics and Analysis 1997;139:99–180. https://doi.org/10.1007/s002050050049.
[92] Ii S, Yamauchi K, Maruhashi Y, Nishida M. Direct evidence of correlation between {2 0 1̄}B19′ and {1 1 4}B2 deformation twins in Ti–Ni shape memory alloy. Scripta Materialia 2003;49:723–7. https://doi.org/10.1016/s1359-6462(03)00356-7.

[93] Surikova NS, Tyumentsev AN, Evtushenko OV. Stress-induced martensitic transformations in [001] crystals of titanium nickelide and its relation to mechanical twinning in the B2-phase. Russian Physics Journal 2009;52:612–21. https://doi.org/10.1007/s11182-009-9271-y.
[94] Shi XB, Hu ZC, Hu XW, Zhang JS, Cui LS. Effect of plastic deformation on stress-induced martensitic transformation of nanocrystalline NiTi alloy. Materials Characterization 2017;128:184–8. https://doi.org/10.1016/j.matchar.2017.04.002.
[95] Šittner P, Heller L, Sedlák P, Chen Y, Tyc O, Molnárová O, et al. B2 ⇒ B19′ ⇒ B2T Martensitic Transformation as a Mechanism of Plastic Deformation of NiTi. Shape Memory and Superelasticity 2019;5:383–96. https://doi.org/10.1007/s40830-019-00250-5.
[96] Polatidis E, Šmíd M, Kuběna I, Hsu W-N., Laplanche G, Van Swygenhoven H. Deformation mechanisms in a superelastic NiTi alloy: An in-situ high resolution digital image correlation study. Materials & Design 2020;191:108622. https://doi.org/10.1016/j.matdes.2020.108622.
[97] Tabanli RM, Simha NK, Berg BT. Mean strain effects on the fatigue properties of superelastic NiTi. Metallurgical and Materials Transactions A 2001;32:1866–9. https://doi.org/10.1007/s11661-001-0164-0.
[98] Frenzel J, George EP, Dlouhy A, Somsen Ch, Wagner MF-X ., Eggeler G. Influence of Ni on martensitic phase transformations in NiTi shape memory alloys. Acta Materialia 2010;58:3444–58. https://doi.org/10.1016/j.actamat.2010.02.019.
[99] Yang Y, Lu H, Yu C, Chen JM. First-principles calculations of mechanical properties of TiC and TiN. Journal of Alloys and Compounds 2009;485:542–7. https://doi.org/10.1016/j.jallcom.2009.06.023.
[100] Siegl J, Nedbal I, Kunz J. Fatigue crack growth history in damage tolerance design of aircraft structures. International Journal of Fatigue 2009;31:1062–7. https://doi.org/10.1016/j.ijfatigue.2008.05.006.
[101] Tyc O. Studium vlivu elektropulzní tepelné úpravy na funkční a strukturní únavu tenkých vláken ze slitiny s tvarovou pamětí NiTi. Diploma Thesis. 2015.
[102] Jiří Kunz, České Vysoké Učení Technické V Praze. Jaderná A Fyzikálně Inženýrská Fakulta. Aplikovaná lomová mechanika. Praha: Česká Technika - Nakladatelství Čvut; 2005.
[103] Robertson SW, Mehta A, Pelton AR, Ritchie RO. Evolution of crack-tip transformation zones in superelastic Nitinol subjected to in situ fatigue: A fracture mechanics and synchrotron X-ray microdiffraction analysis. Acta Materialia 2007;55:6198–207. https://doi.org/10.1016/j.actamat.2007.07.028.
[104] Kimiecik M, Jones JW, Daly S. Quantitative Studies of microstructural phase transformation in Nickel–Titanium. Materials Letters 2013;95:25–9. https://doi.org/10.1016/j.matlet.2012.12.063.
[105] Kimiecik M, Wayne Jones J, Daly S. Grain orientation dependence of phase transformation in the shape memory alloy Nickel–Titanium. Acta Materialia 2015;94:214–23. https://doi.org/10.1016/j.actamat.2015.04.026.
[106] Gall K, Tyber J, Wilkesanders G, Robertson SW, Ritchie RO, Maier HJ. Effect of microstructure on the fatigue of hot-rolled and cold-drawn NiTi shape memory alloys. Materials Science and Engineering: A 2008;486:389–403. https://doi.org/10.1016/j.msea.2007.11.033.
[107] Holtz R. Fatigue thresholds of Ni-Ti alloy near the shape memory transition temperature. International Journal of Fatigue 1999;21:137–45. https://doi.org/10.1016/s0142-1123(99)00065-1.
[108] Saikrishna CN, Ramaiah KV, Paul D, Bhaumik SK. Enhancement in fatigue life of NiTi shape memory alloy thermal actuator wire. Acta Materialia 2016;102:385–96. https://doi.org/10.1016/j.actamat.2015.09.034.
[109] Saikrishna CN, Ramaiah KV, Vidyashankar B, Bhaumik SK. Effect of Intermittent Overload Cycles on Thermomechanical Fatigue Life of NiTi Shape Memory Alloy Wire. Metallurgical and Materials Transactions A 2012;44:5–8. https://doi.org/10.1007/s11661-012-1557-y.
[110] Wagner MF-X, Nayan N, Ramamurty U. Healing of fatigue damage in NiTi shape memory alloys. Journal of Physics D: Applied Physics 2008;41:185408. https://doi.org/10.1088/0022-3727/41/18/185408.
[111] Ahadi A, Sun Q. Stress-induced nanoscale phase transition in superelastic NiTi by in situ X-ray diffraction. Acta Materialia 2015;90:272–81. https://doi.org/10.1016/j.actamat.2015.02.024.

[112] Sun Q, Aslan A, Li M, Chen M. Effects of grain size on phase transition behavior of nanocrystalline shape memory alloys. Science China Technological Sciences 2014;57:671–9. https://doi.org/10.1007/s11431-014-5505-5.
[113] Luo J, He J, Wan X, Dong T, Cui Y, Xiong X. Fracture properties of polycrystalline NiTi shape memory alloy. Materials Science and Engineering: A 2016;653:122–8. https://doi.org/10.1016/j.msea.2015.12.014.
[114] Zurbitu J, Santamarta R, Picornell C, Gan WM, Brokmeier H-G ., Aurrekoetxea J. Impact fatigue behavior of superelastic NiTi shape memory alloy wires. Materials Science and Engineering: A 2010;528:764–9. https://doi.org/10.1016/j.msea.2010.09.094.
[115] Simon T, Kröger A, Somsen C, Dlouhy A, Eggeler G. On the multiplication of dislocations during martensitic transformations in NiTi shape memory alloys. Acta Materialia 2010;58:1850–60. https://doi.org/10.1016/j.actamat.2009.11.028.
[116] Pourbabak S, Verlinden B, Van Humbeeck J, Schryvers D. DSC Cycling Effects on Phase Transformation Temperatures of Micron and Submicron Grain Ni50.8Ti49.2 Microwires. Shape Memory and Superelasticity 2020;6:232–41.
[117] Zhao T, Kang G, Yu C, Kan Q. Experimental investigation of the cyclic degradation of the one-way shape memory effect of NiTi alloys. International Journal of Minerals, Metallurgy and Materials 2019;26:1539–50. https://doi.org/10.1007/s12613-019-1884-8.
[118] Šittner P, Vokoun D, Dayananda GN, Stalmans R. Recovery stress generation in shape memory Ti50Ni45Cu5 thin wires. Materials Science and Engineering: A 2000;286:298–311. https://doi.org/10.1016/s0921-5093(00)00816-9.
[119] Liu Y, Favier D. Stabilisation of martensite due to shear deformation via variant reorientation in polycrystalline NiTi. Acta Materialia 2000;48:3489–99. https://doi.org/10.1016/s1359-6454(00)00129-4.
[120] Coppola R, Klimenkov M, Lindau R, Mangiapia G. Small-angle neutron scattering (SANS) characterization of 13.5 Cr oxide dispersion strengthened ferritic steel for fusion applications. Nuclear Materials and Energy 2020;24:100778. https://doi.org/10.1016/j.nme.2020.100778.
[121] Frenzel J, Zhang Z, Somsen Ch, Neuking K, Eggeler G. Influence of carbon on martensitic phase transformations in NiTi shape memory alloys. Acta Materialia 2007;55:1331–41. https://doi.org/10.1016/j.actamat.2006.10.006.
[122] Karaman I, Kulkarni AV, Luo ZP. Transformation behaviour and unusual twinning in a NiTi shape memory alloy ausformed using equal channel angular extrusion. Philosophical Magazine 2005;85:1729–45. https://doi.org/10.1080/14786430412331331961.
[123] Liu Y, Xie ZL. Twinning and detwinning of 〈0 1 1〉 type II twin in shape memory alloy. Acta Materialia 2003;51:5529–43. https://doi.org/10.1016/s1359-6454(03)00417-8.
[124] Reece PL. Progress in smart materials and structures. New York: Nova Science Publishers; 2007.
[125] Molnárová O, Tyc O, Heller L, Seiner H, Sittner P. 3D Reconstruction of Martensitic Microstructures in Grains of Deformed Nanocrystalline NiTi Wires by TEM. SSRN Electronic Journal 2021. https://doi.org/10.2139/ssrn.3797420.
[126] WAITZ T. The self-accommodated morphology of martensite in nanocrystalline NiTi shape memory alloys. Acta Materialia 2005;53:2273–83. https://doi.org/10.1016/j.actamat.2005.01.033.
[127] Petersmann M, Antretter T, Waitz T. Special cases of martensite compatibility: A near single-variant habit-plane and the martensite of nanocrystalline NiTi. MATEC Web of Conferences 2015;33:03015. https://doi.org/10.1051/matecconf/20153303015.
[128] Waitz T, Antretter T, Fischer FD, Karnthaler HP. Size effects on martensitic phase transformations in nanocrystalline NiTi shape memory alloys. Materials Science and Technology 2008;24:934–40. https://doi.org/10.1179/174328408x302620.
[129] Liu Y, Tan G, Miyazaki S. Deformation-induced martensite stabilisation in [100] single-crystalline Ni–Ti. Materials Science and Engineering: A 2006;438-440:612–6. https://doi.org/10.1016/j.msea.2006.02.130.
[130] Norfleet DM, Sarosi PM, Manchiraju S, Wagner MF-X., Uchic MD, Anderson PM, et al. Transformation-induced plasticity during pseudoelastic deformation in Ni–Ti microcrystals. Acta Materialia 2009;57:3549–61. https://doi.org/10.1016/j.actamat.2009.04.009.

[131] Bowers ML, Chen X, De Graef M, Anderson PM, Mills MJ. Characterization and modeling of defects generated in pseudoelastically deformed NiTi microcrystals. Scripta Materialia 2014;78-79:69–72. https://doi.org/10.1016/j.scriptamat.2014.02.001.
[132] Paranjape HM, Bowers ML, Mills MJ, Anderson PM. Mechanisms for phase transformation induced slip in shape memory alloy micro-crystals. Acta Materialia 2017;132:444–54. https://doi.org/10.1016/j.actamat.2017.04.066.
[133] Casalena L, Bucsek AN, Pagan DC, Hommer GM, Bigelow GS, Obstalecki M, et al. Structure-Property Relationships of a High Strength Superelastic NiTi-1Hf Alloy. Advanced Engineering Materials 2018;20:1800046. https://doi.org/10.1002/adem.201800046.
[134] Zhang JX, Sato M, Ishida A. Deformation mechanism of martensite in Ti-rich Ti–Ni shape memory alloy thin films. Acta Materialia 2006;54:1185–98. https://doi.org/10.1016/j.actamat.2005.10.046.
[135] Chen J, Wu Y, Yin H. In situ multi-field investigation of grain size effects on the rate-dependent thermomechanical responses of polycrystalline superelastic NiTi. Materials Letters 2020;259:126845. https://doi.org/10.1016/j.matlet.2019.126845.
[136] James RD. Taming the temperamental metal transformation. Science 2015;348:968–9. https://doi.org/10.1126/science.aab3273.
[137] Chluba C, Ge W, Lima de Miranda R, Strobel J, Kienle L, Quandt E, et al. Ultralow-fatigue shape memory alloy films. Science 2015;348:1004–7. https://doi.org/10.1126/science.1261164.
[138] Bumke L, Zamponi C, Jetter J, Quandt E. Cu-rich Ti52.8Ni22.2Cu22.5Co2.5 shape memory alloy films with ultra-low fatigue for elastocaloric applications. Journal of Applied Physics 2020;127:225105. https://doi.org/10.1063/5.0006301.
[139] LePage WS, Ahadi A, Lenthe WC, Sun Q-P, Pollock TM, Shaw JA, et al. Grain size effects on NiTi shape memory alloy fatigue crack growth. Journal of Materials Research 2017;33:91–107. https://doi.org/10.1557/jmr.2017.395.
[140] Chen J, Yin H, Sun Q. Effects of grain size on fatigue crack growth behaviors of nanocrystalline superelastic NiTi shape memory alloys. Acta Materialia 2020;195:141–50. https://doi.org/10.1016/j.actamat.2020.05.008.